Extended Search for Axion Dark Matter with ADMX

Nick Du

A dissertation
submitted in partial fulfillment of the
requirements for the degree of

Doctor of Philosophy

University of Washington

2021

Reading Committee:

Leslie J Rosenberg, Chair

Gray Rybka

Sarah Tuttle

Program Authorized to Offer Degree:
Physics

University of Washington

Abstract

Extended Search for Axion Dark Matter with ADMX

Nick Du

Chair of the Supervisory Committee:
Dr. Leslie J Rosenberg
Physics

The axion is a hypothetical elementary particle that came out of a solution to the Strong-CP problem in Quantum Chromodynamics (QCD). The properties of the axion also make it a highly compelling candidate for dark matter. Axion haloscopes are instruments that search for axion dark matter in the local Milky Way halo by searching for the conversion of an axion into photons via the inverse Primakoff effect. The Axion Dark Matter eXperiment (ADMX) is by far the most sensitive axion haloscope, being the first to exclude benchmark models for the QCD axion and continuing to take data at high sensitivity. This thesis reports on a run by ADMX which excluded dark matter axions in the galactic halo over the mass range 2.81–3.31 μeV. This unprecedented sensitivity in this mass range is achieved by deploying an ultra low-noise Josephson parametric amplifier as the first-stage signal amplifier.

TABLE OF CONTENTS

LIST OF FIGURES

ACKNOWLEDGMENTS

I would like to thank my advisor Leslie Rosenberg for his continued mentorship and for reminding me of my personal value. I would also like to thank Gray Rybka for acting as a second mentor and someone to talk to. I would also like to thank all the members of the ADMX collaboration for their friendship and help. Thanks to my friends and family. I would not have made it to where I am without your love and support.

DEDICATION

To my brother Michael, the greatest honor I've ever had is being your older brother.

Chapter 1

INTRODUCTION

One of the biggest mysteries in modern physics is the nature of a form of matter known as "dark matter". There is strong astrophysical evidence that 85% of the matter in the Universe exists in the form of a non-luminous and non-relativistic dark matter. However, the composition of dark matter is unknown; this is one of the biggest mysteries in physics.

One of the most compelling candidates for dark matter is motivated by considering another mystery in physics, namely the "Strong CP problem" in quantum chromodynamics (QCD). In essence, the Strong CP problem is the observation that QCD is found to preserve CP symmetry in strong interactions despite an explicitly CP-violating term in the QCD Lagrangian. One of the most elegant solutions to the problem, first put forward by Helen Quinn and Roberto Peccei, leads to the existence of a new particle, dubbed the "axion". It happens that the axion's properties also make it a compelling candidate for dark matter in the Universe. That the axion solves two important problems in physics is what makes it so compelling.

This thesis describes an experiment based on the "axion haloscope", conceptualized by Pierre Sikivie, an experimental instrument that searches for dark-matter axions in the local Milky Way halo. A haloscope detects axions through their conversion into microwave photons via the inverse Primakoff effect of an axion scattering off a virtual photon thereby becoming a real microwave photon. The conversion power is enhanced by surrounding the conversion region with a high quality factor (Q) microwave cavity. The power is further amplified by an ultra-low noise receiver chain. Examples of axion haloscopes include ABRACADABRA [1], and HAYSTAC [2], but by far the most sensitive haloscope is the Axion Dark Matter eXperiment (ADMX) sited at the University of Washington.

This experiment is the heart of my thesis. During my time as a graduate student, I had the opportunity to play a key role in the ADMX experiment. My contributions include designing the the sensor package for the ADMX experiment, implementing a scheme for blinded-synthetic axion injections, and developing the data analysis for the experiment. I oversaw data taking for what became known as "Run 1B" of ADMX, from January to October 2018, during which time we searched for axion dark matter between the photon frequencies 680 - 780 MHz (axion mass: 2.81-3.31 μeV). The data collected during this run and incorporated into my thesis represent the world's best limits on axion dark matter by an axion haloscope, and achieve sensitivity to the most well motivated benchmark models for axion dark matter in that mass range.

Chapter 2

BASIC THEORY

The search for axion dark matter by ADMX is motivated by two mysteries in physics: the nature of dark matter and the Strong CP problem. Both problems come from different fields of physics, but can very elegantly be explained by the "Peccei-Quinn" mechanism leading to the existence of axion dark matter. In this chapter, I will begin by reviewing the dark matter problem in cosmology. Then I will provide an overview of the axion as a solution to the "Strong CP" problem in QCD and how the properties of the axion make it a compelling dark matter candidate. I will conclude with an overview of several methods of searching for the axion, focusing on the axion haloscope.

2.1 A Brief History of the Universe

Leaving out many details here, I will give a overview of the particle and thermal history of the Universe. The timeline of the evolution of the Universe is shown in figure 2.1. Immediately following the Big Bang (10^{-34} s), the Universe was incredibly hot and dense. At this time, the temperature of the Universe had yet to fall below the Planck scale (10^{19} GeV), so subatomic particles had not yet formed and the four fundamental forces had yet to separate [3]. The physics during this period is as of yet not well understood.

As the Universe began to expand and cool below appropriate symmetry-breaking scales, the four fundamental forces arose. Around this time it could be possible that the Universe also underwent a period of rapid exponential "inflation", thereby increasing its volume by a factor of at least 10^{78} and decreasing the temperature of the Universe by many orders of magnitude [4]. Following inflation, as the Universe continued to expand and cool and quarks began to combine into hadrons.

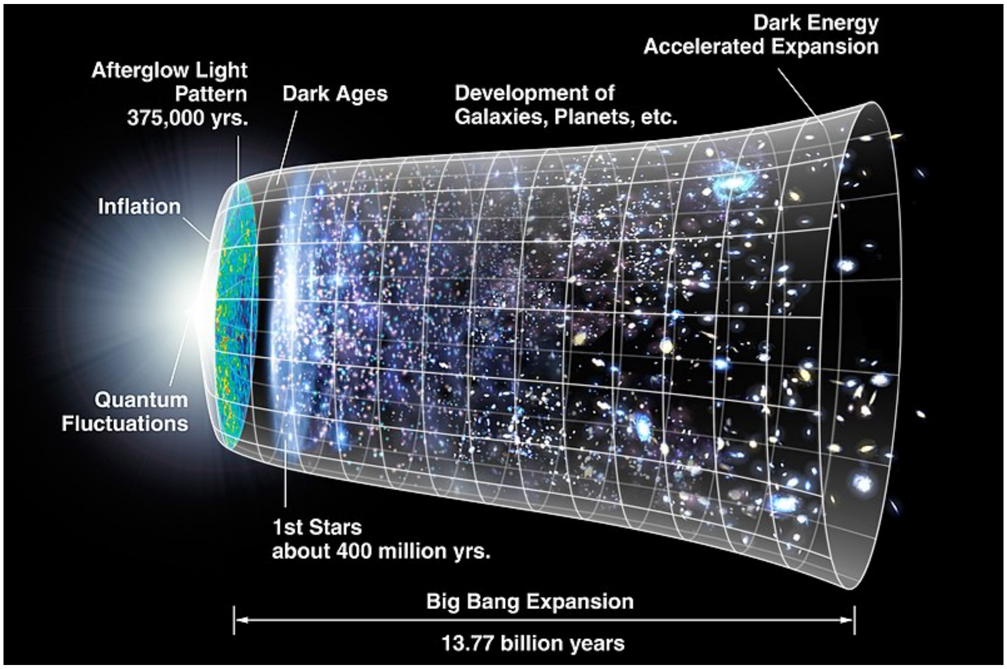

Figure 2.1: A timeline of the evolution of the Universe. PC: WMAP and NASA.

Around 1 second after the Big Bang, neutrinos in the primordial plasma became decoupled from other forms of matter, thereby falling out of thermal equilibrium. After 10 seconds, the Universe began "Big Bang nucleosynthesis", a process by which light nuclei began to form through the fusion of protons and neutrons. This period was responsible for producing most of the Universe's ^{4}He, and also to a lesser extent, deuterium (^{2}H), ^{3}He, and ^{7}Li [5]. During this time, the Universe was a hot plasma of nuclei, electrons, and photons. Dark matter began to gather around small inhomogeneities in the density of the plasma or it could be dark matter seeded the initial inhomogeneities. Because dark matter was not affected by radiation pressure, unlike regular matter, during this period it could collapse much faster, evolving into diffuse filaments, halos, and other structures. These denser regions of dark matter thus in turn, acted as the seed for future structure formation [6].

After 370,000 years, the Universe had cooled to about 4000 K. At this temperature, electrons and atomic nuclei were finally cool enough that they could begin to bind with one another, forming the first electrically neutral hydrogen atoms, a period known as "recombination". With this onset of neutral-atom production, the photons and matter became decoupled and photons then began to stream freely through the Universe. Photons from this time have been observed as the Cosmic Microwave Background (CMB) [3].

By the end of recombination, the majority of baryonic matter in the Universe was in the form of electrically-neutral atoms. During this time, the Universe entered what was known as the "Dark Ages" due to the lack of light-producing structures. Baryonic matter began to collect around the previously-mentioned dark matter structures, eventually becoming the stars and galaxies observed today [3].

2.2 Dark Matter

Since the early 20th century, astrophysical observations suggested the existence of an unobserved form of matter. This unusual matter interacts gravitationally, but has little or no interactions with normal matter and radiation. This unknown form of matter, dubbed "dark matter", accounts for about 85% of all the matter in the Universe. While the nature of dark matter, presumably a particle remnant leftover from the Big Bang, has been one of the greatest mysteries in physics, there is strong evidence for the properties for dark matter are as follows [7]: Dark matter is

1. Feebly interacting or non-interacting with normal matter and radiation,

2. Non-baryonic,

3. Moving at non-relativistic speeds at the time of structure formation.

In this section, I will outline selected evidence in support of the existence of dark matter with these properties.

2.2.1 Galactic Rotation Curves

The rotation curve of a galaxy graphically shows the orbital speed of visible matter in the galaxy versus its distance from the center of the galaxy. In 1932, Jan Oort reported the first observation that the measured speed of stars in the Milky Way galaxy was greater than that expected from the gravitational potential from the visible matter [8]. Much later, this was codified by Vera Rubin and Kent Ford who studied the rotation curves of 21 spiral galaxies and noted that in each case the rotation curves implied a galaxy mass density that grew linearly with radius and speed exceeding the Keplerian speed owing to visible matter [9]. An example of one such rotation curve for NGC 6503 is shown in figure 2.2.

Assuming a disk-like distribution of matter, Newtonian mechanics dictates the orbital speed as a function of distance from the center of the galaxy would be

- $v \ \alpha \ r$ (Inside the disk)
- $v \ \alpha \ 1/\sqrt{r}$ (Outside the disk),

where v is the orbital speed of matter, and r is distance of the matter from the center of the galaxy. For the rotation curve shown in figure 2.2, outside the visible disk the velocity did not go as $1/\sqrt{r}$, but instead approached a constant at large distances. This discrepancy between the observed and predicted rotation curves can be resolved if there exists an additional extended halo of non-luminous matter, dark matter, surrounding the visible disk of matter in the galaxy. If such dark matter exists, there are important further questions as to its detailed distribution in the galaxy.

2.2.2 Gravitational Lensing

The phenomenon in which light from distant sources passing through a strong gravitational field is bent is known as gravitational lensing. The amount of bending is related to, among other things, the strength of the intervening gravitational field between the observer and source. By measuring how much the light from distant astrophysical sources is bent on

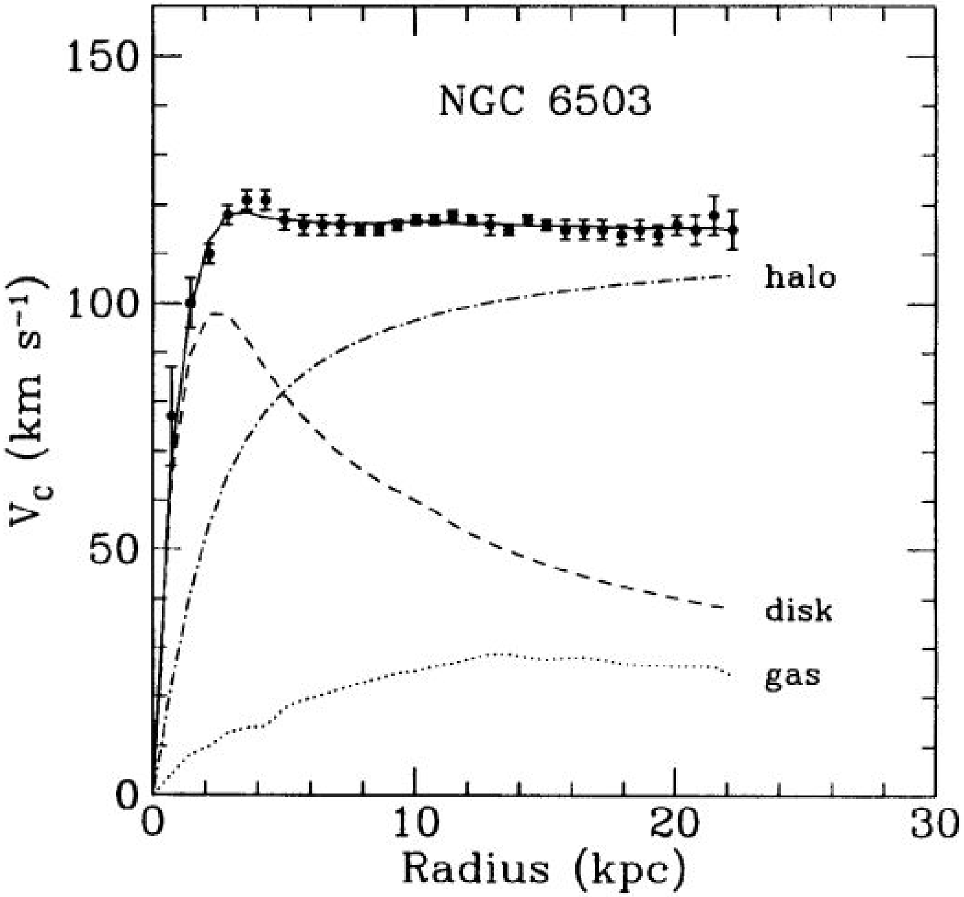

Figure 2.2: The galactic rotation curve of NGC 6503. The vertical axis is the speed of rotation and the horizontal axis is the distance from the center of the galaxy. The data points are speed of rotation for neutral hydrogen gas disks surrounding the galaxy, determined from the 21-cm line of neutral hydrogen's spin transition. The dashed lines are the expected contribution to the rotation curve by the visible disk, gas and unseen halo. The edge of the visible disk is at about 1 kpc, marked by when the contribution to the rotation curve of the visible disk transitions to going as $v \ \alpha \ 1/\sqrt{r}$. In comparison, it is clear that the rotation curves cannot be explained by the visible gas and disk of matter alone. Instead, a unseen halo of matter can explain that the rotation curves are constant even at distances far from the center of the galaxy. Photo Credit: [10].

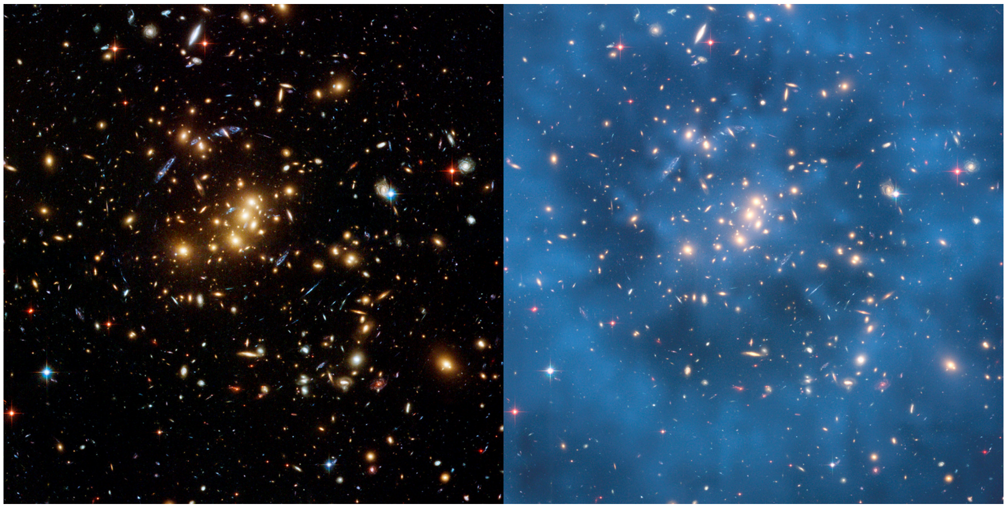

Figure 2.3: Two pictures of galaxy cluster CL 0024+17 taken by Hubble. Left: The visible light from the galaxy cluster. Note the presence of blue arcs within the image, which are light from distant galaxies undergoing gravitational lensing as they travel through the cluster. Right: Blue shading has been overlaid on top of the image to show the distribution of matter required to produce the lensing observed. More darkly shaded regions represent denser regions of dark matter. Photo Credit: NASA, ESA, M.J. Jee and H. Ford (Johns Hopkins University).

passing through the galaxies or clusters of galaxies, the total mass of the galaxy "lens" can be inferred as well as some details of the galactic mass distribution. Measurements such of these performed on galaxy clusters suggested that the total mass within the galaxy cluster is much larger than can be accounted for by visible matter in the galaxy [11]. This suggests the existence of a dominant component of non-visible matter in galaxies. Another inference from lensing is the extra mass is smoothly distributed.

2.2.3 Bullet Cluster

The evidence reviewed so far has suggested the existence of an additional non-luminous form of matter. The Bullet Cluster, which consists of two colliding galaxy clusters, provides evidence that "dark matter" must be at most feebly interacting. As the galaxy clusters collided, the baryonic matter from each cluster interacted with and slowed one another, emitting X-rays as the matter slowed. The emitted X-rays are used to infer the distribution of baryonic matter, while the total distribution of matter is inferred through gravitational lensing, as discussed in section 2.2.2. Both the distribution of baryonic matter and total matter are shown in figure 2.4. In the picture, it is clear the distribution of baryonic matter does not align with the total distribution of matter. This suggests that the dark matter didn't interact during the collision of the galaxies, instead passing through each other, and leading to the observed difference in position of the baryonic and total matter distributions [12]. From the evidence provided by the Bullet Cluster, we can infer that dark matter is at most, feebling interacting with regular matter.

2.2.4 Cosmic Microwave Background

Recall, the Cosmic Microwave Background (CMB) refers to the remnant electromagnetic radiation produced in the early Universe. When the Universe was about 370,000 years old, the Universe had cooled to about 4000 K, a temperature where hydrogen atoms could form from protons and electrons. The formation of electrically-neutral atoms decoupled the electromagnetic radiation from matter, thus allowing the radiation to provide a picture of the Universe at that time. As the Universe continued to expand, the temperature of the radiation eventually decreased to its present temperature of 2.725 K and was redshifted into microwave frequencies. The CMB was more or less first accidentally detected in 1965 by Arno Penzias and Robert Wilson, and was found to be remarkably isotropic [13]. Precision measurements of the CMB from probes such as WMAP and Planck uncovered small anisotropies on the scale of one part in 100,000, shown in figure 2.5 [14, 15].

The anisotropies that arose in the CMB were primarily due to acoustic density waves in the plasma of the early Universe. In the early Universe, over-dense regions in the plasma pulled in additional matter. As the density of photons increased, radiation pressure from photons generated an outward pressure. The opposition between the gravitational force and radiation pressure from photons generated acoustic density oscillations, "baryon acoustic oscillations", which were imprinted as anisotropies in the CMB.

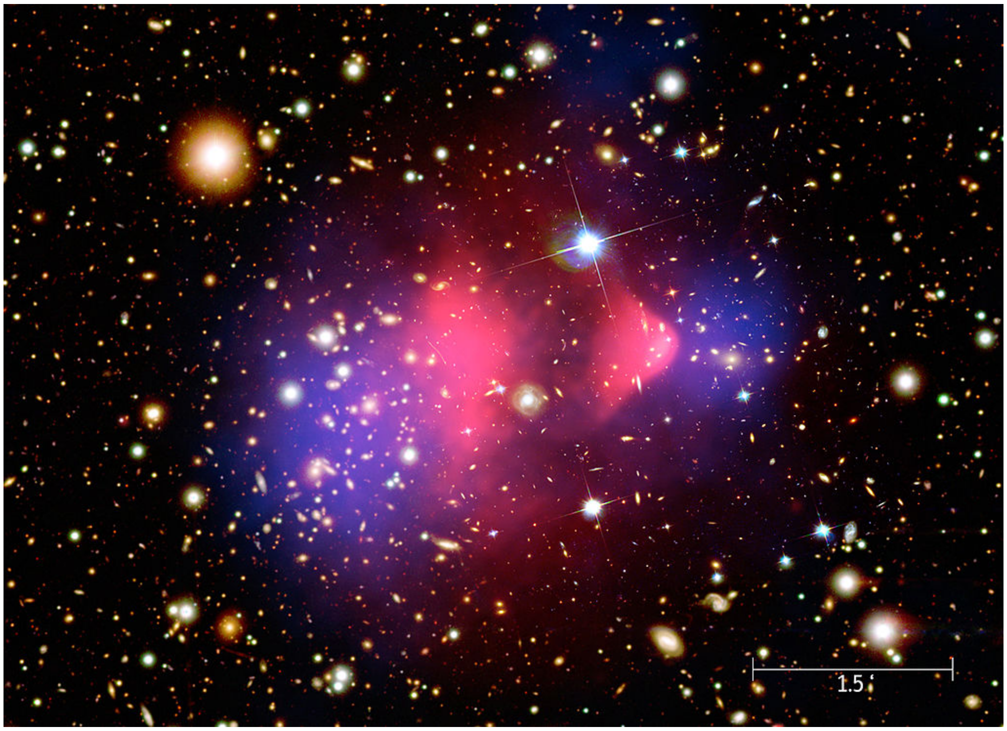

Figure 2.4: A picture of the Bullet Cluster from the Chandra Observatory, overlaid with the baryonic matter distribution inferred from X-ray emissions (Pink) and the matter distribution determined from gravitational lensing (Blue). The difference in position between the two can be explained by the existence of an additional non-luminous, non-baryonic form of matter. Photo Credit: X-RAY: NASA/CXC/CFA/M.Markevitch et al.; LENSING MAP: NASA/STSCI; ESO WFI; Magellan/U.Arizone/D.Clowe et al.; OPTICAL: NASA/STSCI; Magellan/U.Arizona/D.Clowe et al.

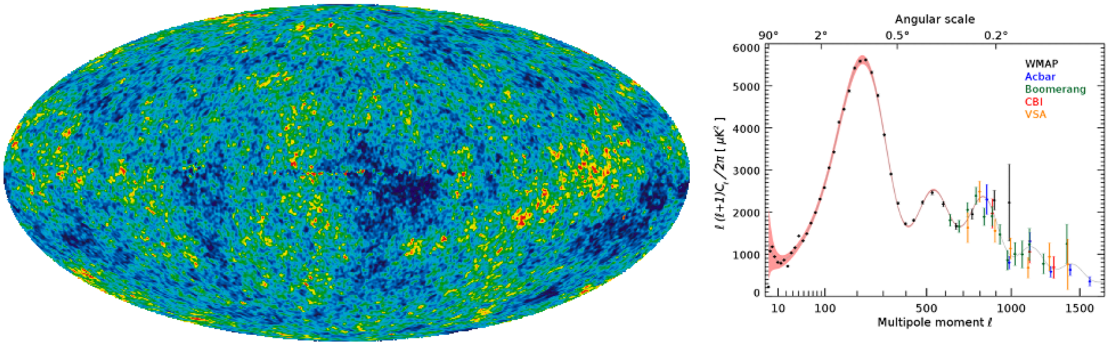

Figure 2.5: Left: An image of the CMB taken by WMAP. Spots represent anisotropies in the temperature of the CMB on the order of 1 part in 100,000. Right: An image of the power spectrum of the CMB taken from Planck data with a fit to the standard dark matter model in green. The angular scale and relative size of the peaks provide information on a number of cosmological parameters. For example, the first peak being at 1 degree indicates the Universe is flat. The ratio of the first peak to the second peak indicates that baryonic matter accounts for only 5% of the total mass-energy in the Universe. Photo Credit: WMAP.

The anisotropies observed in the CMB provide among the best constraints on the cosmic abundance of matter in the Universe. Decomposing the CMB into its power on angular scale provides information on the intensity of these anisotropies. The location and relative sizes of the peaks contain, among other things, information about the curvature of space, the baryon density and the dark matter density. A study of the power spectrum of the CMB suggests the total baryon and matter densities in the Universe to be

$$\Omega_{baryon} h^2 = 0.0226 \pm 0.0006 \tag{2.1}$$

$$\Omega_{matter} h^2 = 0.135 \pm 0.009 \tag{2.2}$$

where Ω_{baryon} and Ω_{matter} are the baryon and matter density, respectively, and $h = H\ MPc/100\ km/s$ is the Hubble expansion parameter in units of 100 km s^{-1} Mpc^{-1} [15]. Therefore, baryonic matter can only account for a small portion of the total matter in the Universe.

2.2.5 Hot vs. Cold Dark Matter

The designation of dark matter candidates as being “hot” or “cold” refers to whether the candidate was moving at relativistic or non-relativistic speeds, respectively, at the time of structure formation. Depending on whether dark matter is hot or cold, the path to structure formation in our Universe changes dramatically. In the case of hot dark matter, the fast-moving dark matter smoothed out the primordial density fluctuations in the early Universe. This led to “top-down” structure formation where large structures eventually fragmented into galaxies. In the case of cold dark matter, the dark matter moved slowly enough for small density fluctuations to grow, acting as seeds for structure formation. This led to “bottom-up” structure formation in which galaxies formed first, later merging into galaxy clusters. For “top-down” and “bottom-up” structure formation simulations, the Universe as we know it is consistent with the latter, suggesting that dark matter is cold, with at most a small hot component [3].

2.2.6 Lambda-CDM Model

The “Lambda-CDM model” (ΛCDM) is a model for how the Universe as we know it evolved from the Big Bang. It is the simplest model that can account for gross details of the structure of the CMB, the structure formation and distribution of galaxies, and the accelerating expansion of the Universe. It is based upon the assumption that the Universe is isotropic and homogeneous and that Einstein’s theory of General Relativity is correct on cosmological scales.

The model breaks the Universe down into three major components, dark energy, dark matter, and atoms, as shown in figure 2.6. Λ is a cosmological constant associated with dark energy, a self repulsive force meant to account for the accelerating expansion of the Universe. The model also includes a self-attracting cold dark matter (CDM) term. The presence of CDM is critical for structure formation of galaxies on the observed timescales. Lastly, the model includes a third component that is ordinary matter in the Universe. Measurements

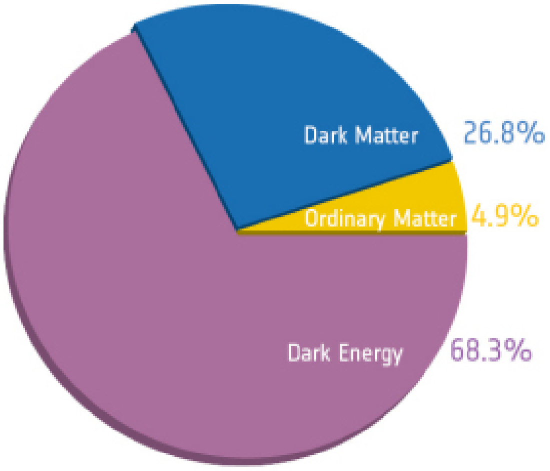

Figure 2.6: A pie chart of the total mass energy distribution in the Universe. Dark matter takes up a notable 26.8% of the total mass energy in the Universe. Photo: Planck.

of the CMB made by the Wilkinson Microwave Anisotropy Probe (WMAP) [14] and Planck telescope [15], supernova redshifts [16], and baryon acoustic oscillations [17] were used to set constraints on the parameters in the Λ-CDM model. These constraints suggest that dark matter makes up 26.8% of the total mass-energy in the Universe and ordinary matter makes up 4.9%. The remaining 68.3% is composed of dark energy, an interesting components but a topic that will not be covered in this thesis.

2.3 The Strong CP Problem and Axions

Quantum Chromodynamics (QCD) is a theory which describes interactions between "colored" objects through the strong force. In its simplest form, the QCD Lagrangian can be written as

$$\mathcal{L}_{QCD} = -\frac{1}{4}G_{a}^{\mu\nu}\ G_{a\mu\nu} + \sum_{j} \bar{\psi}_j (i\gamma^{\mu} D_{\mu} - m_j)\psi_j \tag{2.3}$$

where j labels the quark flavors, ψ_j are the quark fields, γ_μ are the gamma matrices, D_μ is the covariant derivative, m_j are the quark masses, and $G_{\mu\nu}$ is the gluon field-strength tensor.

The non-Abelian nature of the gluon field results in degenerate topologically distinct vacuum states [18]. Being topologically distinct means that each vacuum state is in a distinct class labeled by an integer n, where n is a topological winding number. The physical vacuum state is superposition of these states,

$$|\Theta >= \sum_n e^{-in\theta}|n > \tag{2.4}$$

where θ is an arbitrary parameter that must be measured. This physical state is referred to as the "θ-vacuum". This physical vacuum constructed in this way is gauge invariant.

The effect of the "θ-vacuum" is described by an additional effective term to the QCD Lagrangian

$$\mathcal{L}_\theta = \frac{\bar{\theta}}{32\pi^2} G^a_{\mu\nu} G^{\mu\nu a} \tag{2.5}$$

where $\bar{\theta} = \theta + argdet(M)$ and M is the quark mass matrix. Rewriting this term using the "E" and "B" ("Electric" and "Magnetic") components of the gluon field, the term can be written as

$$\mathcal{L}_\theta = \frac{\bar{\theta}}{16\pi^2} E^a \cdot B^a. \tag{2.6}$$

As in electromagnetism, E^a is a vector and B^a is an axial vector, so $E^a \cdot B^a$ is not preserved under CP symmetry. Thus the additional term, $\mathcal{L}_\theta$ is explicitly CP violating, with the amount of CP violation proportional to $\bar{\theta}$.

Naively one would expect $\bar{\theta}$ to be of order 1, as there is no reason for θ and $arg\ det(M)$ to precisely cancel each other. However, precision experiments, an example of which is discussed below, suggest that $\bar{\theta}$ is immeasurably small. One consequence of CP violation in QCD would be the existence of a neutron electric dipole moment. Figure 2.7 shows a toy model of the neutron acted on by CP (that is, T), demonstrating how the existence of a neutron electric

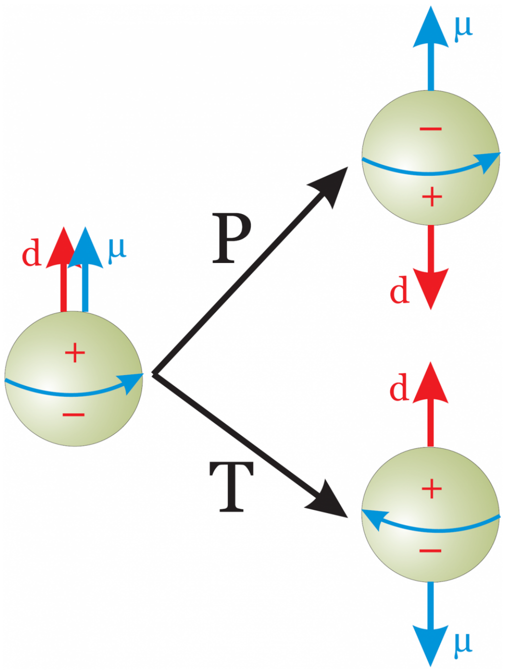

Figure 2.7: A model of the neutron with its associated charge distribution and spin, giving it a magnetic and electric dipole moment pointing in the same direction. Applying time-reversal preserves the charge distribution but reverses the spin, causing the electric and magnetic dipole moments to change directions, violating time-reversal symmetry. By the CPT theorem, a neutron electric dipole moment would therefore violate CP symmetry. Photo Credit: Public domain work from Andreas Knecht.

dipole moment would violate CP (T) symmetry. Attempts to measure the neutron electric dipole moment have instead placed very strong limits on the existence of a neutron electric dipole moment. The current best limit set on the neutron is $d_n = (0.0 \pm 1.1) \times 10^{-26} e\ cm$, which constrains $|\bar{\theta}| < 10^{-10}$ [19]. That two unrelated quantities, θ and $arg\ det(M)$, that is, why a quantity related to the strong interaction and a quantity related to the weak interaction, cancel each other out so precisely, is a fine-tuning problem that has come to be known as the "Strong CP" problem. It is indeed a profound problem and one of the few blemishes on our understanding of the Standard Model.

2.3.1 The Peccei-Quinn Mechanism

While several ideas have been suggested to address the Strong CP problem, perhaps the most popular, and to me the simplest and most sensible, is the solution proposed by Helen Quinn and Roberto Peccei [20]. Their solution was to add a new global $U(1)$ chiral symmetry, known as the Peccei-Quinn symmetry $U(1)_{PQ}$. The new symmetry introduces a new complex pseudoscalar field ϕ. $\bar{\theta}$ is thereby promoted to a dynamical variable as $arg(\phi)$. The QCD potential then takes the classic "wine bottle" form of

$$V(\phi) = \mid \phi^2 \mid - \frac{f_{PQ}^2}{2} \tag{2.7}$$

where f_{PQ} is the symmetry-breaking scale, the energy scale above which CP was violated. This potential is shown in figure 2.8.

In the early formation of the Universe, when temperatures were above the symmetry breaking scale, f_{PQ}, the vacuum expectation value of ϕ was 0 and all values of θ were equally probable. Since θ was non-zero, CP was violated and the neutron had a non-zero electric dipole moment. As the Universe cooled below the symmetry-breaking scale, ϕ developed a non-zero expectation value and $\bar{\theta}$ was constrained to the minimum of the potential. This process is similar to the Higgs mechanism. Peccei and Quinn showed that at the new absolute minimum of the potential, $\bar{\theta}$ would naturally relax to 0, effectively removing the CP-breaking term from the QCD Lagrangian, thereby enforcing CP conservation in strong interactions.

Weinberg and Wilczek later noted that the introduction of the spontaneously-broken U(1) symmetry implied the existence of a pseudo-Nambu Goldstone boson, a pseudoscalar, which was dubbed the "axion" [21, 22]. Because the axial symmetry of the potential was broken through an anomaly (not described here), the axion has a non-zero mass.

2.3.2 Axion Mass and Coupling

The mass of the axion is related to the Peccei-Quinn symmetry-breaking scale, f_{PQ}, via

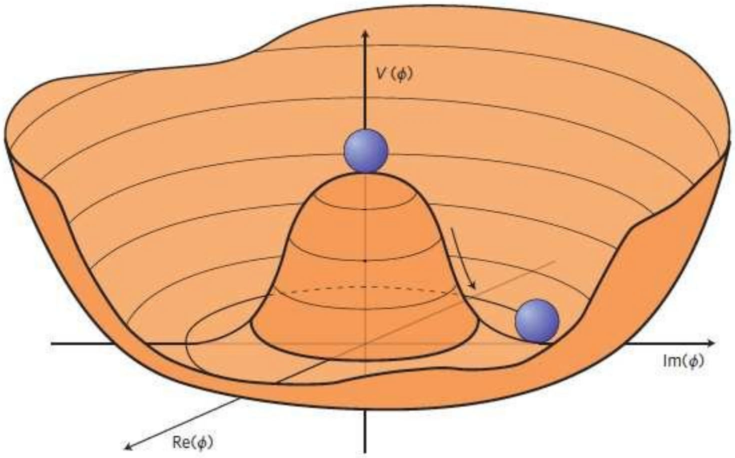

Figure 2.8: The traditional wine-bottle potential of the field ϕ introduced by Peccei and Quinn. Photo Credit: CERN.

$$m_a = 5.691 meV \times \frac{10^9 GeV}{f_{PQ}}. \tag{2.8}$$

Initially, the symmetry-breaking scale was assumed to be associated with the weak scale, $f_{PQ} \sim \nu_{weak}$, corresponding to an axion mass between 10-100 keV. However, such heavy axions, having pion-like couplings, were quickly ruled out by accelerator and other experiments. Simplifying somewhat, by modifying the theory to have a much larger symmetry-breaking scale, a more weakly coupled axion, dubbed the "invisible" axion. This is the particle that this body of work targets.

In axion phenomenology, there are two benchmark models for the axion that are widely accepted as plausible QCD axion models. The Kim-Shifman-Vainshtein-Zakharov (KSVZ) axion couples only to quarks [23, 24], while the Dine-Fischler-Srednicki-Zhitnitsky (DFSZ) axion couples to both quarks and leptons [25, 26]. DFSZ axions are especially compelling because they can be easily implemented into grand unified theories such as SU(5) and grand unified theories embedding SU(5) [25]. It is grand unification that provides the otherwise mysterious cancellation of terms coming from weak and strong interactions which is the heart of the Strong CP problem.

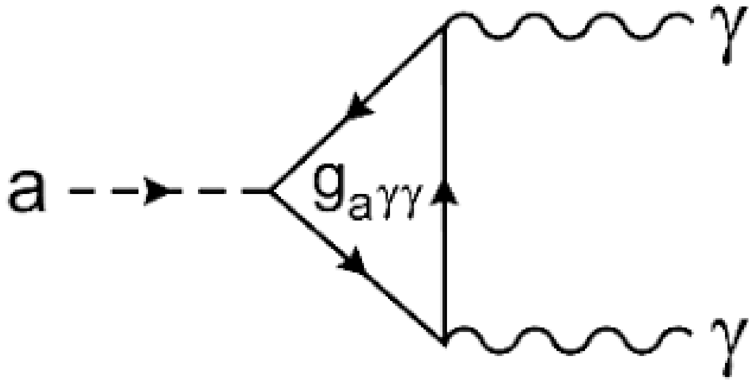

Figure 2.9: A Feynman diagram depicting the process of coupling of an axion to two photons. Photo Credit: NASA/IPAC Extragalactic Database.

Of particular interest for this thesis is the coupling of the axion to photons, specifically the decay of axions into two photons. This coupling is shown in figure 2.9. The axion to two photon coupling is given by

$$g_{a\gamma\gamma} = \frac{\alpha}{2\pi f_{PQ}}(\frac{E}{N} - 1.92) = (0.203\frac{E}{N} - 0.39)\frac{m_A}{GeV^2} = \alpha\frac{g_\gamma}{\pi f_{PQ}}, \tag{2.9}$$

where α is the fine structure constant, g_γ is a model-dependent coupling, f_{PQ} is the symmetry breaking scale, and E and N are the electromagnetic and color anomalies of the axial symmetry. Of the two benchmark models, the DFSZ axion is more weakly coupled, with a model-dependent coupling of 0.36, while the coupling of the KSVZ axion is -0.97.

2.4 Axion Dark Matter

The feebly-interacting nature of the invisible axion with regular matter is one property of the axion that makes it a well-motivated dark-matter candidate. One mechanism for the production of axions in the early Universe is known as vacuum re-alignment (VR) production. In the early Universe, when the temperature of the Universe exceeded the Peccei-Quinn symmetry-breaking scale, Peccei-Quinn symmetry was unbroken and all values of θ were equally probable. When the Universe cooled to below the symmetry breaking scale, Peccei-

Quinn symmetry, $U(1)_{PQ}$ was broken and $\bar{\theta}$ rolled down the "wine-bottle" potential toward the new minimum at $\bar{\theta} = 0$. The equation of motion for $\bar{\theta}$ is similar to that of a damped oscillator in an expanding Universe

$$\ddot{\bar{\theta}} + 3H(t)\dot{\bar{\theta}} + m_a^2 sin(\bar{\theta}) = 0 \tag{2.10}$$

where $H(t)$ is the Hubble constant and m_a is the axion mass. The oscillations about the minimum corresponded to the formation of a pressure-less zero-momentum axion condensate that was out of thermal equilibrium with surrounding hot baryonic matter. The axions could then fall into gravitational potentials from clusters of baryonic matter, implying that axions seed the initial structure and eventually become the dark matter found in galaxies.

The fractional cosmic mass density of the axions formed through the vacuum re-alignment (VR) mechanism is

$$\Omega_A^{VR} h^2 = 0.12(\frac{6\mu eV}{m_A})^{1.165} F\bar{\theta}_i^{\,2}, \tag{2.11}$$

where h is the Hubble expansion parameter, $\bar{\theta}_i$ is the initial misalignment angle relative to the CP-conserving value between $-\pi$ and π, and F is a factor accounting for anharmonicities in the axion potential [27, 28, 29]. Recall that the observed CDM density from CMB observations is $\Omega_{CDM} h^2 = 0.12$. If Peccei-Quinn symmetry was broken pre-inflation, $\bar{\theta}_i$ would take on the same value throughout the whole universe. If $F\bar{\theta}_i$ was $O(1)$, an axion mass of on order 1 μeV would account for 100% of the dark matter in the Universe.

If Peccei-Quinn symmetry was broken post inflation $\bar{\theta}_i$ would take on different values in different causal volumes of the Universe. Taking a root-mean-square average of such volumes gives $\bar{\theta} = \pi/\sqrt{3}$. The equation for the fractional cosmic mass density of axions simplifies to

$$\Omega_A^{VR} h^2 = 0.12(\frac{30\mu eV}{m_A})^{1.165} \text{ [27, 28, 29]}. \tag{2.12}$$

A range of plausible axion masses in the post-inflationary case thus becomes 25 $\mu eV < m_A <$ 4.4 meV.

In either the pre- or post-inflationary case, axions lighter than 1 μeV are produced too abundantly, resulting in overclosure of the Univese. Anthropic arguments can be applied in the pre-inflationary case to argue for axion masses lower that 1 μeV, however I, personally, find anthropic arguments to be weak.

If axions were sufficiently heavy, they could also be produced thermally from quarks and gluons. The dominant process in this case was $\pi + \pi = \pi + A$ [30]. This is an equilibrium process and axions produced thermally would make up a component of hot dark matter in the Universe. For axions masses $m_a < 1\ meV$, the cross section of the axion was too small to produce a significant amount of axions [31, 32, 33]. However, as discussed later, axions with $m_a > 1\ meV$ have been largely ruled out through astrophysical constraints. Thus, axion dark matter produced thermally would likely be subdominant. In addition, a component of cold dark matter axions could be produced from the decay of axion strings [28, 34, 35, 36, 37, 38, 29]. However, the contribution from this mechanism has significant uncertainties and is not considered here.

2.5 Searches for the Axion

Figure 2.10 is a plot of the current "landscape" of searches for axions. In this section I will give an overview of selected constraints on the axion mass, focusing on axion haloscopes, the topic of this thesis.

2.5.1 Astrophysical Constraints on the Axion

In some ways similar to neutrino emission in stars and supernovae, axions are a channel for energy transport out of astrophysical objects. If axions couple strongly enough to regular matter (but not too strongly), they would be produced in sufficient amounts and escape to affect the lifetime and energy loss rates of stars and supernovae. However, if axions are too strongly coupled, axions would be trapped and not escape. These two competing processes, along with data on stellar lifetimes, can be used to place constraints on the axion mass and coupling.

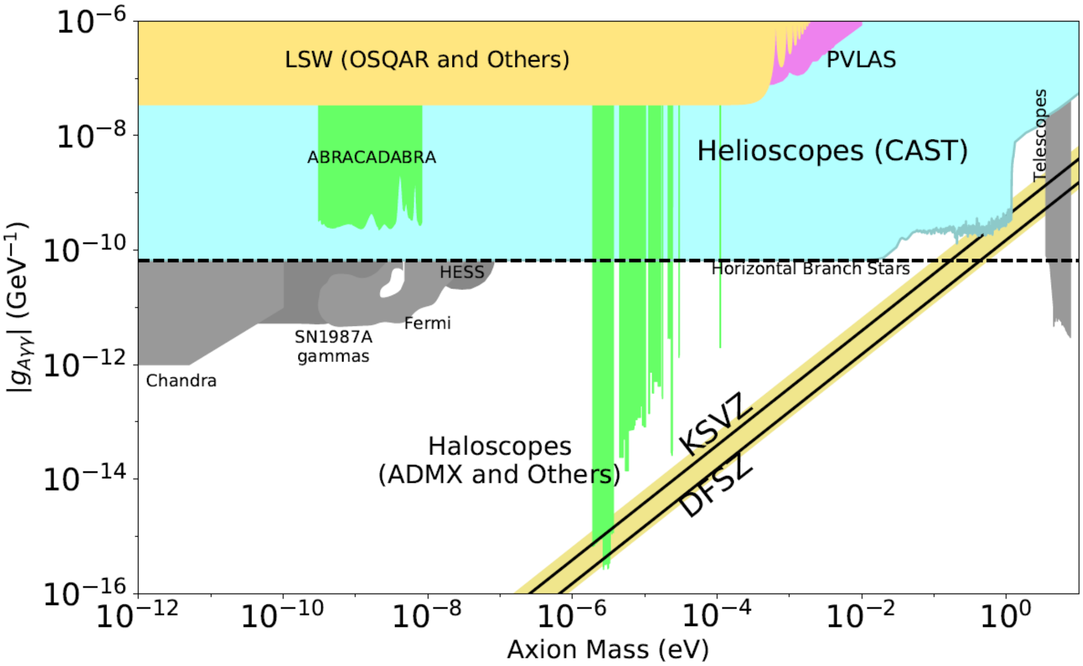

Figure 2.10: The "exclusion plot" for the axion. The vertical axis is the axion-to-photon coupling and the horizontal axis is the axion mass. The diagonal black lines are couplings predicted for the benchmark DFSZ and KSVZ axions. The highlighted region between DFSZ and KSVZ reflects theorectical uncertainties in the coupling. The various shaded regions are limits on the axion-to-photon coupling over a given mass made by different experiments. Note that only haloscopes, shown in green, have been sensitive enough to exclude KSVZ and DFSZ axions in the region from 1-100 μeV. PC: Particle Data Group [39].

I will begin the discussion with our Sun. For the KSVZ axion, the primary means of axion production in the Sun is the Primakoff process $\gamma + Z- > a + Z$. The additional energy loss from axions would cause the Sun to contract to raise its temperature, thereby increasing the nuclear energy production rate in the sun. This would be accompanied by an increase in neutrino fluxes from the Sun. Measurements of neutrino flux from SNO with the standard solar model limit the axion to photon coupling to $g_{a\gamma\gamma} < 4.1 \times 10^{-10}\ GeV^{-1}$ [40].

A much stronger limit on the axion-to-photon coupling comes from observations of globular cluster stars. Globular clusters are gravitationally-bound spherical groupings of stars. The stars within a globular cluster are almost all the same age, and the primary difference between stars in a globular cluster is their initial mass. Therefore, globular cluster stars serves as a powerful tool for studying stellar evolution as the ratio of the number of stars observed in any given phase of their life cycle is directly proportional to the time spent in that phase. The effect of axion emission in stellar evolution would to shorten the helium-burning phase of stars. The observed populations of Horizontal Branch (HB) stars, which burn helium, to Red Giant Branch (RGB) stars, which burn hydrogen, has ruled out $g_{a\gamma\gamma} < 6.6 \times 10^{-11}\ GeV^{-1}$ over a wide mass range [41].

Core-collapse Supernova (SN) 1987A provides additional constraints on the axion. Core collapse occurs when the rate of nuclear fusion in a massive star is no longer sufficient to support against gravity, resulting in the star collapsing in on its core. In SN1987A, the primary means of axion cooling would be through nucleon-nucleon axion brehmsstrahlung. For axions of mass $1\ meV < m_a <\ 2eV$, axion emission would have drastically accelerated the cooling of the supernova core and reduced the duration of the neutrino burst from SN 1987A observed by terrestrial detectors, Kamiokande-II and Irvine-Michigan-Brookhaven detectors [42, 43].

Axion emission through nucleon-nucleon axion bremsstrahlung could also act as an additional source of cooling for neutron stars. The additional cooling from axion emission could account for the fast cooling rate observed in the neutron star (NS) the the supernova remnant Cassiopeia A. Studies including axion emission in the cooling of the Cas A NS were able to put limits on the axion coupling to photons of $g_{app}^2 < (1-6) \times 10^{-17}\ GeV$ [44, 45]. Similar techniques were applied to a young neutron star in the HESS J1731-347 supernova remnant. The high temperature of that neutron star suggested that all neutrino emission processes except neutron-neutron bremsstrahlung would be suppressed. By considering axion emission via neutron-neutron bremsstrahlung, Ref. [46] was able to set a limit on the axion to neutron coupling of $g_{ann}^2 < 7.7 \times 10^{-20}$. This is currently systematically-limited by the cooling models, but could well improve as our understanding improves.

The existence of an extremely light axion can also play a role in the dynamics of rotating astrophysical black holes. When the Compton wavelength of the axion field is comparable to the size of the black hole, the axion can form bound states around the black hole. Through the "superradiance process", in which the rotation of the black hole is used to amplify incoming gravitational waves, the occupation number of these bound states will fill exponentially. When superradiance conditions are fulfilled, a black hole will lose its spin quickly on astrophysical timescales. Measurements made of stellar black holes that satisfy such conditions rule out axions between $6 \times 10^{-13}\ eV < m_a < 2 \times 10^{-11}\ eV$. In addition, the transition between and annihilation of axion "bound states" in the black hole would produce long-lasting gravitational wave signals perhaps detectable by Advanced LIGO (ALIGO). In the future, ALIGO could therefore be used to probe for axions with mass $m_a < 10^{-10}\ eV$ [47]. Although powerful, astrophysical constraints do not probe for QCD dark-matter axions.

2.5.2 Laboratory Searches for the Axion

Laboratory-based searches for the axion provide a means to probe for much more weakly coupled axions than available from astrophysical observations. Currently the most promising laboratory searches for axions rely on the coupling of an axion to two photons via the inverse Primakoff effect.

One class of experiment is "light shining through walls" (LSW). A diagram of one such experiment is shown in figure 2.11 (Top). LSW experiments are realized by sending photons, in the form of laser light, though a dipole magnetic field. Photons in the magnetic field can convert into axions through the axion-to-photon coupling. Blocking the path of the laser, a wall is inserted followed by another dipole magnetic field. While the wall blocks the photons, axions would easily travel through and could reconvert into photons in the magnetic field. The current best limit from LSW experiments was achieved by the OSQAR experiment, setting a limit of $g_{A\gamma\gamma} < 3.5 \times 10^{-8}\ GeV^{-1}$ for $m_A < 0.3\ meV$ [48]. LSW experiments owe their sensitivity to having in the optical path a Fabry-Perot cavity on either side of the wall, thereby increasing the axion-conversion probability by a factor of the cavity finesses.

Axion helioscopes, such as the one shown in figure 2.11 (Bottom) search for the emission of solar axions from the Sun. As discussed earlier, axions could be emitted from the Sun via the Primakoff effect. Using a large static dipole magnetic field, these solar axions can be converted into photons. So far the best limits set by an axion helioscope were those of the CAST experiment with $g_{A\gamma\gamma} < 6.6 \times 10^{-11}\ GeV^{-1}$ for $m_A < 0.02\ eV$ [49]. However, helioscopes are less sensitive for lighter QCD axions, which would be a dark matter candidate.

2.6 Axion Haloscopes

The experiments that have set the best limits by far for QCD dark-matter axion couplings are axion haloscopes. As the Earth travels about Sun, it is bathed in dark matter in the Milky Way halo. In the vicinity of the terrestrial laboratory, this means we expect about 10^{13} axions per cc, a huge number density. Axion haloscopes aim to detect axion dark matter in our local halo via the coupling of an axion to two photons.

The axion haloscope was first conceptualized by Pierre Sikivie in 1983 [51]. The apparatus, shown in figure 2.12, consists of a high-Q microwave resonant cavity placed inside a strong static magnetic field. Due to the large de Broglie wavelength of the cold dark matter axions, around 10 m, relative to the size of the experiment, the axion can be treated as a coherent field driving the cavity. Within the cavity, the axion field couples to the magnetic field, producing photons with frequency $f = E/h$, where E is the total energy from the axion (the rest mass plus a small kinetic energy term). If the resonant frequency of the microwave cavity is tuned to the near the frequency of the axion mass, the power of photon production

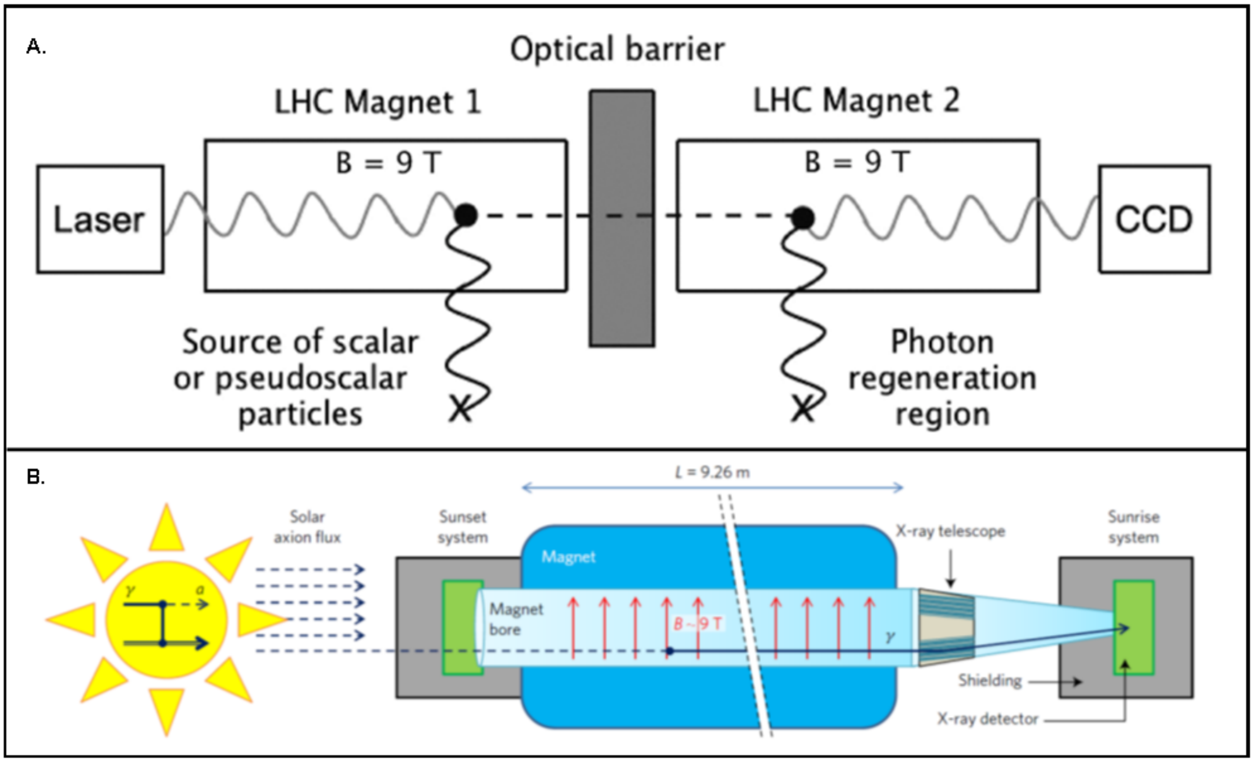

Figure 2.11: Top: A diagram of a"light shining through wall" experiment. Laser light is sent through a static dipole magnetic field and blocked by an optical barrier. On the other side is another static dipole magnetic field. Axions transmitted through the optical barrier could be "regenerated" as photons and detected, in this case, by a Charge Coupled Device (CCD). Bottom: A diagram of helioscope experiment. Solar axions are converted into a photons by a large static dipole magnet. Photo Credit: Top: OSQAR Experiment [48]. Bottom: IAXO Experiment [50].

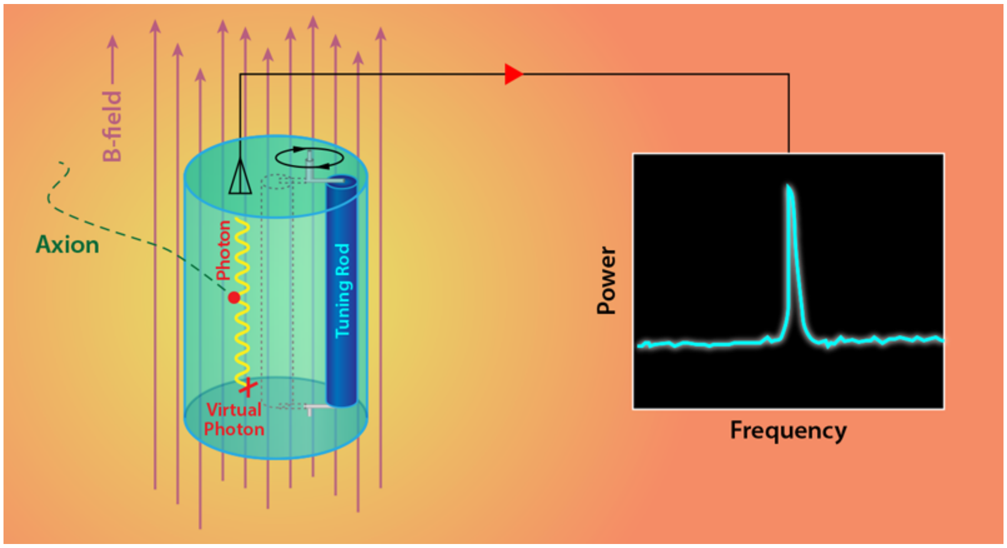

Figure 2.12: A diagram of the axion haloscope. PC: Scientific American.

is resonantly enhanced. Electromagnetic power from the cavity is then extracted by inserting an antenna into the cavity. A axion signal would be a peak above the noise in the cavity power spectrum. Because the axion mass is not known *a priori*, the resonant cavity must be tunable in order to search across a broad range of plausible axion masses.

The power expected from an axion signal is

$$\begin{aligned} P_{axion} = 2.2 \times 10^{-23}\ W \left(\frac{V}{136\ L}\right) \left(\frac{B}{7.6\ T}\right)^2 \left(\frac{C}{0.4}\right) \left(\frac{g_\gamma}{0.36}\right)^2 \times \\ \left(\frac{\rho_a}{0.45\ GeV cm^{-3}}\right) \left(\frac{f}{740\ MHz}\right) \left(\frac{Q}{30,000}\right) \end{aligned} \tag{2.13}$$

where $g_{a\gamma\gamma}$ is the axion-to-photon coupling, ρ_a is the local dark-matter density, m_a is the mass of the axion, B_{ext} is the external magnetic field, V is the cavity volume, f is the frequency of the photon, C_{lmn} is the form factor of the cavity (discussed below), Q is the quality factor of the cavity and f is the frequency of the axion signal. The form factor C_{lmn} parameterizes the overlap between the external magnetic field and the electric-field mode structure of the cavity, and is defined by

$$C_{lmn} = \frac{(\int dV E_{lmn} \cdot B_{ext})^2}{V B_{ext}^2 \int dV \epsilon_r E_{lmn}^2} \tag{2.14}$$

where E_{lmn} is the electric field of the cavity mode, B_{ext} is the external magnetic field, and ϵ_r is the relative permittivity within the cavity. In the case of the ADMX experiment, a cylindrical resonant cavity is placed inside a solenoid magnet. The magnetic field from the solenoid is along the axis of the cavity, and thus the optimal mode for searching for axions must have an electric field also directed along the axis of the cavity. For an ideal right cylindrical cavity, by symmetry only TM_{0m0} modes would couple to axions. Of those, the largest form factor is the TM_{010} mode. Higher order TM_{0m0} modes have components of the electric field that are both parallel and anti-parallel decreasing the overall form factor.

From the above equation, the power expected from an axion is extremely small, in the sub-yoctowatt range, requiring ultra-low noise electromagnetic detection to achieve a sufficient signal-to-noise ratio. The dominant noise in the experiment is Johnson noise from the physical temperature of the cavity plus additional noise from the receiver electronics, especially within the first stage amplifier. The total noise power from the experiment in a bandwidth B is

$$P_N = k_B B T_{sys} \tag{2.15}$$

where k_B is Boltzmann's constant, and T_{sys} is the system noise temperature of the experiment, which can be thought of as essentially the sum of the physical temperature of the cavity T_{cav} and the noise temperature of the receiver chain T_{amp}. The experiment therefore requires deep cryogenic temperatures and ultra-low noise receivers in order to adequately reduce the total noise temperature. The experiment signal-to-noise ratio (SNR) is then dictated by the Dicke-Radiometer equation as

$$SNR = \frac{P_{axion}}{k_B B T_{sys}} \times \sqrt{tB} \tag{2.16}$$

where P_{axion} is the power of the axion signal, t is the integration time, and B is the signal's bandwidth [52]. Throughout run 1B, ADMX had an instantaneous SNR for a KSVZ (DFSZ) axion of 0.04 (0.006) and after 100 seconds of integration an SNR of 11.66 (1.72).

2.6.1 Axion Lineshape

As mentioned earlier, an axion signal in a haloscope will take the form of a relatively narrow peak in the frequency power spectrum. The frequency of the signal is $f = E/h$, where E is is the total energy from the axion (rest mass plus small kinetic energy). Due to the kinetic energy, the signal will have a lineshape associated with the velocity distribution (the phase space) of axions in the vicinity of the laboratory.

In an overly-simple model, the axion dark matter in the Milky Way is treated as a pressure-less thermalized gas [53]. In this “isothermal sphere” model, the velocity dispersion of the axions then has a Maxwell-Boltzmann-like distribution. For an axion at 1 GHz, the axion signal is then distributed over a 700 Hz frequency bandwidth. This model is very likely too simple and more elaborate axion phase-space models have been proposed.

Perhaps the most reliable models are from N-body simulations for galactic-structure formation, where axions (bose particles) are the dark matter [54]. These simulations include effects from the infall history of the halo and interactions with baryonic matter and physics specific to bose dark matter. The phase space predicted from these simulations is Maxwellian-like but narrower. Compared with the “isothermal sphere” model, the width of the lineshape is about a factor of 1.8 times narrower [54]. Figure 2.13 shows a comparison of the differences between the two lineshapes. The narrower lineshape associated with the N-body simulation is beneficial from an experimental standpoint, because less integrated noise is under the narrower signal peak. The reduction in signal width corresponds to an increase in the signal-to-noise ratio of $\sqrt{1.8}$, as determined from equation 2.16.

In addition, there are, perhaps speculative, models where axions in a Bose-Einstein condensate form caustic ring-like structures [55]. The axion lineshape associated with such models is very narrow and therefore requires a higher resolution search to resolve. While ADMX does collect high resolution data in search of these caustic rings, this is done on a

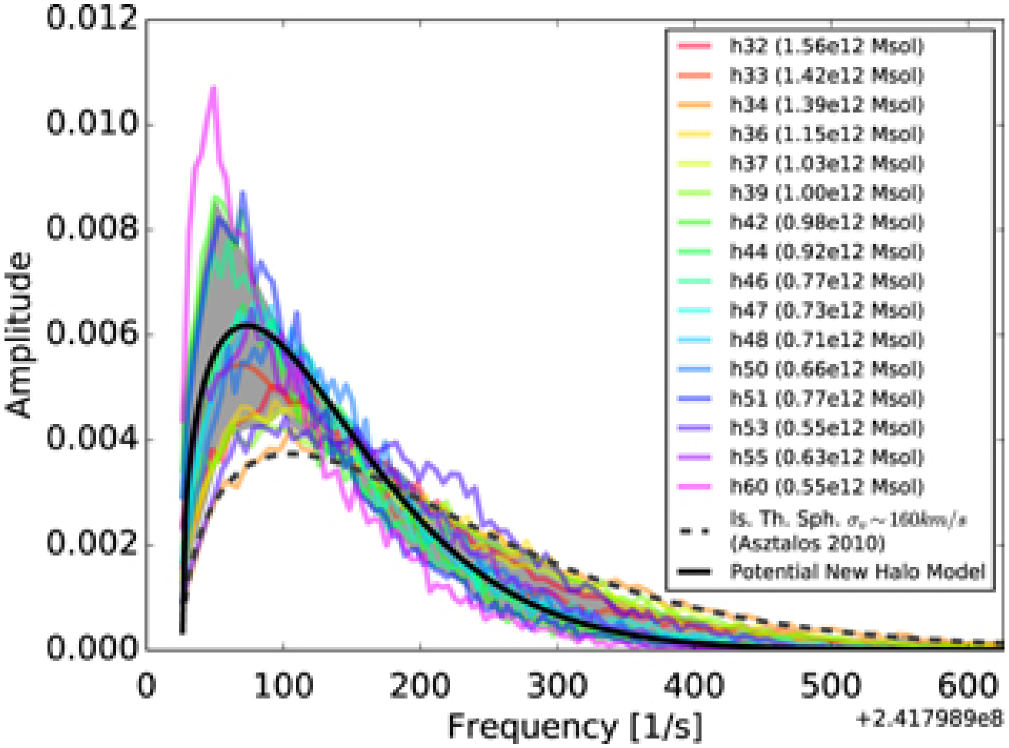

Figure 2.13: Axion lineshapes simulated for Milky-Way-like halos using N-body simulation software. The solid black line represents a fit to the models while the dashed line represents the lineshape predicted from the standard isothermal sphere model [54].

separate data-taking channel and will not be described in this thesis.

Chapter 3

EXPERIMENT

The Axion Dark Matter eXperiment (ADMX) is the world's most sensitive axion haloscope. In this chapter, I will provide an overview of the design and hardware used in ADMX, providing detail on how each subsystem of the experiment affects the sensitivity to axions. I will start with by introducing a brief history of ADMX. Then I will focus in on the individual subsystems of the experiment.

3.1 ADMX Experiment

3.1.1 Brief History

ADMX was designed to be the first implementation of the Sikivie haloscope with enough sensitivity to detect dark-matter axions with plausible masses and couplings [51]. It was appreciated early on that finally achieving this sensitivity would be a many-year project with many development steps. ADMX was first operated at Lawrence Livermore National Laboratory (LLNL), in California. While there, it became the first axion dark matter experiment to achieve sensitivity to a plausible QCD dark-matter axion (KSVZ) in the mass range of 1.9-3.3 μeV, masses where dark-matter axions could lie. Between 2005 and 2008, ADMX underwent a number of upgrades to improve its sensitivity including the integration of ultra-low noise quantum amplifiers based on Superconducting Quantum Interference Devices (SQUIDs). By collecting more data during 2008-2010, ADMX was able to expand the excluded axion mass range for KSVZ axion dark matter to 3.3-3.7 μeV [56]. However, ADMX had not yet been able to exclude the compelling DFSZ axion, a long-term goal of axion experiments.

In 2010, ADMX moved to the Center for Experimental Nuclear and Astrophysics (CENPA) laboratory at the University of Washington. At CENPA, ADMX underwent further upgrades including the integration of a dilution refrigerator to cool the cavity to temperatures on the order of 100 mK, thereby greatly improving the experiment sensitivity. Indeed, in 2016, ADMX became the first, and today still only, axion haloscope to exclude the more weakly coupled but highly compelling DFSZ axion with limits over the 2.66-2.81 μeV mass range. This great sensitivity was due to the increase in sensitivity from using a dilution refrigerator and Microstrip SQUID microwave amplifier (MSA) [57]. The mass coverage at that time was limited by the bandwidth of the MSA. In 2017, ADMX replaced the MSA with a Josephson Parametric amplifier (JPA), closely related to the MSA, as the first-stage microwave amplifier [58]. This allowed for a far greater mass range to be covered without the extraction of the insert and the replacement of the RF components. The results of the axion search using the JPA, known as “run 1B”, are the focus of this thesis.

3.1.2 Overview

Figure 3.1 shows a sketch of the experimental insert. The height of the insert was about 9 feet and during the axion search, the insert was lowered into a 7.6 T magnet bore via a crane. The room-temperature flange at the top of the insert was the interface of the room-temperature systems with the various cryogenic electronics and refrigeration systems in the insert.

The resonant cavity was located near the bottom of the insert. The cavity was threaded axially by a static 7.6 T magnetic field generated by a superconducting solenoid magnet. The cavity was cooled to 130 mK at the mixing chamber of the dilution refrigerator, which was bolted to the top of the cavity. Copper tuning rods extending axially along the full length of the cavity were used to tune the cavity resonant frequency. Two short wire antennae were inserted into the cavity. A antenna inserted into the top of the cavity allowed for extraction of power from the cavity into a sensitive microwave receiver. A second, smaller antenna inserted into the bottom of the cavity was used to transmit microwave power through the cavity to characterize the cavity parameters (e.g. determine the resonant frequency and loaded quality factor (Q) of the cavity).

Above the cavity was a “1-K stage” thermally connected to the “1-K pot”. Gearboxes that coupled the power-extracting antenna and cavity-tuning rods to room-temperature stepper motors were mounted to this thermal stage. In addition, the “hot load”, a component to calibrate the sensitivity of the receiver, was weakly thermally sunk to this stage.

Above the 1-K stage was a 4-K liquid-helium reservoir. This 4-K cold stage contained a “bucking-coil” magnet, used to generate a magnetic field-free region to house the field-sensitive quantum electronics. In addition, second-stage heterostructure field effect transistor (HFET) amplifiers were mounted to this thermal stage. Above the liquid helium reservoir were various thermal stages at various temperatures between 20-50K that provided thermal shielding to the colder stages of the experiment. See figure 3.1 for a sketch of the various thermal stages.

3.1.3 Scan Rate for Haloscopes

The scan rate for haloscopes is given by the equation

$$\begin{split}\frac{df}{dt} = 1.68GHz/year \left(\frac{g_\gamma}{0.36}\right)^4 \left(\frac{f}{1GHz}\right)^2 \left(\frac{\rho_0}{0.45GeV/cc}\right)^2 \left(\frac{5}{SNR}\right)^2 \\ \left(\frac{B}{8T}\right)^4 \left(\frac{V}{100l}\right)^2 \left(\frac{Q_L}{10^5}\right) \left(\frac{C_{lmn}}{0.5}\right)^2 \left(\frac{0.2}{T_{sys}}\right)^2 [59]\end{split} \tag{3.1}$$

where g_γ is the model dependent axion coupling, ρ_a is the local dark matter density, f is the frequency of the axion ($f = E/h$), B is the magnetic field, V is the cavity volume, Q_L is the loaded quality factor, C_{lmn} is the form factor of the cavity with mode indices l, m, and n, T_{sys} is the system noise temperature, and SNR is the target signal-to-noise ratio of the axion signal. Here g_γ, f, and ρ_0 are theory parameters, out of the control of the experimenter, while SNR, B, V, Q_L, C_{lmn}, and T_{sys} are parameters that characterize the experiment. A majority of this chapter details how the various experiment subsystems are designed to improve on those experimental parameters in order to optimize the scan rate.

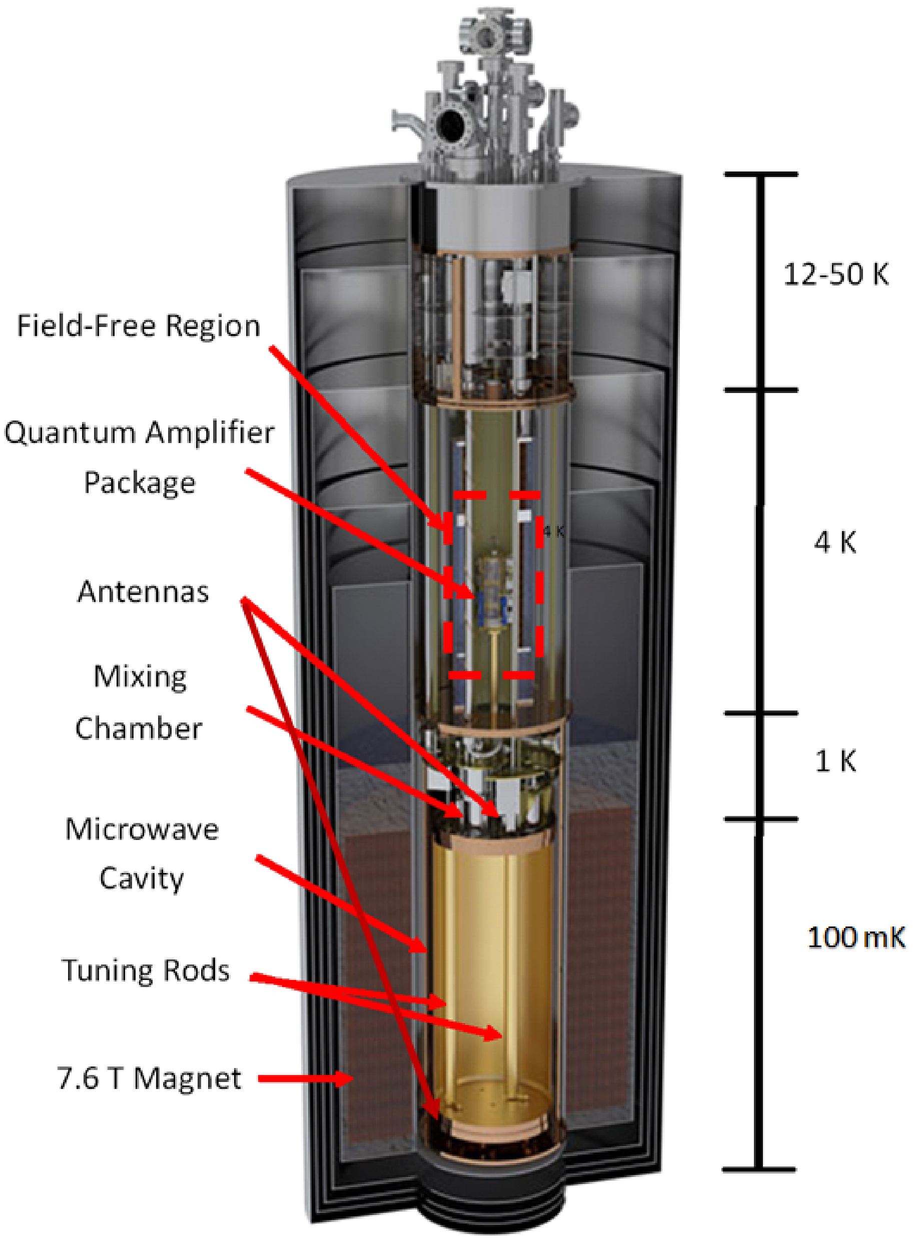

Figure 3.1: Cut-away sketch of the ADMX cryostat and experimental insert. The insert is lowered into the bore of a superconducting solenoid magnet and the cavity is tuned with two axial tuning rods. Some microwave power from the cavity is extracted by an antenna and amplified by a Josephson parametric amplifier (JPA), which is located in a field-free region.

3.1.4 Cooling

As mentioned in section 2.6, the dominant noise source in the experiment was Johnson noise from the cavity and the electronic noise from the receiver. The cavity was cooled using a custom high-flow dilution refrigerator developed at Janus research (now part of Lakeshore Cryogenics) in collaboration with our ADMX collaborators at the University of Florida.

A dilution refrigerator used a ^{3}He and ^{4}He mixture to achieve milli-Kelvin temperatures. When cooled to temperatures below 870 mK, a mixture of ^{3}He/^{4}He would undergo a phase separation into a concentrated ^{3}He phase and a diluted ^{3}He/^{4}He mixed phase. In a dilution refrigerator, this phase separation occured in the coldest part of the refrigerator, the “mixing chamber”. The ^{4}He was more or less static in the refrigerator where ^{3}He was introduced. Almost pure ^{3}He was pumped through the dilution refrigerator. In the mixing chamber, the pure ^{3}He underwent a transition from the pure phase to the diluted mixture. Entropy increased as the ^{3}He transitions from a pure phase into a more disorderly mixed phase, thereby absorbing heat from the environment. Thus, the phase transition of the mixture provided the cooling for the dilution refrigerator.

The other thermal stages of the experiment pre-cooled the ^{3}He mixture before it entered the mixing chamber and also recovered residual cooling. The “4-K stage” consisted of a large reservoir of liquid helium that was routinely topped up about once per day. The liquid helium in the reservoir supplied the two 1-K “pots” in the experiment. The 1-K “pots” were copper vessels partially filled with liquid ^{4}He. Pumping on the vapor above the liquid helium within the pots cooled the pots down to temperatures around 1 K. One of the 1-K “pots” pre-cooled the ^{3}He mixture (“the small 1K pot”) and the other established a 1-K thermal stage (“the big 1K pot”) for other cold components. During the run covered in this thesis, the dilution refrigerator had a cooling power of about 800 μW and the mixing chamber reached operating temperatures of about 100 mK. The mixing chamber, as shown in figure 3.2, was mounted directly to the top of the cavity and cooled the cavity down to temperatures of about 130 mK.

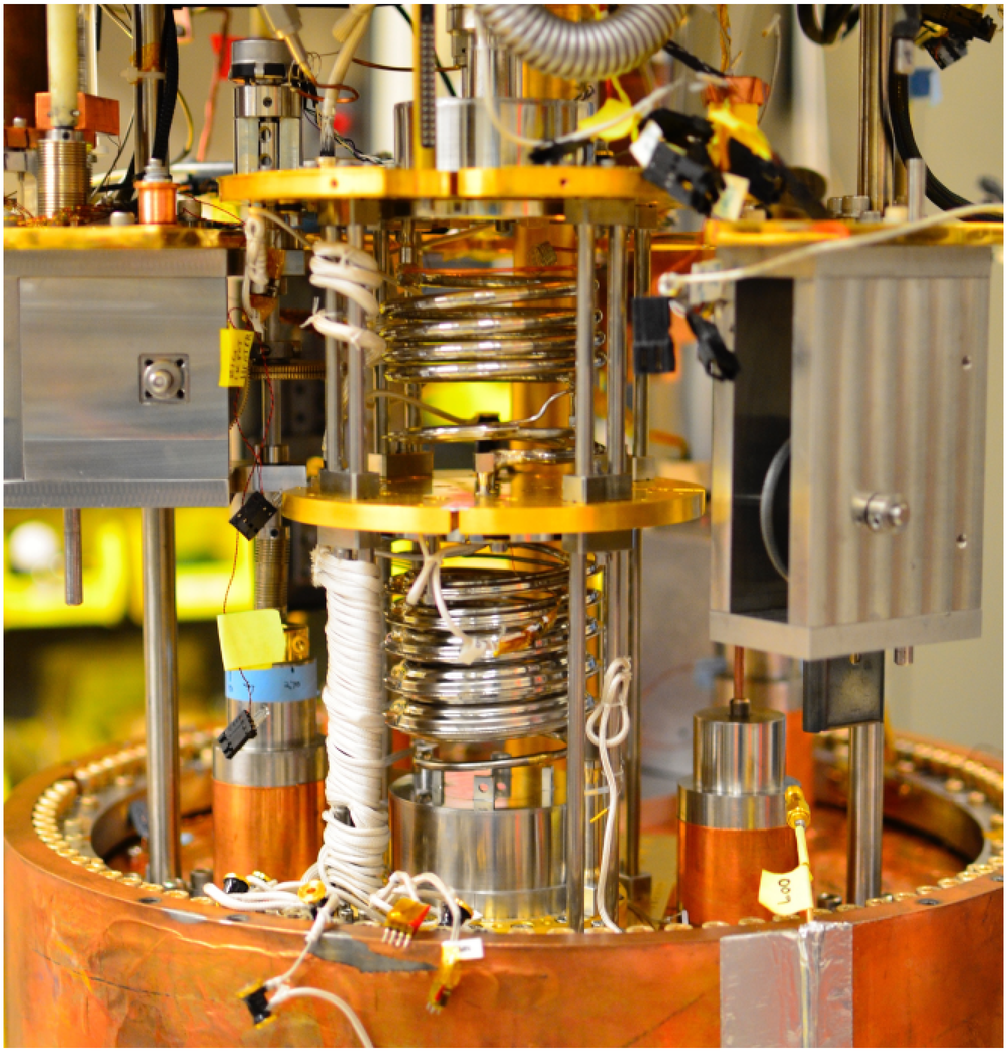

Figure 3.2: A picture of components of the ADMX dilution refrigerator. The coldest component, the mixing chamber is thermally sunk to the top of the cavity, cooling the cavity to about 130 mK. Above the mixing chamber are heat exchangers which pre-cool the nearly pure ^{3}He flowing into the mixing chamber.

The two superconducting magnets used by ADMX were both cooled in a bath of liquid ^{4}He. The bucking-coil magnet, which was integrated into the ADMX insert, was cooled by liquid helium in the reservoir; it was typically only partially submerged and kept cold with radiation shields at 4.2 K.

3.1.5 Liquefaction System

The large quantity of liquid helium required in the ADMX experiment practically necessitated the helium gas that evaporated be collected and re-liquefied. The ADMX helium liquefaction system is one of the largest in Washington state. The liquefaction system is shown in figure 3.3. ^{4}He gas from the experiment was first stored in a gas-bag buffer before being compressed into medium- and then high-pressure storage. High-pressure helium was fed into a liquefier to produce liquid helium (LHe). The resulting LHe was stored in a large-volume dewar to be later transferred into the experiment by an automated system.

3.2 Cavity

The resonant cavity used by ADMX was a right circular cylindrical cavity constructed from copper-plated stainless steel and is shown in figure 3.4. Without tuning rods, the volume of the cavity was 140.4 L, but with the addition of tuning rods, the volume of the cavity was 136 L. A small, weakly-coupled antenna was inserted in a fixed position at the bottom of the cavity. A variable-position antenna, the “strongly-coupled antenna”, was inserted at the top of the cavity and was used to extract some microwave power from the cavity. By varying the insertion depth of the antenna, we ensured that the antenna was well coupled to the cavity throughout the cavity tuning range.

If the axion mass were precisely known, the design of a resonator would be trivial. One could simply build a bare resonator with a resonant frequency matching the frequency of the axion signal and then integrate for a time long enough for the signal to develop at good SNR. However, because the axion mass is not precisely known, the cavity must be tunable to allow for a search across a range of possible axion masses. In the case of the ADMX experiment,

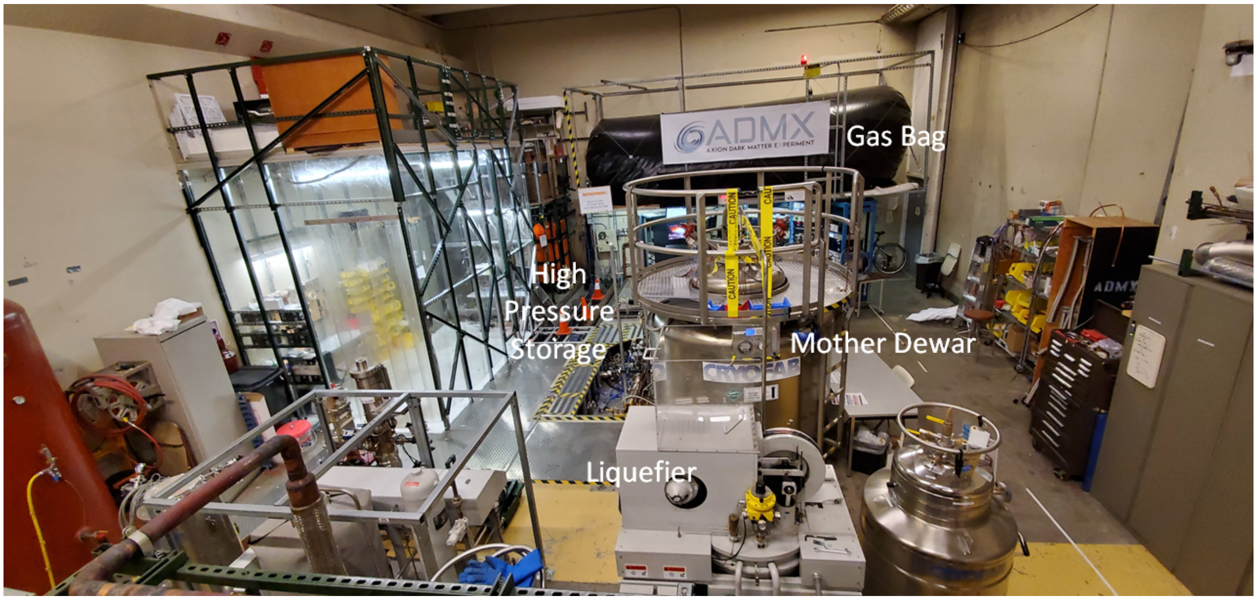

Figure 3.3: Picture of the ADMX gas-handling and liquefaction systems. Helium gas evaporated from the insert and main magnet was first collected into the gas bag before being compressed into medium- (Orange cylinder) and then the high-pressure storage. The liquefier stored LHe in a large "mother dewar".

the resonant frequency of the cavity was set by two copper tuning rods that extended axially the length of the cavity. Those rods could be rotated from near the wall of the cavity to near the center to change the cavity resonant frequency.

The tuning rods were attached at each end to sapphire shafts which extended to the outside the cavity. Sapphire is a dielectric material and the use of a dielectric material for the shafts was critical, because shafts made from conductive material would function as an antenna, allowing power to escape from the cavity by acting as a TEM waveguide. Sapphire, having an ultra-low cryogenic loss-tangent, was used to minimize degradation of the cavity quality factor due to dielectric losses. The sapphire shafts coupled the tuning rods to gearboxes mounted on the 1-K plate above the cavity. The gearboxes, in turn, were coupled to room-temperature stepper motors via a vacuum "wobble" feedthrough attached to G10 fiberglass shafts extending from the bottom of the insert's upper warm-temperature flange to the top of the 1-K plate. In tuning the cavity, the room-temperature stepper motors rotated the tuning rods inside the cavity at a gear ratio of 19,600 to 1, the gear reduction occurring in the "gearbox".

When the cavity is tuned to a given frequency, the frequency range over which the cavity is sensitive to axions is determined by its quality factor, Q. The quality factor is defined as

$$Q = \frac{f_r}{\Delta f} \text{ [60]} \tag{3.2}$$

where f_r is the resonant frequency of the cavity and Δf is the bandwidth of the cavity. The bandwidth of the cavity is defined as frequency range over which power transmitted through the cavity is at least half the power transmitted through the cavity on resonance. An almost equivalent definition for the quality factor is

$$Q = 2\pi \times \frac{U}{P_{lost}} \tag{3.3}$$

where U is the energy stored in the cavity and P_{lost} is the power dissipated per cycle by lossy elements in the resonator. For the resonant cavity, the lossy elements of the cavity were primarily the conductance of the walls (the RF surface resistance), the tuning rods of the cavity, and the antennae within the cavity. Dielectric losses in the sapphire are negligible. The total power losses of the resonator are decomposed as

$$P_{lost} = P_{cavity} + P_{antenna,strong} + P_{antenna,weak} \tag{3.4}$$

where P_{cavity} is the power lost from the conductance of the walls and tuning rods of the cavity, and $P_{antenna,strong}$ and $P_{antenna,weak}$ are the power lost from the strongly- and weakly-coupled antennae. Recall that $P_{lost} = 2\pi U/Q$ and the energy stored in the resonator is the same in each loss element, so equation 3.4 can be rewritten as

$$\frac{1}{Q_L} = \frac{1}{Q_{cavity}} + \frac{1}{Q_{Antenna,strong}} + \frac{1}{Q_{Antenna,weak}}. \tag{3.5}$$

where Q_L is the quality factor of the cavity with antennae inserted into the cavity and is known as the “loaded quality factor”. The quality factor of the cavity without antennae, Q_{cavity} is known as the unloaded quality factor. $Q_{Antenna,strong}$ and $Q_{Antenna,weak}$ are the quality factors of the strong and weakly-coupled antenna, respectively. The weakly-coupled antenna was of course only weakly coupled and therefore removed relatively little power from the cavity, so $Q_{Antenna,weak}$ had a negligible effect on the loaded quality factor. On the other hand, the strongly-coupled antenna extracted power from the cavity for the receiver chain, and therefore the total power lost from the cavity by the strongly-coupled antenna was more significant. The loaded quality factor would be strongly dependent on how well coupled the strongly-coupled antenna is to the cavity, which in turn was very sensitive to the insertion depths of the strongly-coupled antenna within the cavity.

3.2.1 Coupling to the Cavity

Recall there were two antennae inserted into the resonant cavity of ADMX. The weakly-coupled antenna at the bottom of the cavity was fixed in position and used to inject calibration signals into the cavity. The strongly-coupled antenna at the top of the cavity was used

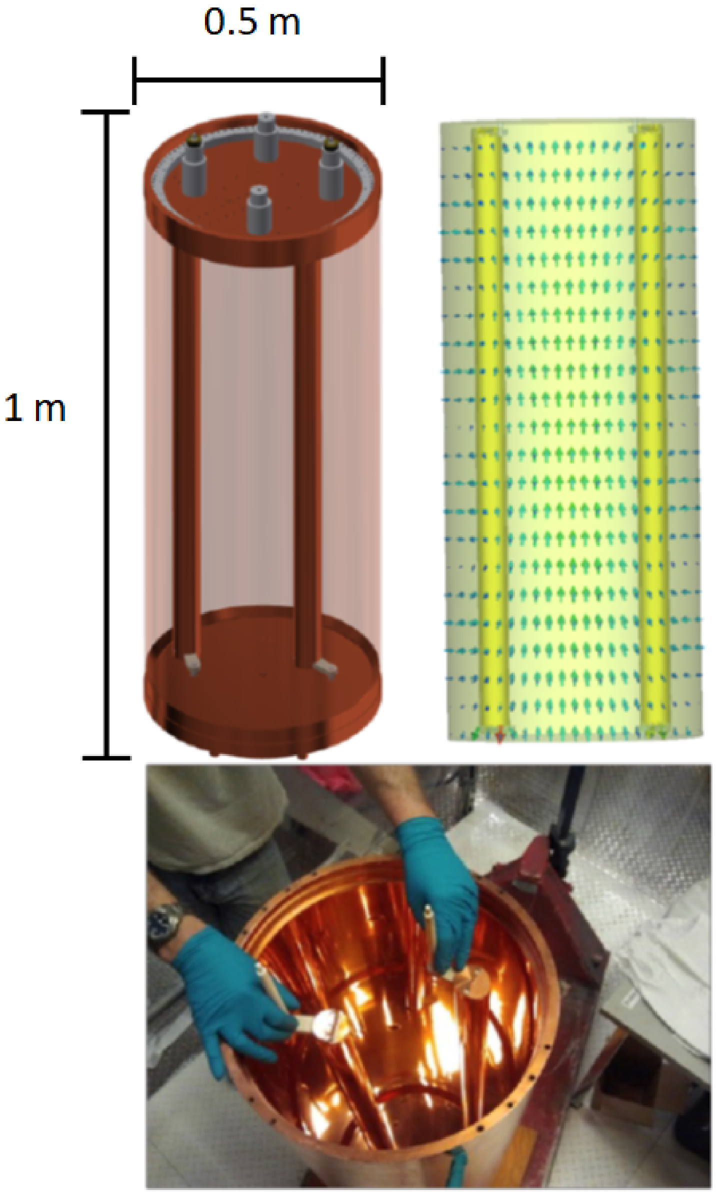

Figure 3.4: [Top Left]: A CAD model of the ADMX cavity including the two tuning rods. [Top Right]: A simulation of the electric field of the TM_{010} mode. [Bottom]: A photo of the ADMX cavity and tuning-rod system used in run 1B. The two 0.05 m diameter copper tuning rods are used to tune the resonant frequency of the cavity.

to extract power from the cavity for the receiver chain. The amount of power extracted by the strongly-coupled antenna depends on how well coupled the antenna is to the cavity. The coupling of the antenna could be adjusted by varying the insertion depth of the antenna into the resonant cavity.

At critical coupling, the impedance “looking in” at the antenna from outside the cavity equaled the impedance (50 Ω) of the transmission line. When the impedances were matched, the power in the cavity lost to the walls of the cavity and the power removed by the antenna were equal, so $P_{cavity} = P_{antenna,strong}$. Therefore, at critical coupling, half of the power of a signal within the cavity would be absorbed by the walls of the cavity and half would be extracted by antenna. Also, we observed that at critical coupling, the loaded quality factor was half the unloaded quality factor. While loaded quality factor varied across the rub 1B frequency range, a typical loaded quality factor was near 30,000.

3.2.2 Selecting the Cavity Mode

The mode structure of an ideal, empty, right-circular cylindrical cavity is relatively simple [60]. There are transverse magnetic (TM) modes in which the magnetic fields are perpendicular to the cavity axis, and transverse electric (TE) modes in which the electric fields are aligned perpendicular to the cavity axis. The addition of tuning rods and antennae inside the cavity introduces transverse electric (TEM) and other modes in the cavity.

In ADMX, the resonant cavity was placed inside the field of a solenoidal magnet. As discussed in section 2.6, the amount of power expected for an axion signal developed inside the cavity is dependent on the form factor, defined by

$$C_{lmn} = \frac{(\int dV E_{lmn} \cdot B_{ext})^2}{V B_{ext}^2 \int dV \epsilon_r E_{lmn}^2} \tag{3.6}$$

where E_{lmn} is the electric field of the cavity mode, B_{ext} is the external magnetic field, ϵ_r is the relative permittivity within the cavity, and the integral is performed over the cavity volume [51]. The form factor reflects the amount of overlap between the electric field of the cavity mode and the external magnetic field. For TE and TEM modes, the electric field is largely orthogonal to the external magnetic field, so the form factor is near 0. The modes of interest are those in which the electric field aligns with the field from the solenoid magnet, the TM_{0n0} modes. Because we wish to maximize the form factor, the integral $\mathbf{E}\cdot\mathbf{B}$ over the cavity volume, obviously the form factor is optimized in the TM_{010} mode.

Higher order TM_{0n0} modes introduce components of the electric field running both parallel and anti-parallel to magnetic field of the solenoid, reducing the total form factor. Future searches could use these higher order modes to search for higher frequency axions, but with reduced sensitivity compared to the searches on the TM_{010} mode.

Placing tuning rods into an ideal cylindrical cavity complicates the cavity mode structure. In particular, it introduces a number of weakly tuning (TE and TEM) modes. When the TM_{010} mode used in this search is tuned to near the same frequency as the weakly tuning modes, the modes mix and the shapes of those modes is complicated. At these "mode crossings", the two modes mix such that the electric field of the mode no longer aligns as well with the magnetic field from the external magnet. Section 4.3.3 will review the procedure for searching for axion signals at at frequencies near mode crossings.

3.3 Magnet

ADMX used two superconducting magnets. The main magnet, into which the resonant cavity is placed, was a large solenoid. While the magnet is rated to be operated at 8.5 T peak field, due to the risk of quenching, the magnet only operated at 7.6 T during run 1B data taking. In a magnet quench, the superconductor in the magnet transitions from superconducting to normal over a relatively short time. This transition can occur if a portion of of the conductor is heated to temperatures above the critical temperature or if the current through the coils exceeds the critical current. The current through the suddenly-resistive portion of the coils generates significant amounts of Ohmic heating. The heating rapidly boils off the liquid helium that cools magnet, and the current in the magnet rapidly decreases to 0. The rapid heating and changes in magnetic flux associated with a magnetic quench have the potential to significantly damage both the magnet itself and the ADMX insert, so great care needs to be taken to avoid a quench.

A number of cryogenic-receiver components in the experiment were magnetic field sensitive, requiring a near-zero magnetic field environment in which to operate correctly. Hence, a magnetic field-free region was created by a “bucking-coil” magnet. A sketch of the bucking-coil magnet is shown in figure 3.5. The bucking-coil magnet consisted of two coils, one to cancel the field from the main magnet and another counter-wound coil. Current through the counter-wound coil ran opposite to the current through the field-cancellation coil so that the mutual inductance between the main magnet and bucking-coil magnet was cancelled and there was a near-net-zero force between the bucking-coil and main magnet. The field cancellation from the bucking-coil magnet reduced the field in the region of the cryogenic receiver to less than 15 G. That was adequate to allow further field-reduction by passive magnetic shields. The quantum amplifiers in the experiment were given additional passive protection by placing them inside Cryoperm [61] shielding followed by superconducting shields.

3.4 ADMX Receiver

The primary purpose of the ADMX receiver was to amplify the signal power from the cavity while minimizing additional noise contribution from the receiver components. The low-noise aspect of the design of the receiver was crucial for optimizing the signal-to-noise ratio of a potential axion signal within the experiment. One of the key factors that affects the signal-to-noise ratio is the ordering of the radio frequency (RF) components of the receiver with lowest-noise gain stage first. As an example, for a receiver with three amplifiers in series, such as the one shown in figure 3.6, the total noise power from the receiver is

$$P_N = k_B B(G_1 G_2 G_3 T_1 + G_2 G_3 T_2 + G_3 T_3) \tag{3.7}$$

where G_i and T_i are the power gain and noise temperature of the i^{th} amplifier.

The series of amplifiers can modeled as an equivalent single amplifier with gain and noise equal to

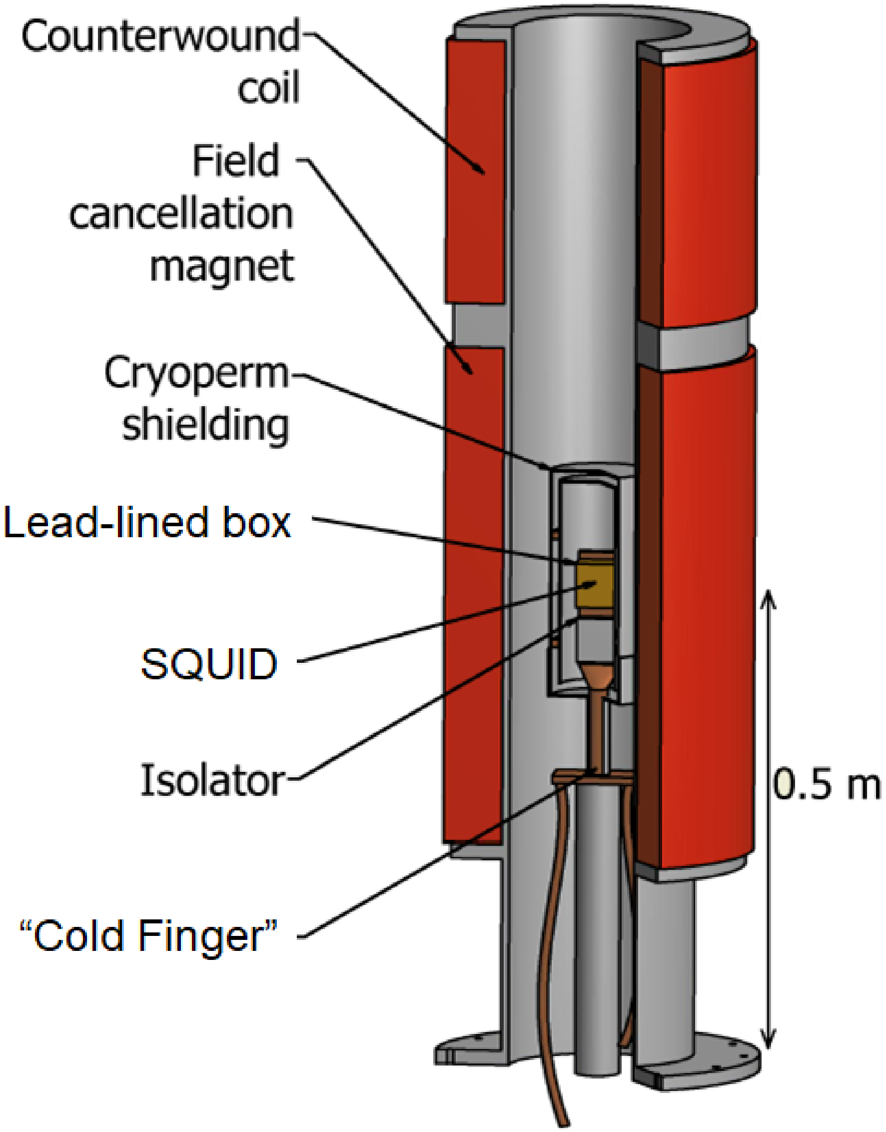

Figure 3.5: A sketch of the ADMX bucking-coil magnet and cryogenic-receiver package, called the "Squidadel". The bucking-coil magnet includes a counter-wound section to cancel the mutual inductance with the main magnet and maintain a net zero force between the two magnets. The Squidadel is placed in the field-free region established by the bucking-coil. The quantum amplifiers have additional passive shielding from the residual magnetic field [62].

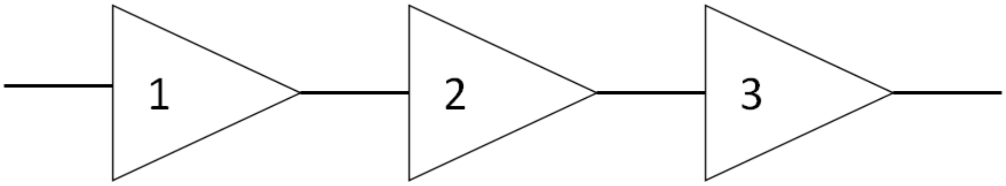

Figure 3.6: A receiver with 3 amplifiers in series.

$$G_{eq} = G_1 G_2 G_3 \tag{3.8}$$

$$T_{eq} = T_1 + \frac{T_2}{G_1} + \frac{T_3}{G_1 G_2}. \tag{3.9}$$

To minimize the equivalent noise temperature in the receiver, the lowest noise temperature amplifier should therefore be placed first in the receiver chain. The noise contribution from subsequent amplifiers will then be reduced by a factor equal to the total gain of the previous amplifiers.

The first amplifier used in the ADMX experiment was an ultra-low noise quantum amplifier based on Superconducting QUantum Interference Devices (SQUIDs). This was followed by a broadband cryogenic amplifier from Low Noise Factory [63]. These cryogenic amplifiers along with other RF components inside the ADMX insert together were collectively refered to as the "cryogenic receiver". The receiver components outside the insert at room temperature, were collectively called the "warm receiver". In this section, I will review both sections of the ADMX receiver.

3.4.1 Cryogenic Receiver

A schematic of the cryogenic receiver for ADMX is shown in figure 3.7. the strongly-coupled antenna inserted into the top of the cavity extracted some power and fed it into the cryogenic receiver, where it was amplified and sent to the warm receiver. In this section, I discuss the various components in the cryogenic receiver.

Circulators C_1, C_2, and C_3 in figure 3.7 are 3-port ferromagnetic devices, as shown in

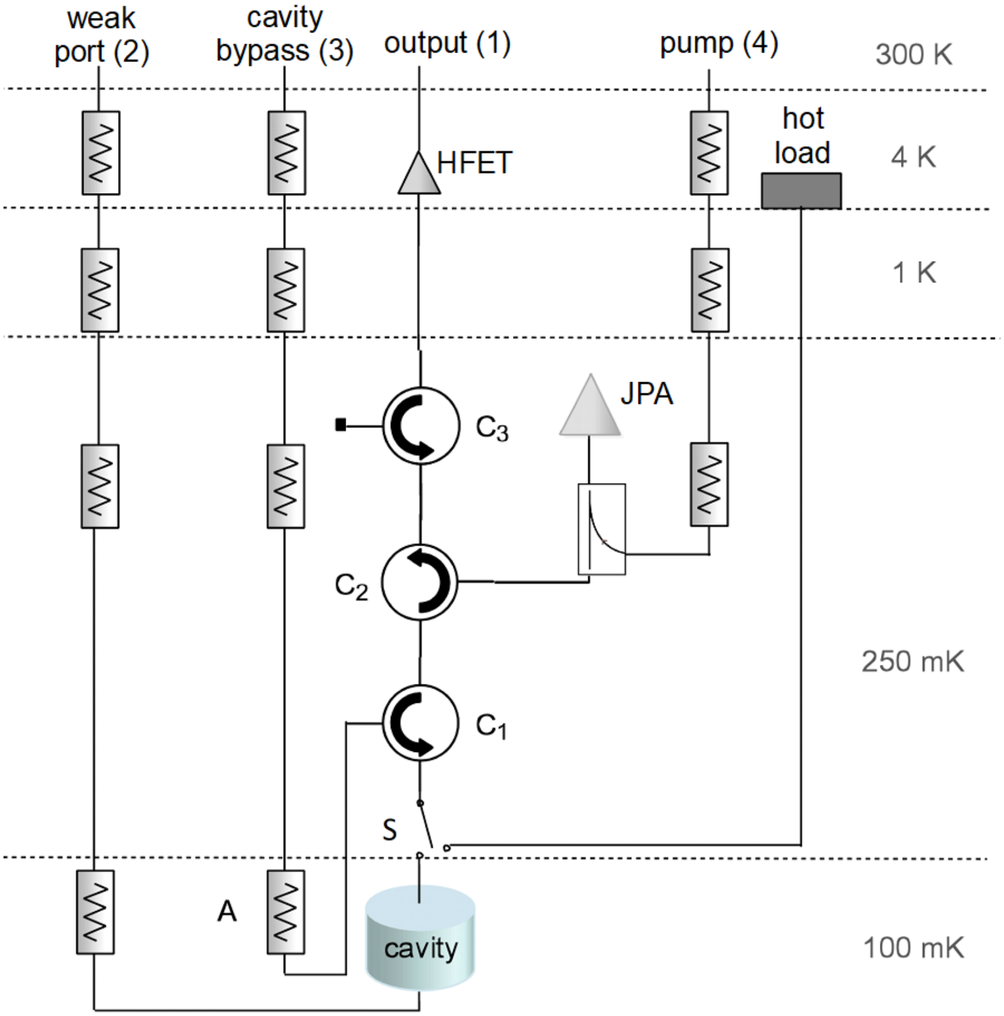

Figure 3.7: The schematic of the ADMX cryogenic receiver. C_1, C_2, and C_3 are circulators. JPA is the Josephson parametric amplifier and HFET is a heterostructure field-effect transistor amplifier. Both amplifiers are used to amplify power from the cavity. The pump line is used to supply a pump tone to the JPA. Switch S can be toggled between the cavity and the hot load for noise calibration measurements.

figure 3.8 [64]. Circulators are non-reciprocal devices that direct signal through the circulator in only one direction (1→2, 2→3, 3→1). For example, power input into port 1 of the circulator is sent out of port 2 with a small amount of loss, and isolated from port 3. The direction of power flow in the circulators in indicated in figure 3.7 with counter-clockwise arrows.

Switch S is a solenoid switch used to change the input of the cryogenic receiver to either the output of the cavity or a "hot load" used for calibration of the system noise temperature. The calibration operation will be discussed further in section 4.7. To actuate the switch, 160 mA DC current was applied to the switch for about 1 second. Actuation of the switch caused considerable heating in the cryogenic receiver, so it was actuated sparingly.

The attenuators (A) mounted at each thermal stage of the experiment served as thermal sinks for the receiver coaxial lines. In addition, the attenuators reduced the thermal noise being deposited into colder components of the receiver from warmer spaces.

The line labeled "weak port" (2) connected to the weakly coupled antenna at the bottom of the cavity. This enabled transmission measurements through the cavity. These measurements were used to characterize the resonant cavity including the resonant frequency and loaded quality factor (Q) of the cavity. In addition, the weak port was used to inject synthetically generated axion signals into the cavity; we'll discuss this powerful capability of ADMX later. The receiver coaxial cables on the weak port line were stainless steel flashed with copper in order to minimize the heat conduction between thermal stages.

The line labeled "cavity bypass" (3) was a receiver line that bypassed the resonant cavity. Power transmitted through the cavity-bypass line was reflected off of the strongly coupled antenna on the cavity. This line was used in reflection measurements which measure the portion of power reflected off the antenna as a function of frequency. These measurements determined how well-coupled the strongly-coupled antenna is to the mode of the cavity. In addition, the cavity-bypass line was used to characterize the overall health of the cryogenic receiver.

The line labeled "output" (1) connected the output of the cryogenic amplifiers to input of

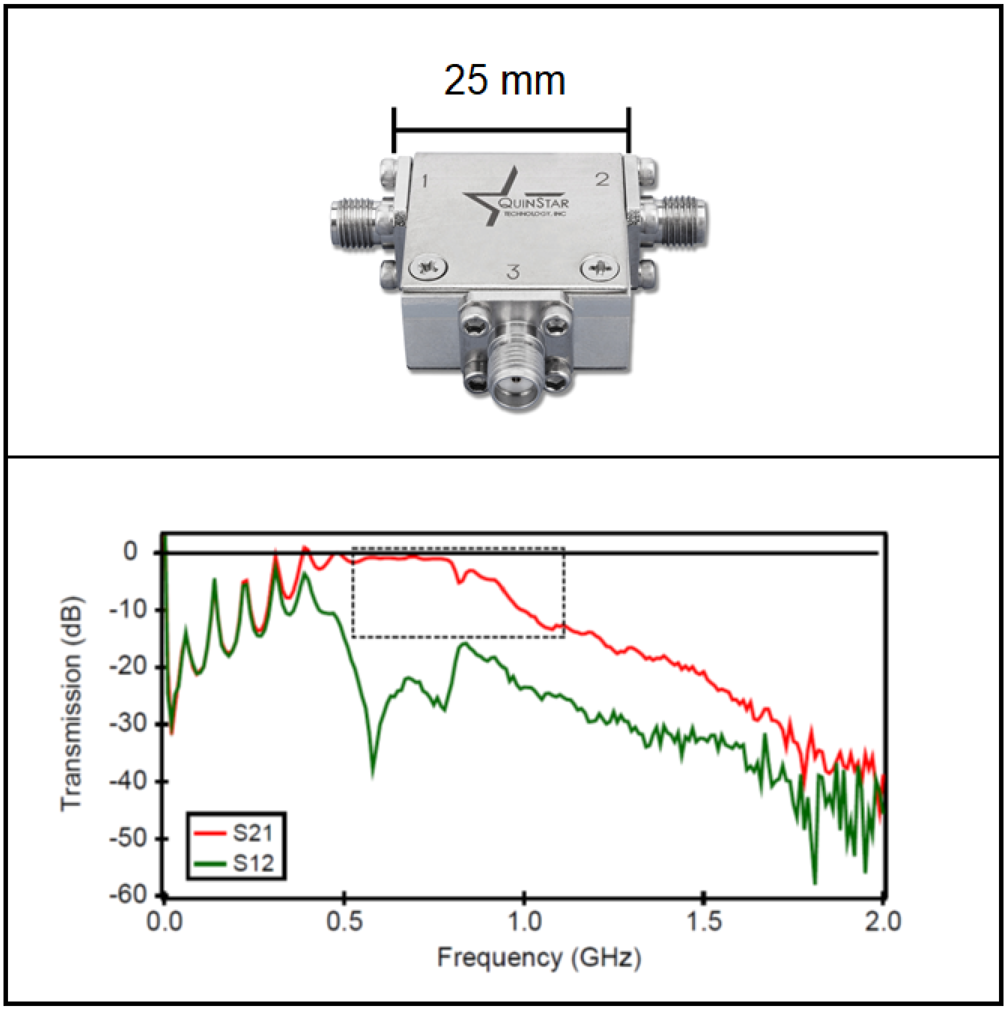

Figure 3.8: [Top]: A photo of a circulator used in ADMX. Circulators are non-reciprocal devices that direct power in only one direction. For instance, power incident on port 1 is sent to port 2, but isolated from port 3. [Bottom]: The measured transmission and isolation in dB for a circulator used in ADMX as a function of frequency. S_{21} indicates a transmission measurement where power is input on port 1 and measured at port 2, while S_{12} indicates a measurement where power is input on port 2 and measured at port 1. As expected, power is transmitted from port 1 to port 2, and the signal from port 2 to port 1 is isolated with at least 20 dB of power isolation. Note the useful bandwidth of the circulator is 600-800 MHz.

the warm receiver. Among other things, this receiver line was used to amplify and measure the signal being output from the cavity. In order to minimize attenuation of the signal from the cavity, superconducting receiver coaxial cables were used in the output line up until the input of the HFET amplifier. The exception to this was the connection between the strongly-coupled antenna and the input of the switch, which was made using a more flexible copper flashed stainless steel coaxial cable in order to accommodate variations in the insertion depth of the antenna.

3.4.2 Josephson Parametric Amplifier (JPA)

A Josephson Parametric amplifier (JPA) is an ultra-low noise quantum amplifier used as the first-stage amplifier by ADMX. The JPA used by ADMX was designed at the University of California-Berkeley [65] and fabricated at the National Institute of Standards and Technology.

A Josephson Parametric amplifier consists of two Josephson junctions placed in a SQUID loop and in parallel with a capacitor. An equivalent-circuit diagram for a JPA is shown in figure 3.9. The JPA behaves like an LC circuit with a resonant frequency equal to

$$\omega_{JPA} = \frac{1}{\sqrt{(L_J + L_G)C}} \tag{3.10}$$

where L_J is the Josephson inductance in the SQUID loop, L_G is the geometric inductance of the equivalent circuit, and C is the capacitance of the capacitor placed in parallel with the SQUID loop. The Josephson inductance is determined by

$$L_J = \frac{L_{J0}}{\sqrt{1-(I/I_0)^2}} = L_{J0}(1 + \frac{1}{2}(I/I_0)^2 + ...) \text{ [66]} \tag{3.11}$$

where I is the current through the junction, I_0 is the critical current of the junction, and L_{J0} is the Josephson inductance in the absence of any current through the junction. The critical current is the maximum supercurrent that can flow through the SQUID. The resonant frequency of JPA, ω_{JPA}, is tuned using a externally applied magnetic flux threading the

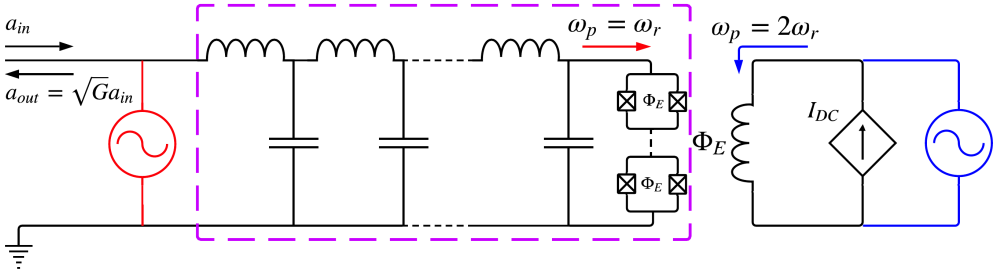

Figure 3.9: An equivalent-circuit model of the JPA. The JPA consists of an array of SQUIDs placed in series with a capacitance in parallel. A separate DC field is inductively coupled to the JPA allowing for tuning of its resonant frequency. The JPA can be either current or flux-pumped. In the current-pump design, the pump tone is input into the main transmission line (Red), whereas in the fluxed pump design, the pump tone is input into the inductively-coupled DC line.

SQUID loop, to change the critical current of the Josephson junction, I_0, thereby changing the Josephson inductance.

The JPA makes use of parametric amplification to amplify the power of a signal. In the JPA, parametric amplification is achieved by varying the inductance of the JPA by a pump tone. The JPA used by ADMX used a “current-pump” design in which the signal and pump tone were combined input into the main RF transmission line. In this design, the modulation of bias current through the Josephson junctions varies the resonant frequency of the JPA, allowing for parametric amplification of the signal from the cavity. The pump tone is supplied to the JPA by the RF line “JPA pump”.

The JPA was controlled by three parameters, the DC bias current, the power of the pump tone, and the frequency of the pump tone. The gain of the JPA was optimal when the frequency of the pump tone, ω_P, matched the frequency of the incoming signal tone, ω_S. However, in order to decouple the pump tone from the signal from the cavity, the pump tone frequency was offset from the signal frequency by 375 kHz. The 375 kHz offset also allowed use of bandpass filters to remove the pump tone before digitizing the voltage from the receiver.

Over the course of the run, the JPA provided at least 20 dB gain over a 10-20 MHz instantaneous bandwidth. While this bandwidth by itself would have been insufficient to cover the whole run range for ADMX, the resonance of the JPA was tuned by adjusting the DC bias current and pump tone power. This adjustment was done approximately every 10 minutes to ensure that the JPA maintained good gain and low noise across the bandwidth of the cavity.

It should be noted that the design of the JPA was unconventional for an amplifier. In conventional amplifiers, the signal is input into one port and the amplified signal is output by a separate port. However, the JPA was a single port device and lacks a conventional input and output port. Instead, the signal incident on the JPA input was amplified and sent backwards. Amplifying signals in this manner risked reflecting amplified noise back into the cavity. However, the circulators C_1 and C_2 isolated the amplified signal from the cavity and directed the amplified signal towards the cryogenic HFET amplifier.

3.4.3 HFET Amplifier

An HFET amplifier is a broadband device used as the second-stage amplifier in the ADMX receiver. The HFET amplifier used by ADMX was purchased from Low Noise Factory, and is shown in figure 3.10 (Top) [63]. It was biased with a drain voltage and current and provided at least 30 dB of power gain with a noise temperature of about 4.2 K over a 0.3-14 GHz bandwidth. A plot of the cryogenic behavior of the HFET is shown in figure 3.10 (Bottom).

The HFET amplifier was mounted to the bottom of the 4-K liquid helium reservoir. During operations, it was observed that when the HFET amplifier was placed inside a magnetic field the HFET channels were perpendicular to the magnetic field, the noise temperature of the HFET was higher than expected, about 8 K. A plausible model that explains the increase in noise temperature is that Lorentz forces acting on electrons in the HFET channels affected the electron path, which increased the noise temperature of the HFET. In future runs, this effect will be corrected for by orienting the HFET such that the input and output of the HFET are properly aligned with the magnetic field.

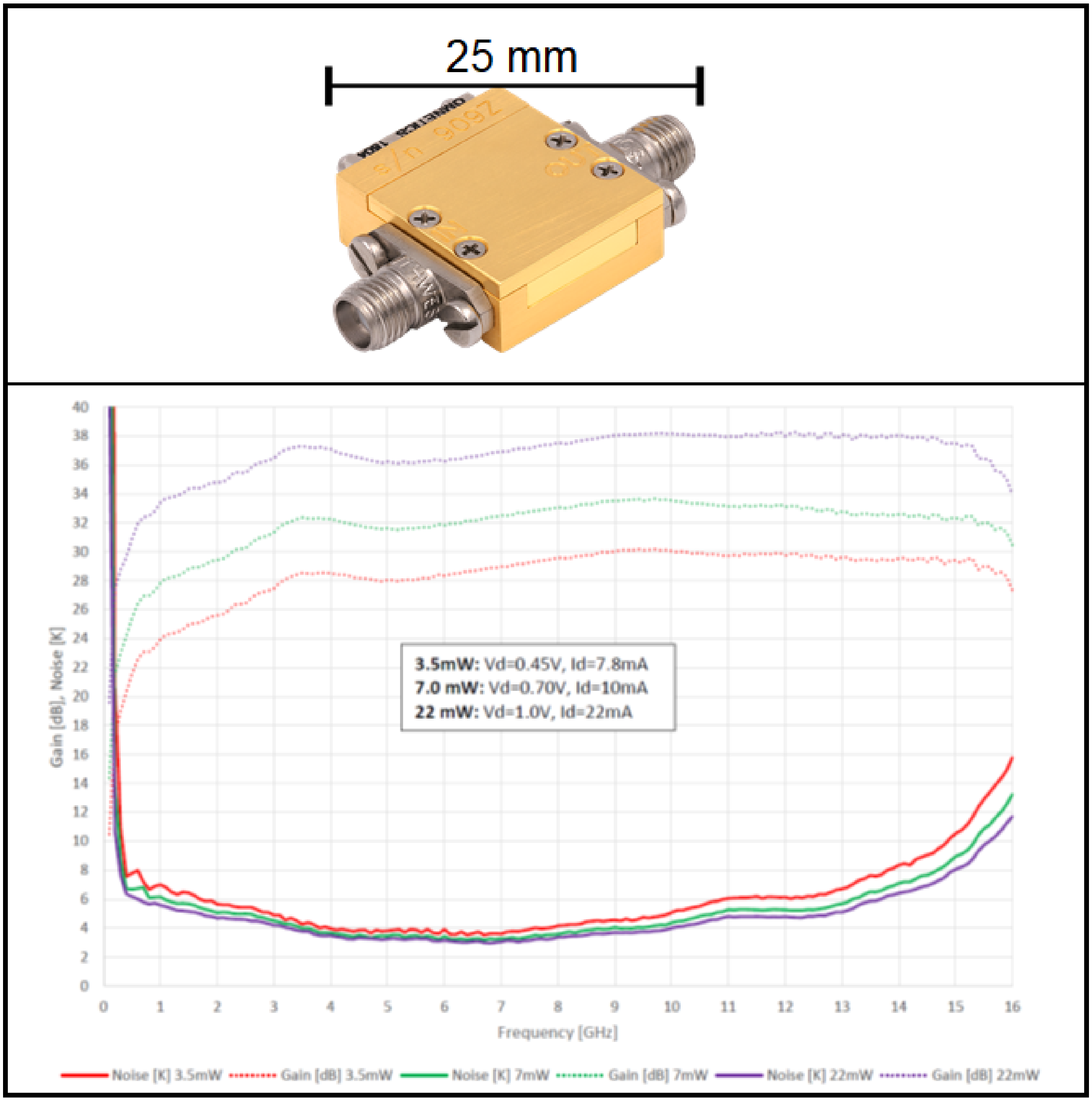

Figure 3.10: Top: A picture of the HFET amplifier purchased from Low Noise Factory and used as the second-stage amplifier in the cryogenic receiver. Bottom: A plot of the gain and noise temperature vs. frequency of the amplifier at 4 K at several biases. The amplifier has at least 30 dB of gain over a broad frequency range.

3.4.4 Squidadel

The most field-sensitive components in the receiver were the circulators (C_1... C_3), switch S, and the JPA are packaged together into what was called the “Squidadel”, shown in figure 3.11. These components were housed in the field-free region provided by the bucking-coil magnet. The Squidadel was cooled by a “cold finger”, a large copper rod that thermally coupled the Squidadel to the mixing chamber. A Hall probe mounted to the bottom of the 4-K liquid helium reservoir was responsible for a “touch” to the Squidadel, which caused minor heating. The thermal touch caused the operating temperature of the Squidadel to be higher than the mixing chamber temperature, around 230 mK.

3.4.5 Warm-Receiver Package

The warm-receiver package consisted of the RF components located in the laboratory at room temperature. One purpose of the warm receiver was to facilitate the transmission, reflection, and digitization measurements performed in the experiment. In addition, an additional room-temperature amplifier connected to the output of the cryogenic receiver provides additional gain and noise reduction.

A Keysight E5071C Network analyzer (NA) was used to measure the swept responses of the insert [67]. It output swept power over a broad frequency range into the insert and simultaneously measured the proportion of power coming out of the receiver. For transmission and reflection measurements, a RF switchbox connected the output of the NA to the weak port and cavity bypass lines, respectively.

A digitizer was used to measure the power output from the cavity. The digitizer used by ADMX was a Alazar PX1500 digitizer [68]. The digitizer sampled the voltage as a time series from cavity and receiver at a sampling rate of 200 Megasample per second, which was then downsampled to 25 Megasamples per second. The voltage time series was Fourier transformed and then squared in order to convert the voltage time series into the power spectrum from the cavity.

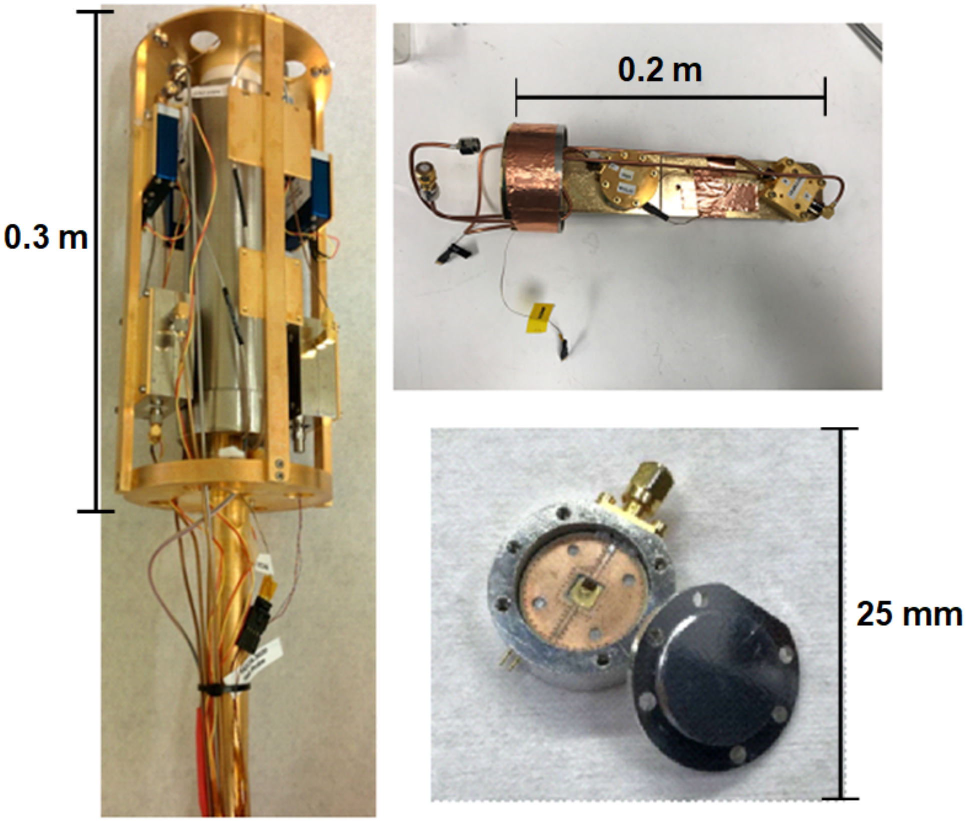

Figure 3.11: [Left]: A photo of the "Squidadel", the cryogenic-receiver package. Various switches and circulators are on the outer layer of the Squidadel. In the center, surrounded by a μ-metal shield are the field-sensitive quantum amplifiers. [Top Right]: A photo of the quantum amplifiers contained inside the passive superconducting shielding. [Bottom Right]: A photo of the JPA used by ADMX.

When measuring power from the cavity in search of an axion signal, the RF switchbox connected the weak port line of the cryogenic receiver to a terminator in order to prevent any noise from being injected into the cavity. The voltage output from the cavity and receiver was mixed-down with a local oscillator to an intermediate frequency of 10.7 MHz and measured as a voltage time series by the digitizer. Bandpass filters between the mixing stage and the digitizer removed the JPA tone and local oscillator tones as well as any additional wide band noise that before the signal was measured by the digitizer

3.5 Synthetic Axion Generator System (SAG)

In 2018, ADMX integrated a Synthetic Axion Generator(SAG) system into the experiment, which injected axion-like signals into the cavity. This system was powerful for testing the responses of both the ADMX receiver and the analysis procedures for axion-like signals in the cavity. The SAG system mainly consisted of an arbitrary-function generator and local oscillator, as shown in figure 3.12. The arbitrary-function generator produced a Maxwell-Boltzmann waveform similar to that predicted from the standard halo model for axion dark matter. The input function programmed into the arbitrary function generator was

$$f du = \left(\frac{3}{2\pi}\right)^{1/2} \frac{du}{r} e^{-1.5(r^2+u)} sinh(3r\sqrt{u}). \tag{3.12}$$

where $r = 0.85$ is the ratio of the velocity of the Sun through the Galaxy to the root mean square halo velocity [53].

The signal produced by the arbitrary-function generator was mixed up to a higher frequency within the search range of the experiment with a local oscillator. The frequencies (masses) of the synthetic axions were selected by a designated “blindness czar” in the Collaboration. These synthetically-generated tones were then injected into the cavity through the cavity’s weak port. The power of the synthetic axion signal was set by the output power of the arbitrary function generator, while the nominal local-oscillator power was kept constant at 13 dBm. Figure 3.13 shows a plot of a power spectrum from the cavity with a synthetic axion injected into the cavity at the cavity’s resonant frequency.

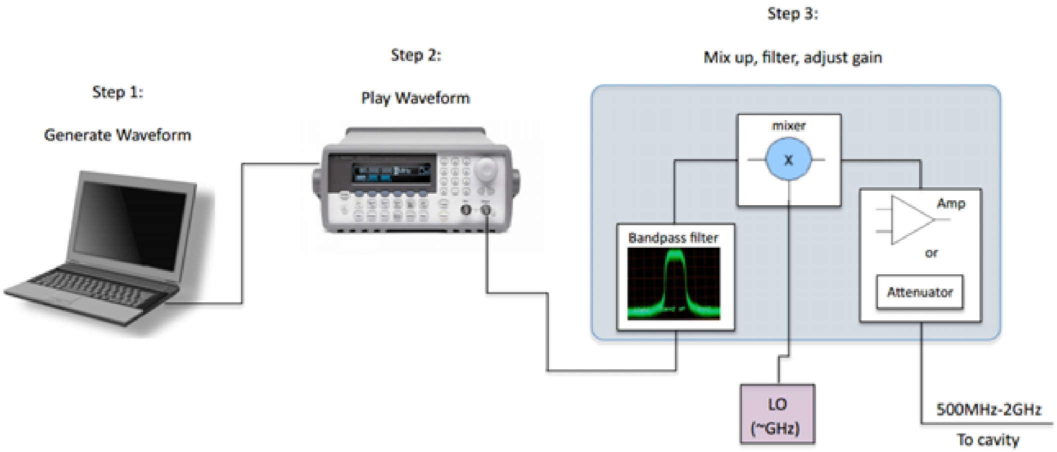

Figure 3.12: Diagram of SAG system.

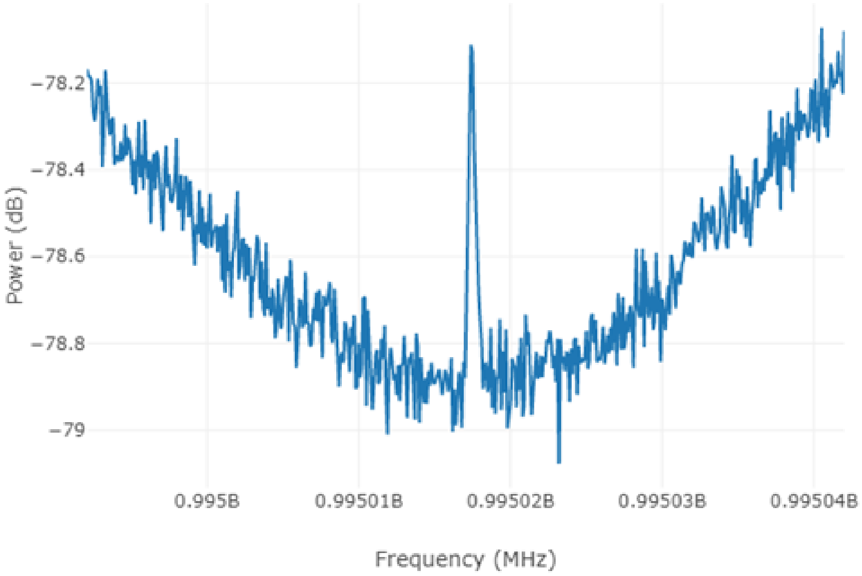

Figure 3.13: A plot of the digitized power at the output of the receiver chain as a function of frequency. Here, a synthetic axion was injected into the cavity at the resonant frequency is visible as a line near the center of the spectrum.

3.5.1 Calibrating the Power of the Synthetic Axion

To calibrate the power of the synthetic-axion signal being injected into the cavity, synthetic-axion signals at a known frequency were injected into the cavity at powers above the noise floor of the experiment. The power from the receiver was sampled and the amplitude of the synthetic-axion signal was recorded. The power output from the arbitrary-function generator was then varied and the power from the receiver would be re-sampled. The results of the calibration are shown in figure 3.14. An extrapolated linear fit determined what output powers on the arbitrary function generator corresponded to an injected power in the cavity that was consistent with a “KSVZ-” and “DFSZ-like” axion signals.

3.6 Sensor Package & DC Wiring

The numerous thermal stages and subsystems in ADMX required a large array of sensors to monitor the state of the system. These sensors included temperature sensors, Hall probes, and position encoders. The experiment made use of several DC wire bundles to connect the sensors to room temperature instruments stored in the ADMX data acquisition (DAQ) rack. The DC wiring bundles were run through a number of “breakout boxes” within the insert that are thermally sunk to the various thermal stages of the experiment; this avoided loading the various temperature stages. A general layout of the breakout boxes is shown in figure 3.15. In addition, these bundles provided DC power to components such as heaters and amplifiers.

3.6.1 Temperature Sensors

The temperature sensors used in ADMX were all 4-wire Resistance Temperature Detectors (RTDs) [69]. RTDs were chosen for their accuracy and wide range of operating temperatures. The temperature sensors used in the ADMX insert were Cernox temperature sensors, thin-film ZrN/ZrO sensors developed by Lakeshore Cryotronics, and Ruthenium Oxide sensors [70]. The Cernox sensors exhibited large magneto-resistances at temperatures less than 1 K,

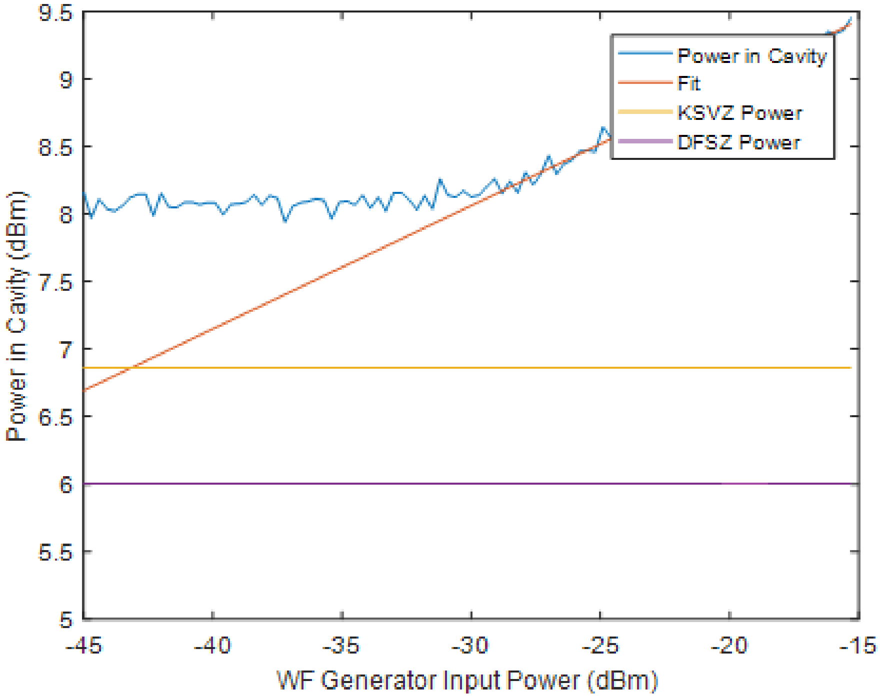

Figure 3.14: A plot of the measured power of a synthetically generated axion signal injected into the cavity and amplified as a function of the programmed input power of the synthetic axion injection.. By varying the input power of the synthetically generated axion, the output power of the SAG system varied. The power injected into the cavity was measured at several input powers, and an extrapolated linear fit established the input power for “KSVZ” and “DFSZ-like” axion signals.

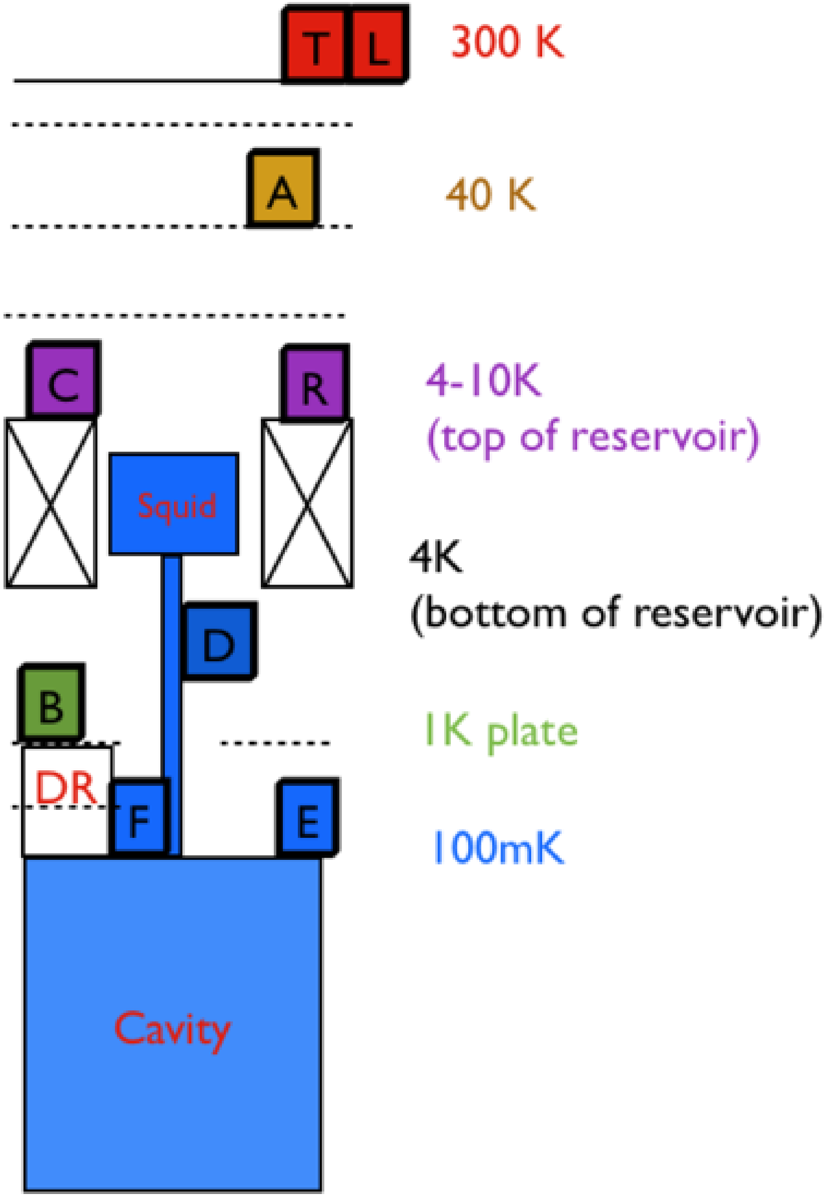

Figure 3.15: A diagram of the of the DC-wiring layout for ADMX. The “breakout boxes” are mounted to various thermal stages within the insert and allow connection of the wire bundles to the individual sensors on the insert. The wire bundles eventually connect to room-temperature feedthroughs at the top of the insert.

so Ruthenium Oxide sensors were used in regions near the main magnet.

The majority of temperature sensors used generic calibration curves provided by the manufacturer. However, several temperature sensors for critical higher-accuracy measurements were purchased with individual high-precision calibrations. These individually-calibrated sensors included the temperature sensors for the hot load, the cavity, and the Squidadel.

Temperature sensors were mounted on each of the thermal stages of the experiment and monitored temperature throughout the run. In the case of the LHe reservoir, cavity, and the Squidadel, sensors were mounted at both the top and bottom in order to monitor thermal gradients across the bulk. Figure 3.16 shows the temperature sensors mounted to the top and bottom of the cavity, these sensors found the temperature differential across the cavity to be less that 3 mK when the cavity during operation.

Two separate instruments read out temperature sensors on the ADMX insert. The majority of temperature sensors were monitored using an Agilent AG34980A Multifunction Multiplexer [71]. For temperature sensors in the milli-Kelvin stage, a Lakeshore Model 370 AC resistance bridge was used [70]. Additionally, sensors that require high accuracy, such as the temperature sensor for the hot load, were also measured using the Lakeshore AC resistance bridge. The Janus dilution refrigerator had its own set of temperature sensors for its mixing chamber, intermediate cold plate (ICP), still, and small 1K pot, which were read out with a separate Lakeshore Model 370 AC resistance bridge.

3.6.2 Hall Probe

Hall probes were used in the insert to monitor the magnetic filed in the field-free region. The Hall probes, when energized, were biased with 100 mA of current. Because, when energized, the Hall probes were a significant heat load within the experiment, the Hall probes were only powered on during magnetic-field ramping operations. In addition, a weak thermal "touch" between the bottom hall probe and the Squidadel prevented us from energizing the bottom Hall probe, so only the top Hall probe was used. During the ramp, the top Hall probe was energized and used to ensure that the field in the field-free region did not exceed 15 G, which

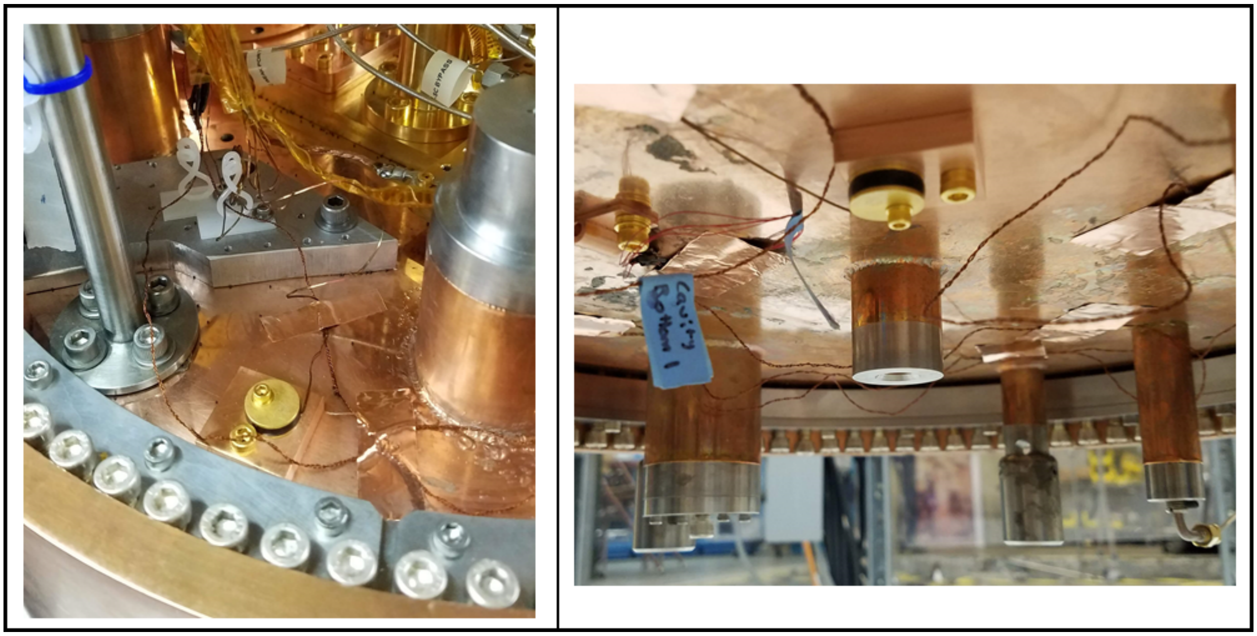

Figure 3.16: [Left]: Ruthenium Oxide temperature sensor mounted to the top of the cavity. [Right]: Ruthenium Oxide temperature sensor mounted to the bottom of the cavity.

would have started to penetrate the passive shielding surrounding the JPA.

3.6.3 Heaters

A number of resistive heaters were mounted to refrigeration components and elsewhere inside the experiment, as is found in almost all cryogenic apparatuses. These were used primarily during the warm-up of the insert to boil off excess liquid helium. A heater on the hot load was critical for to calibrating the experiment noise temperature; a procedure discussed in section 4.7. Additionally, a heater on the "still" of the dilution refrigerator was used evaporate ^{3}He for recycling through the dilution refrigerator gas system.

3.6.4 Data Acquisition and Controls

The sensors in ADMX were readout through several instruments, including the Lakeshore Model 370 AC resistance bridge [70] and Agilent AG34980a "Muxer" [71]. These instruments were controlled by the Experimental Physics and Industrial Control System (EPICS) software developed at Los Alamos National Laboratory [72]. The data collected from these instruments were stored in a database constructed using Structured Query Language (SQL) [73]. Because of the large number of sensors on ADMX, constantly logging the readings from each sensor at a high rate would have rapidly filled available memory of the DAQ computer. To preserve computer memory, each sensor in the experiment was assigned a "deadband". The deadband specified a range about the last logged sensor reading. As the sensors were rescanned, sensor values outside the deadband were logged into the database. Sensor readings were also logged once every 10 minutes even if values remained within the deadband. This scheme for logging data was useful for preserving memory in the data-taking computer, while still allowing us to record values when the state of the experiment was rapidly changing.

3.7 "Sidecar"

Mounted above the main ADMX cavity was a smaller, high frequency cavity called ADMX "Sidecar". ADMX Sidecar served as a testbed for higher frequency axion dark matter searches and was also a bona fide search for high mass axions with stronger-than DFSZ coupling. The Sidecar cavity was tuned using one tuning rod coupled to a piezo-electric stepper motor and mounted directly to the top of the cavity. Use of this piezo-electric motor enabled more precise movement of the tuning rods and eliminated room-temperature mechanical penetrations. For future multi-cavity-type axion searches that require multiple cavities tuned to the same frequency, this piezo technology will be critical. While the initial results from sidecar are not discussed in this thesis, they have been published [74].

3.7.1 Higher-Frequency Resonator Design

The TM_{010} frequencies that can be scanned for a given resonator design are set by the diameter of the resonator. For frequencies up to 2 GHz, ADMX will use the same cavity, but with larger tuning rods to search for higher-frequency axions using the TM_{010} mode. However, the larger tuning rod decreases the volume of the cavity, decreasing the sensitivity to axions. Re-

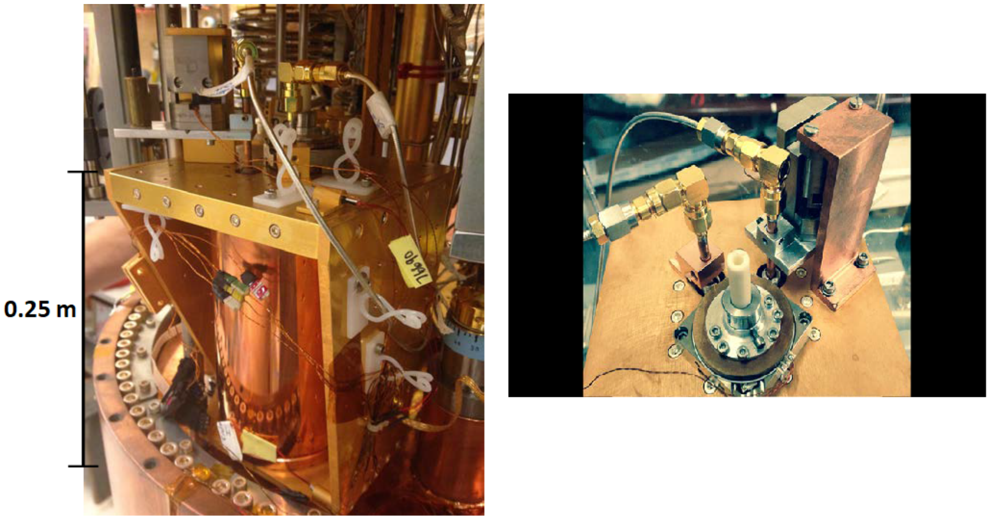

Figure 3.17: ADMX Sidecar is a smaller cavity mounted directly above the main cavity. Sidecar serves as a development test bed and searches for high-mass axions with stronger than DFSZ coupling. The use of piezo-electric motors for tuning will be critical in future ADMX configurations that rely on multiple cavities tuned to the same resonant frequency. Left: Photo of the sidecar cavity mounted to the top of the main cavity. Right: Photo of the piezoelectric motors for tuning sidecar mounted to the top of the sidecar cavity.

call equation 3.1 which determines the scan rate for an axion haloscope. The scan rate scales as $df/dt \ \alpha \ f^2$, naively suggesting an improved scan rate for higher-frequency axion searches. However, that neglects the decrease in the volume of the resonator at higher-frequencies. Assuming a right-circular cylindrical cavity, the volume of the resonator decreases as $V \alpha \ 1/f^4$, so the scan rate is diminished for higher-frequency axion is searches. For frequencies greater than 2 GHz, the decrease in cavity volume is significant enough that ADMX would no longer be sensitive to DFSZ axions in a reasonable time.

There are a number of approaches to solving this problem. One approach would be to search for axions with higher-order TM_{0n0} modes, while maintaining a large cavity volume. However, higher order modes introduce components of the electric field that are anti-aligned with the external magnetic field, significantly decreasing the form factor. The placement of dielectrics at positions where the electric field is anti-aligned within the resonator would reduce the total decrease in form factor. Such an approach is being studied with the Orpheus experiment at the University of Washington [75] and the MADMAX experiment at the Deutsches Elektronen-Synchrotron (DESY) [76].

Arguably, a more direct approach is to increase the number of resonators, each with a smaller diameter. By tuning several smaller resonators to the same frequency and combining the power from the resonators coherently, one can search for axion signals at higher frequencies while maintaining a large effective volume at good SNR. ADMX has prototyped and is currently testing a four-cavity array for the 2-4 GHz frequency range, shown in figure 3.18. This version of ADMX is scheduled to search for axions in 2023. Co-tuning the four resonators to the same frequency requires precise tuning, which can be achieved with a piezo-electric motor. As such, the work done by ADMX Sidecar has provided valuable insight into the development of the four-cavity array.

Figure 3.18: A sketch of the ADMX 4 cavity array which will be used to conduct higher-mass axion searches. This will be operational in 2023.

Chapter 4

DATA TAKING

Data taking for run 1B of ADMX began in January 2018 and ended in October 2018. During that time, ADMX searched for axions between the frequency of 680-800 MHz (masses of 3.36-3.81 μeV), a frequency range of 120 MHz. The goal of data taking in ADMX was to search for potential DFSZ axion signals developed in the cavity. To do this, the cavity was tuned in multiple discrete steps covering the entire frequency range. At each tuning step, some power from the cavity was extracted and sampled. In this section, I will provide an overview of the "run plan" and how the numerous systems in ADMX are integrated into the data-taking procedure. I will also detail the procedure for blind synthetic axion injections into the experiment and calibrating the experiment noise temperature. The analysis of these data is discussed in chapter 5.

4.1 Making a Run Plan

Before the ADMX insert was placed inside the magnet and cooled, a "run plan" had to first be developed. The run plan defined the timeline for the axion search, the frequency range to be covered, the target sensitivity of the axion search, the rod positions throughout the search, and the protocols for rescanning axion candidates and injecting sythetic axion signals. The run plan was informed by the science goals and the constraints of the experiment.

The constraints on the frequency range of the run came from the bandwidth of the various components inside the ADMX insert, such as the tunable range of the cavity and the operable range of the various RF components. In the case of run 1B of ADMX, the primary constraints on frequency were the circulators, which were only operated well between 600-800 MHz. Above 790 MHz, attenuation through the circulator significantly degraded the sensitivity to axions. The lower-frequency range of the run was constrained by science motivations. Previous versions of ADMX had already searched for axions, with high sensitivity, at frequencies up to 680 MHz [57]. Thus, the scan range for run 1B of ADMX was determined to be 680-800 MHz.

For the majority of run 1B, both tuning rods were moved in a clockwise configuration inwards starting from the walls of the cavity. This tuning configuration, known as the "symmetric" configuration, optimized the form factor of the TM_{010} mode by concentrating the electric field near the center of the cavity, away from the fall-off of the magnetic field at the walls.

4.2 Data Taking Cadence

Over the course of a run, the ADMX cavity was tuned in multiple discrete steps across the run's frequency range. After each step, the rods were static and some power from the cavity was extracted to search for axion signals. A number of secondary measurements were also required to further determine operating parameters of the experiment, such as establishing the cavity resonant frequency and the system noise temperature. All these measurements were integrated into a series of steps which define the data-taking "cadence". Listed explicitly, the data taking cadence had to accomplish the following

1. Tune and track the resonant TM_{010} mode of the cavity;

2. Measure and optimize the system noise temperature of the experiment;

3. Sample power from the cavity in search of an axion-like signal.

In practice, the cadence was determined by a main ADMX "data-taking script" software, which controlled the timing and execution of various system state measurements and operations. Figure 4.1 provides a visualization of the data-taking loop. Firstly, swept transmission measurements through the cavity enabled determinations of the resonant frequency and quality factor (Q) of the cavity. Then, some power from the cavity was sampled and digitized as a time series for 100 seconds. The resonant frequency of the cavity was then tuned by actuating the stepper motors connected to the tuning rods so as to rotate the tuning rods inside the cavity. The sequence of operations was then repeated. Periodically during the data-taking loop, additional operations were added. These additional operations included swept reflection measurements to determine the coupling of the antenna to the cavity, and operations to optimize of the system noise temperature of the experiment.

The main ADMX data-taking script was written in a compiled programming language called Lua [77]. During the run, the ADMX data-taking script was controlled and monitored using "DAQ" variables. "DAQ" variables were stored in a Structured Query Language(SQL) [73] table that could be read and updated by the various ADMX data-taking scripts. Among other roles, DAQ variables controlled how often different measurements in the data-taking loop are repeated. DAQ variables were also used to temporarily record run parameters such as the resonant frequency of the cavity and the optimal bias settings for the JPA. These parameters were then used in other steps in data-taking loop. For instance, the cavity resonant frequency recorded in the first step will determine the center frequency for digitization in the fourth step. The data collected were monitored in real time through a web-page interface shown in figure 4.2. Along with the DAQ variables, the web page allowed us to monitor the state of the experiment and make real-time updates to the data taking scripts as needed.

4.3 Tuning the Cavity

Because the mass of the axion is not known *a priori*, the resonator in an axion haloscope must be tunable across a range of frequencies. Recall from section 3.2, ADMX accomplished this tuning using two copper-plated tuning rods aligned parallel to the axis of the cavity and rotated between near the center of the cavity and the cavity walls. The rods were attached to gearboxes mounted to the 1-K plate of the insert. The gearboxes coupled the rotation of the tuning rods to the rotation of the stepper motors with a gear reduction of about 1 to 19,600. To properly tune the cavity, it was critical that we knew the resonant frequency

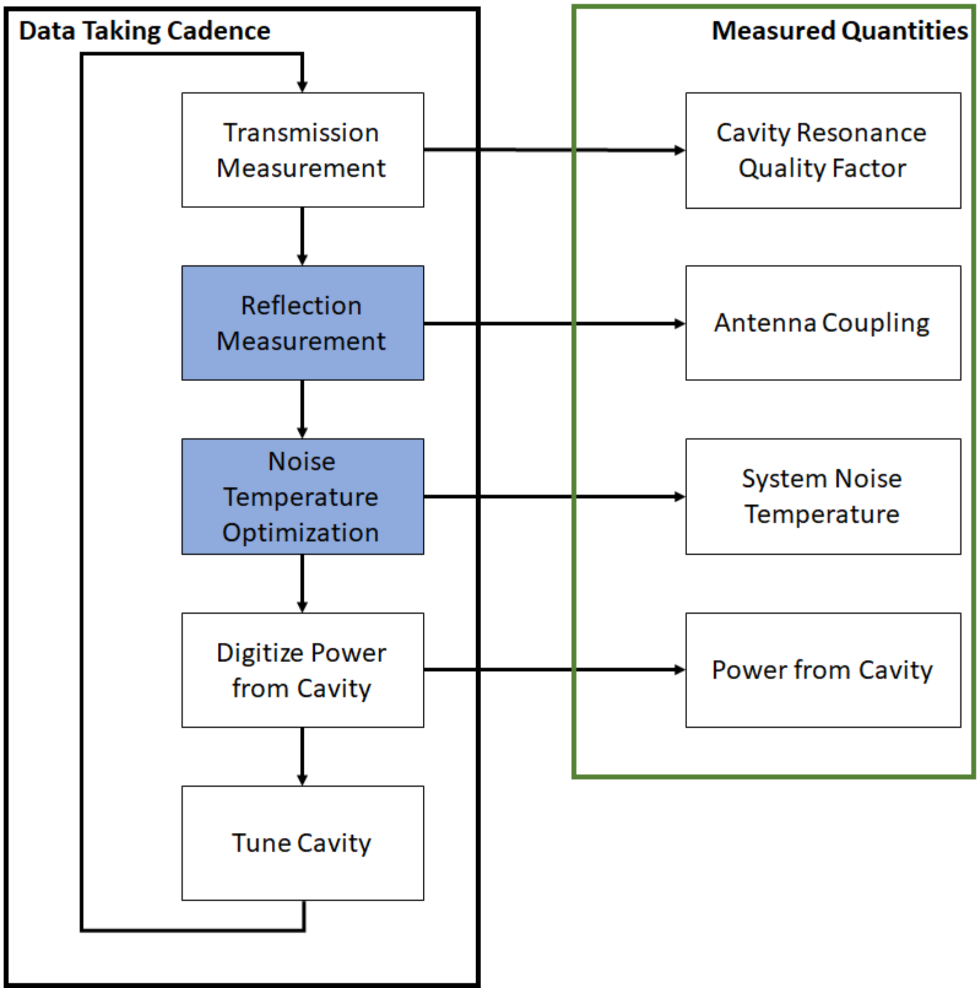

Figure 4.1: A flow chart of the data-taking cadence. The steps in the cadence are listed on the left. Steps highlighted in blue are executed only occasionally. The information collected at each step is shown on the right.

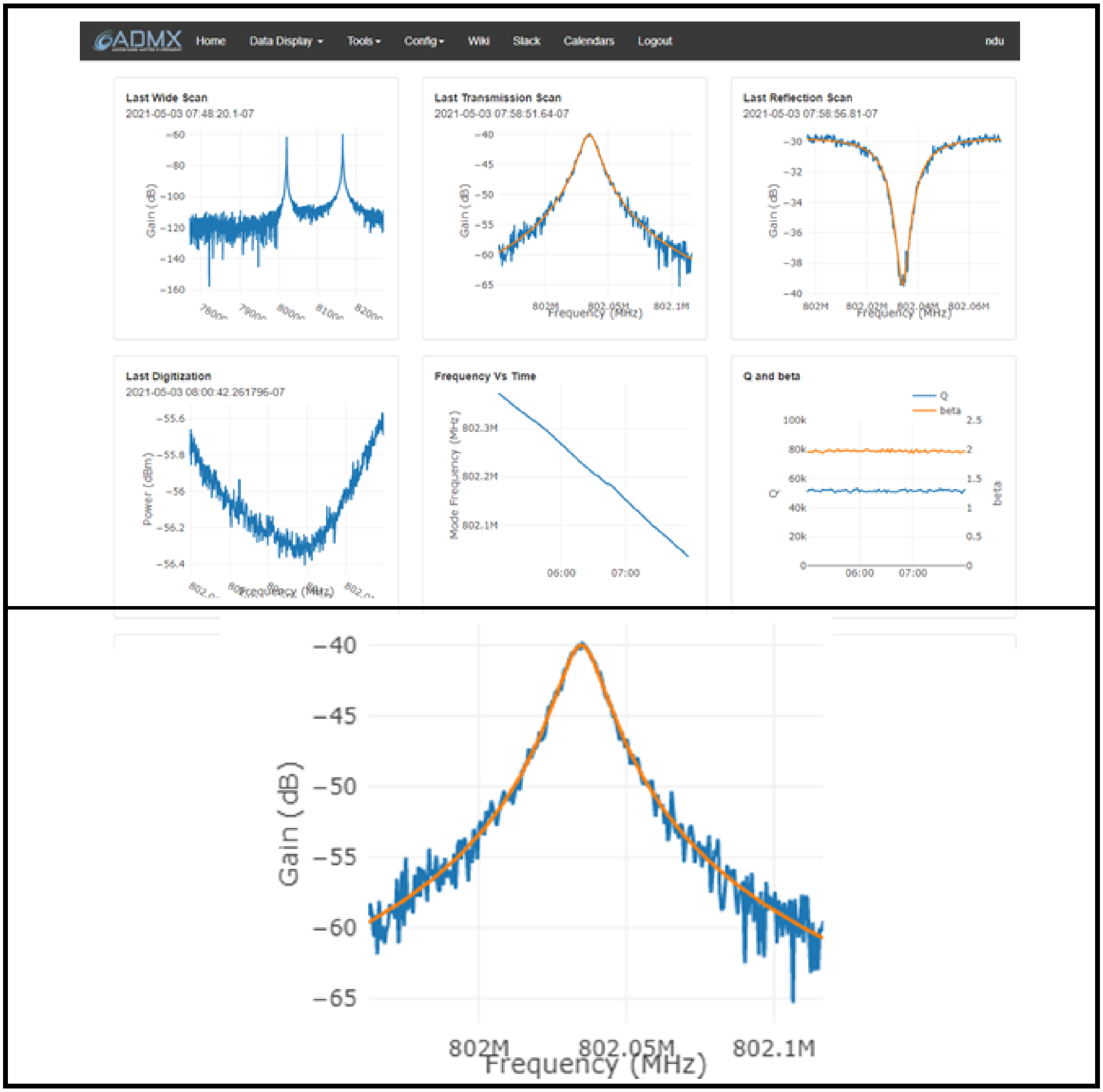

Figure 4.2: Top: A picture of part of the data-taking web page interface. As each step of in the data-taking loop is completed, the plot corresponding to that step is updated. Bottom: An enlargement from the top figure of the transmission measurement. The horizontal axis is frequency and the vertical axis is the relative power transmitted through the cavity in dB. This particular measurement is used to determine the cavity resonant frequency and quality factor.

of the various cavity modes. This informed the frequency at which the digitizer should be set to search for axion signals. In this section, I will provide an overview of how the cavity was tuned and the resonant mode was tracked. I will discuss how a mode of a cavity can be observed and tracked through transmission measurements. I will conclude by discussing the the procedure taking data near mode crossings.

4.3.1 Tracking the Cavity Mode

As the cavity was tuned through the frequency range of the run, it was critical that we accurately track the TM_{010} resonant mode of the cavity. The frequency of the TM_{010} resonant mode informed where the center frequency of the digitized power spectra should be set, by appropriate commands to local oscillators. In rare cases where the mode was "lost" or the wrong mode was tracked, the expected axion power in the corresponding power spectra diminished significantly or even vanished. In order to reliably track the mode of the cavity, transmission measurements were made following every tuning step.

A transmission measurement used a network analyzer to inject a known amplitude swept signal into the ADMX cavity through the weak port while simultaneously measuring the proportion of the signal transmitted through the cavity and receiver chain. The measurement of the relative power transmitted through the cavity and receiver chain as a function of frequency was known as the transfer function of the cavity. During data-taking, transmission measurements were performed immediately following every tuning step in a relatively narrow frequency range of about 200 kHz about the previous resonant frequency of the cavity. Figure 4.3 shows a plot of a number of swept transmission measurements taken for several tuning steps. Note that the tuning steps were small compared to the frequency range of a swept transmission measurement, ensuring the mode could be accurately tracked.

The transfer functions of the cavity transmission response were fit to the usual resonant Lorentzian of form

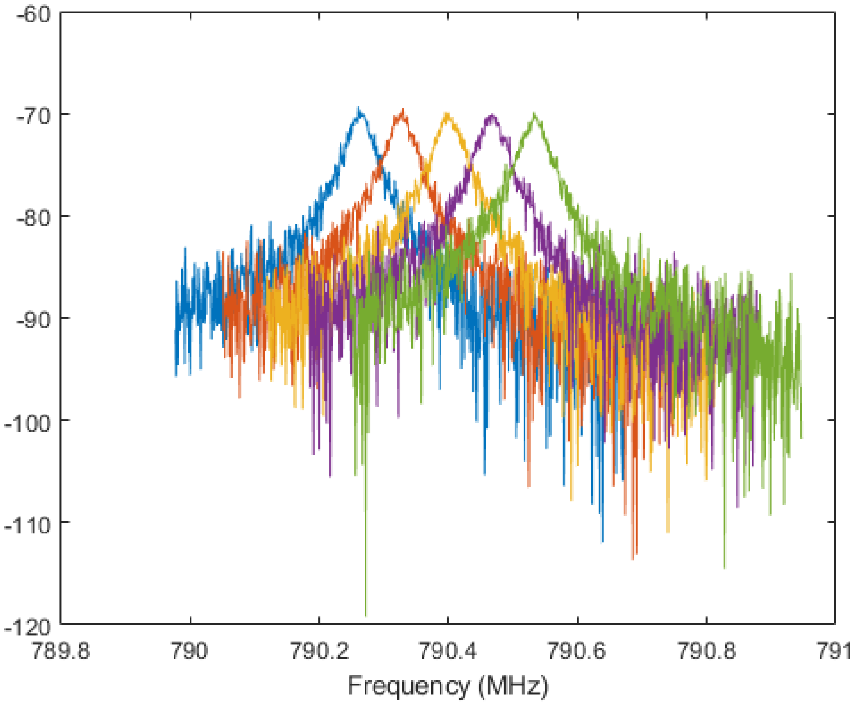

Figure 4.3: A plot showing a series of overlapping swept transmission measurements at sequential tuning steps. The vertical axis is the relative power transmitted through the cavity in dB.

$$L(x) = A + \frac{B}{1 + 4Q_L^2(\frac{f-f_0}{f_0})^2}, \tag{4.1}$$

where f_0 is the resonant frequency of the cavity, Q_L is the loaded quality factor of the cavity, and A and B are additional free parameters of the fit describing the relatively flat noise floor and Lorentzian amplitude. In fact, the resonance lineshape was slightly non-Lorentzian due to parasitic reactances but that is ignored here. The results of the fit were used to determine the resonant frequency and loaded quality factor of the cavity in the DAQ system. Figure 4.4 shows a typical transmission response through the cavity with along with its associated fit. This procedure was found to work well in tracking the cavity resonant mode throughout the run.

4.3.2 Making a "Mode Map"

In addition to the transmission measurements performed after every tuning step, transmission measurements over a wider frequency range, greater than 10 MHz, were made periodically in order to understand the cavity mode structure. Figure 4.5 (Top) shows a typical a transmission measurement through the cavity across a wide frequency band. Peaks seen in the resulting transfer function corresponded to the different modes inside the cavity.

Combined, these wide transmission measurements were used to make a "mode map" of the cavity, shown in figure 4.5 (Bottom). The mode map visualized how the various modes of the cavity change in frequency as the tuning rods rotate within the cavity. Because there were two tuning rods, the mode map was typically made with the horizontal axis specifying the position of one tuning rod while the position of the other tuning rod was fixed. Mode crossings could be observed as regions where two modes of the cavity "intersect" one another. As stated before, at mode crossings, the sensitivity of the experiment diminished significantly and additional procedures were introduced to search for axions near mode crossings.

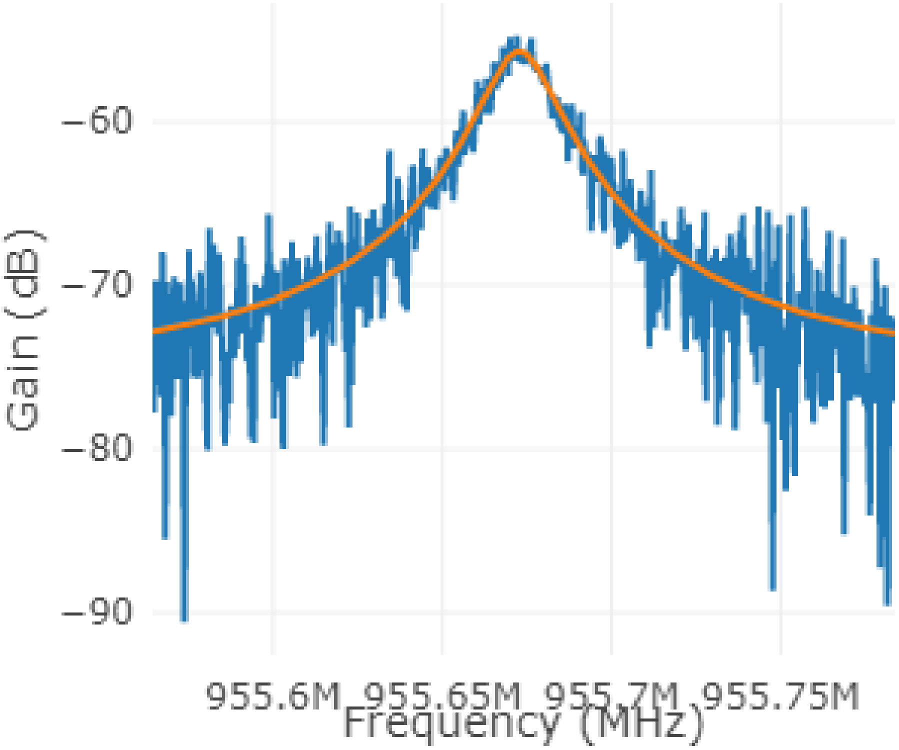

Figure 4.4: An example transmission response through the cavity along with its associated fit. The proportion of power transmitted through the cavity is measured in dB over a range of frequencies. The orange line represents the fit to the response, which establishes the cavity quality factor and resonant frequency.

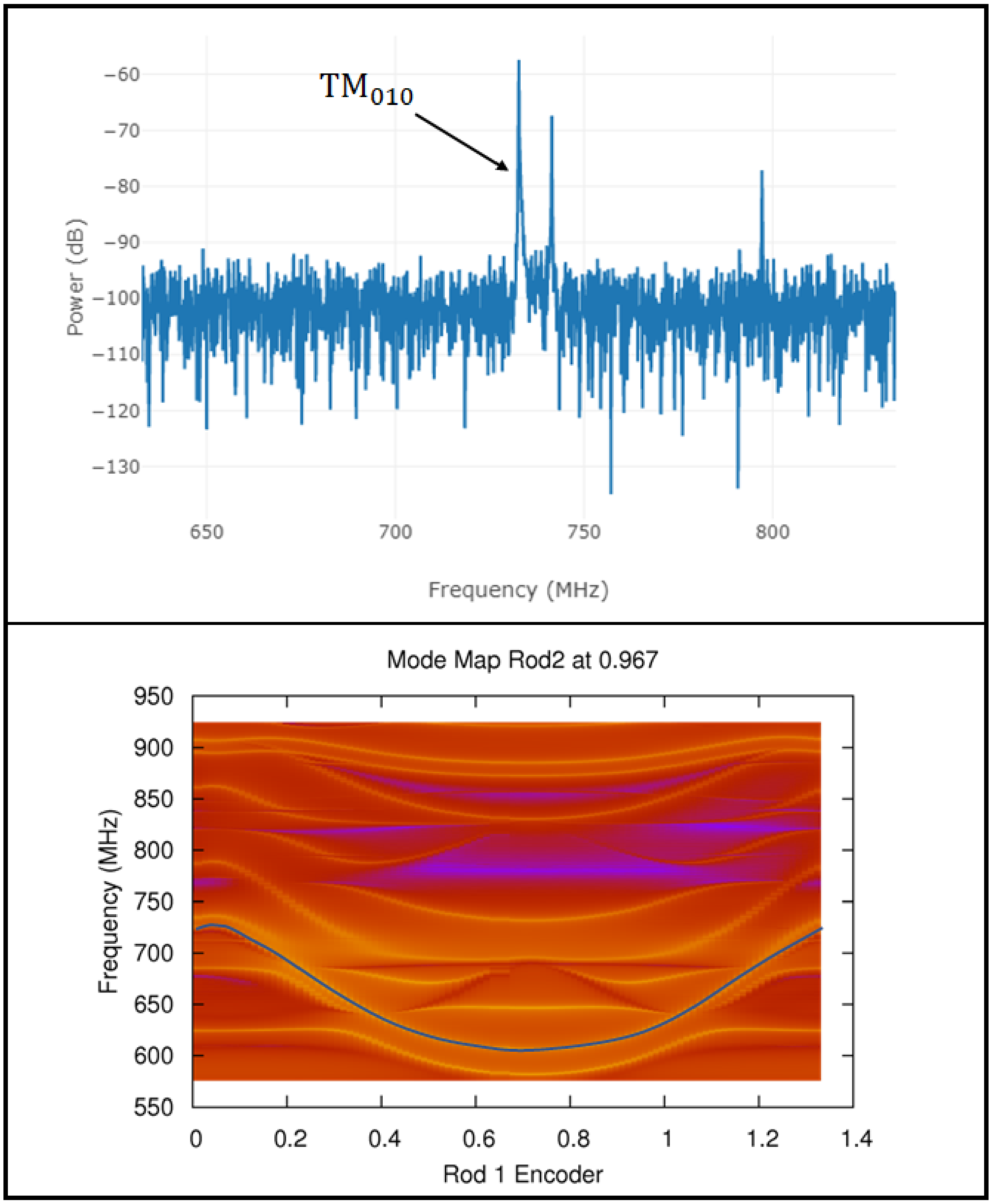

Figure 4.5: Top: A plot of a typical wideband transmission measurement through the cavity. The relative power transmitted through the cavity is shown on the vertical axis in dB, and frequency in MHz is shown on the horizontal axis. The TM_{010} mode is indicated by the arrow. Bottom: A mode map made by making repeated wideband transmission measurements as the cavity is tuned. Here, the position of one of the rods is plotted on the horizontal axis, the other rod is fixed and the vertical axis is the frequency of the various cavity modes. The TM_{010} is tracked in blue.

4.3.3 Mode Crossings

To take data near these mode crossings, an alternative rod configuration was used in which one rod was moved in a clockwise direction and another was moved in a counter-clockwise direction, referred to as the anti-symmetric configuration. In this configuration, the weakly-tuning modes were shifted by several MHz relative to the TM_{010} mode, thereby shifting the position of the mode crossing. Electric field strengths for both the initial data-taking rod configuration (symmetric) and the rod configuration for scanning mode crossings (anti-symmetric) are shown in figure 4.6. Mode crossings were scanned near the end of the run to minimize the number of times the rod configuration was switched. This alternative rod configuration decreased the overall form factor due to the mode being concentrated more toward the edge of the cavity where the magnetic field is weaker. However, the form factor was still adequate to search for axions at DFSZ sensitivity.

Table 4.1 lists the mode crossings for the run and their corresponding frequency width. The frequency width of the mode crossing was defined as the width over which power transmitted through the cavity is at least half the power transmitted through the cavity on resonance. The mode crossings at 728.30, 744.90, and 782.20 MHz were successfully scanned with an anti-symmetric rod configuration. At other mode crossings, the mode crossings were either too wide for the configuration to shift the mode enough or the sensitivity to axions at that mode crossing was inadequate. Therefore, there were several narrow frequency gaps in the analysis where we were unable to search for axions.

4.4 Coupling the Receiver to the Cavity

The strongly-coupled antenna inserted into the top of the cavity extracted some power which was then amplified by the receiver and sampled by the digitizer. It was important that the antenna be properly coupled to the cavity, as a poorly-coupled antenna would extract only a small amount of power from the cavity and too much coupling would degrade the quality factor. In either case the SNR of an axion signal would be degraded. The antenna coupling

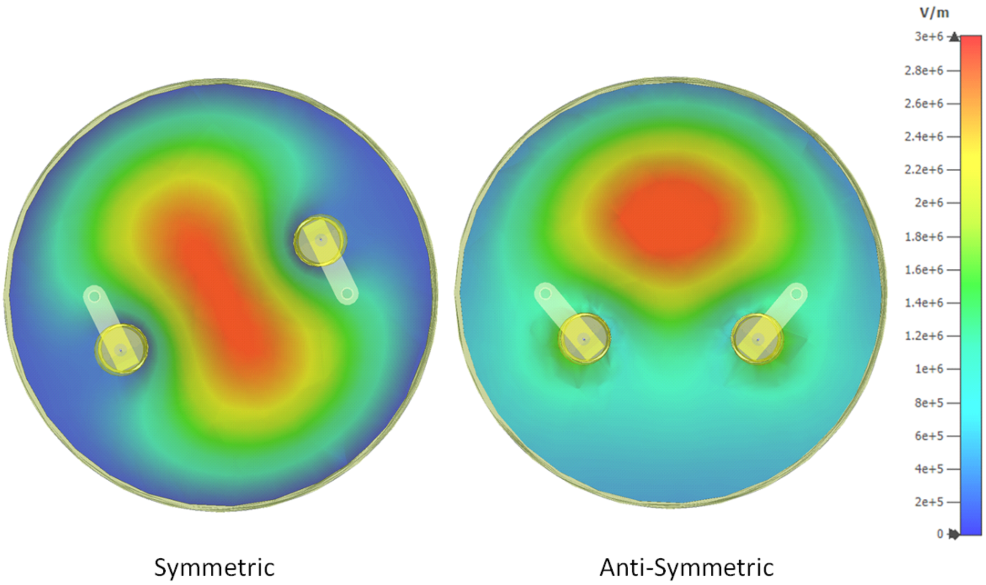

Figure 4.6: The magnitude of the axial electric-field in a cross-section through the center of the cavity. The TM_{010} resonant frequency of the cavity is set by the position of two tuning rods. During initial data-taking, the rods are moved in a symmetric configuration (left). To scan over mode crossings, an anti-symmetric configuration is used (right). The frequency of the TM_{010} mode is the same in both configurations shown. The colors indicate the magnitude of the electric field along the axis of the cavity.

Mode-Crossing Frequency (MHz)	Width (MHz)
704.659	0.350
726.624	0.701
728.301	0.610
744.907	1.200
753.844	12.682
782.20	0.800

Table 4.1: Mode-crossing frequencies encountered in the range scanned in run 1B.

was adjusted by withdrawing or inserting the antenna into the cavity.

Reflection measurements off the cavity were used to determine the coupling. In this reflection measurement, a swept RF signal was applied to the antenna via the cavity bypass line and the fraction of power reflected off the antenna was measured through the output line by use of a network analyzer. Figure 4.7 shows the reflected power from one such reflection measurement.

By comparing the fraction of power reflected on- and off-resonance, the coupling of the antenna was determined. Near the cavity resonance, a portion of the applied power entered the cavity, and the remainder was reflected. The absorption of power near the cavity resonance led to the dip in the center of the reflection. On the other hand, far from the cavity resonance, a large impedance mismatch between the cavity and antenna transmission line resulted in almost all of the power being reflected off the cavity. This is clear in the reflection measurement.

Recall that when the antenna was critically coupled to the antenna, the impedances of the cavity and antenna were matched. At critical coupling less than 1/1000th of the power incident on the antenna on-resonance was reflected, corresponding to a 30 dB difference between the on- and off-resonance reflection. During data-taking, when the difference between the on- and off-resonance reflection fell below 5 dB, the insertion depth of the antenna would be adjusted to re-couple the antenna to the cavity mode.

4.5 Sampling Power from the Cavity

Power in the cavity that had been extracted by the antenna was then amplified and processed by the microwave receiver. The amplified signal from the cavity was mixed down to a 10.7 MHz intermediate frequency at a mixing stage in the room-temperature receiver. The signal was then passed through a narrow bandpass filter to remove the tones of the local oscillator introduced by mixing. The signal at the output of the receiver was sampled as a voltage time series by a “digitizer”. The digitizer used by ADMX is discussed in section 3.4.5. In searching for axion signals from the cavity, the signal from the cavity was integrated and

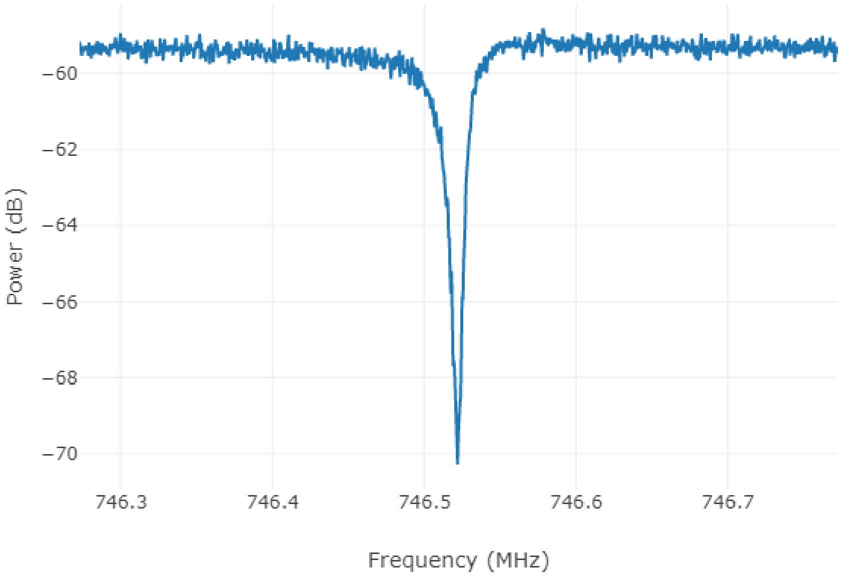

Figure 4.7: A typical reflection measurement. The horizontal axes is the frequency and the vertical axis is the fraction of power reflected off the cavity in dB. The location of the dip corresponds to the resonant mode of the cavity. Off resonance, power is reflected off the cavity. On resonance, most of the power is enters the cavity. The relative power reflected off- and on-resonance allows us to infer the antenna coupling.

sampled for 100 seconds. The resulting voltage time series was then Fourier-transformed into a single-sided voltage amplitude spectrum, and the magnitude of the voltage spectrum was computed in order to obtain the power spectrum from the cavity. Each such power spectrum was 50 kHz wide about the resonant frequency of the cavity, with 100 Hz wide bins.

4.6 Blind Synthetic Axion Injections

Run 1B of ADMX implemented a system for blindly injecting synthetic axions into the ADMX experiment. These injections used the synthetic axion generator system discussed in section 3.5 to apply synthetically-generated axion-like signals into the cavity through the weakly-coupled antenna. Before the run, a list of synthetic axion frequencies was generated by a member of the ADMX collaboration deemed the “blindness czar”. The frequencies of the synthetic axions were stored in a SQL table and were blinded to the axion-search analysis group. During data-taking operations, the resonant frequency of the cavity was automatically checked against the list of synthetic axion frequencies before the digitization step. If a synthetic axion frequency was within 25 kHz of the cavity resonant frequency (within the bandwidth of the digitized power spectrum), the synthetic axion generator would configure itself to inject a synthetic axion into the system. For all intents and purposes, power spectra containing synthetic-axion signals were processed as normal data.

4.7 Noise Temperature Calibration

One of the key parameters for establishing the sensitivity of the experiment is the system noise temperature. As discussed previously, the system noise temperature was almost wholly equal to the sum of the physical temperature of the cavity and the noise contribution from the components of the microwave receiver, such as the amplifiers and circulators. Understanding the system noise temperature of the experiment was critical to determining the sensitivity of the experiment and calibrating the power of signals coming from the cavity.

Noise temperature calibration in ADMX was done in two steps, described in the following two subsections. These two steps calibrated the noise temperature of the receiver with and without the JPA. The two steps were referred to as a “hot load” measurement and “signal-to-noise measurement”.

In the first step, the pump tone to the JPA was turned off so that the input of the JPA acts as a nearly-perfect reflector. We call this “turning the JPA off”. The system noise of the receiver with the JPA turned off was then calibrated using what is known as a “hot load” or “y-factor” measurement [78]. This measurement sampled the power at the output of the digitizer while heating to a known temperature a specific Johnson noise source at the input of the receiver, called the “hot load”.

In principle, the hot load measurement could be directly used to determine the noise temperature of the receiver with the JPA on, however in practice, there are several issues complicating this. The JPA provided gain over a narrow bandwidth, between 10-20 MHz. Because of this, the resonant frequency of the JPA was regularly re-tuned in a biasing procedure, and re-biasing somewhat altered the JPA characteristics. Hence, hot load measurements to calibrate the noise temperature of the receiver after each JPA bias procedure would have been extremely time consuming and dramatically reduced the overall scan rate. In addition, the characteristics of the JPA changed noticeably with even small variations in temperature. A variation of even 10 mK in the temperature of the JPA at a given bias could result in a drop in the gain of the JPA by 20 dB if not re-biased. During a hot-load measurement, conduction heating of the JPA through the RF line connecting to the hot load presented a potential parasitic path for heating the JPA. If the JPA were parasitically heated, the noise calibration would be compromised, as the gain of the JPA and the system noise temperature would have likely varied appreciably. For these reasons, the hot-load measurement technique was not used for calibrating the system noise temperature with the JPA on. Instead, a second measurement, known as a “signal-to-noise improvement measurement”, in tandem with a “hot-load” measurement was used to calibrate the system noise temperature of the experiment with the JPA turned on.

In a signal-to-noise improvement measurement, the gain and power of the receiver were measured separately with the JPA turned off and on. The relative change in gain and power of

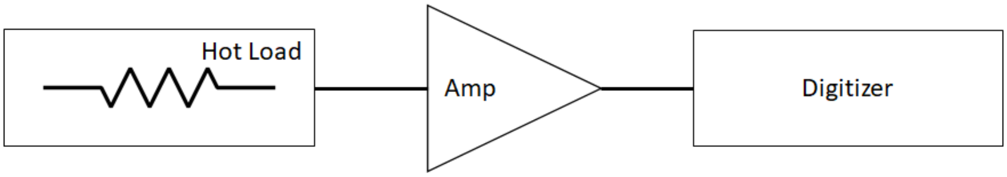

Figure 4.8: A simple model for a hot load measurement

the receiver were then used to calculate the relative improvement in the signal-to-noise ratio of the receiver when the JPA is turned on. Combined with the previous noise temperature measurement with the JPA turned off (determined from the hot load measurement), the noise temperature of the system with the JPA turned on therefore be found.

4.7.1 Hot Load Measurement

A hot load, or y-factor, measurement was used to calibrate the noise temperature of receiver when the JPA is turned off. These measurements involved the heating of a Johnson noise source, called the "hot load", to a known temperature [78]. The hot load was connected to the input of JPA and the temperature of the hot load and power output from the receiver during heating were recorded. Figure 4.8 is a simplified block diagram a hot load measurement. In this example, the power at the output of the amplifier is

$$P_{out} = k_B B G_{amp}(T_{hot\ load} + T_{amp}) \tag{4.2}$$

where k_B is Boltzmann's constant, B is the bandwidth of each bin of the power spectrum, G_{amp} is the power gain of the amplifier, $T_{hot\ load}$ is the temperature of the hot load, and T_{amp} is the noise temperature contribution of the amplifier. By measuring $T_{hot\ load}$ and the output power, a linear fit in principle establishes the gain and noise contribution of the amplifier.

In practice, this procedure was complicated somewhat if there was attenuation at a different temperature than the hot load between the hot load and amplifier. The additional attenuation attenuated the power from the hot load and also contributed additional noise corresponding to the temperature of the attenuator. This was the case with the ADMX experiment, where RF components such as the circulator added attenuation between the hot load and JPA. In order to measure the gain and noise temperature of the receiver with the JPA off and the attenuation within the Squidadel, two separate hot load measurements were used, where an RF switch was used to switch the input of the JPA between either the cavity or the hot load and then the Squidadel or hot load are heated, respectively. The noise sources used in both measurements are shown in the receiver diagram shown in figure 4.9.

In the first method, a switch in the Squidadel was actuated so that the input of the HFET amplifier was directed toward the hot load, boxed in red in figure 4.9. The hot load was then slowly heated over the range 4-10 K. During this, the temperature of the hot load was monitored with a temperature sensor mounted to the hot load and the power output from the receiver was constantly sampled by the digitizer. In this configuration, noise from the hot load was amplified by the HFET amplifier and warm receiver and the expected output power was

$$P_{out} = k_B B G_{HFET}(T_{hot\ load}\epsilon + T_{JPA}(1-\epsilon) + T_{HFET}) \tag{4.3}$$

where $T_{hot\ load}$ is the temperature of the hot load, T_{JPA} is the temperature of the JPA, ϵ is the attenuation between the cavity and HFET amplifier, T_{HFET} is the noise temperature of the HFET amplifier and warm receiver, and G_{HFET} is the power gain of the HFET amplifier and warm-receiver components.

In the second method, the switch in Squidadel connected the input of the HFET amplifier to the cavity. In this receiver configuration, attenuator A, boxed in blue in figure 4.9, was used as the noise source. The noise power from attenuator A was reflected off of the cavity (at frequencies off resonance of the cavity) and amplified by HFET amplifier. Attenuator A was heated between 0.23-1.0 K by sending a low current through switch S, which was thermally connected to attenuator A. The current was low enough that the switch was not actuated, but large enough to heat attenuator A. The expected output power was

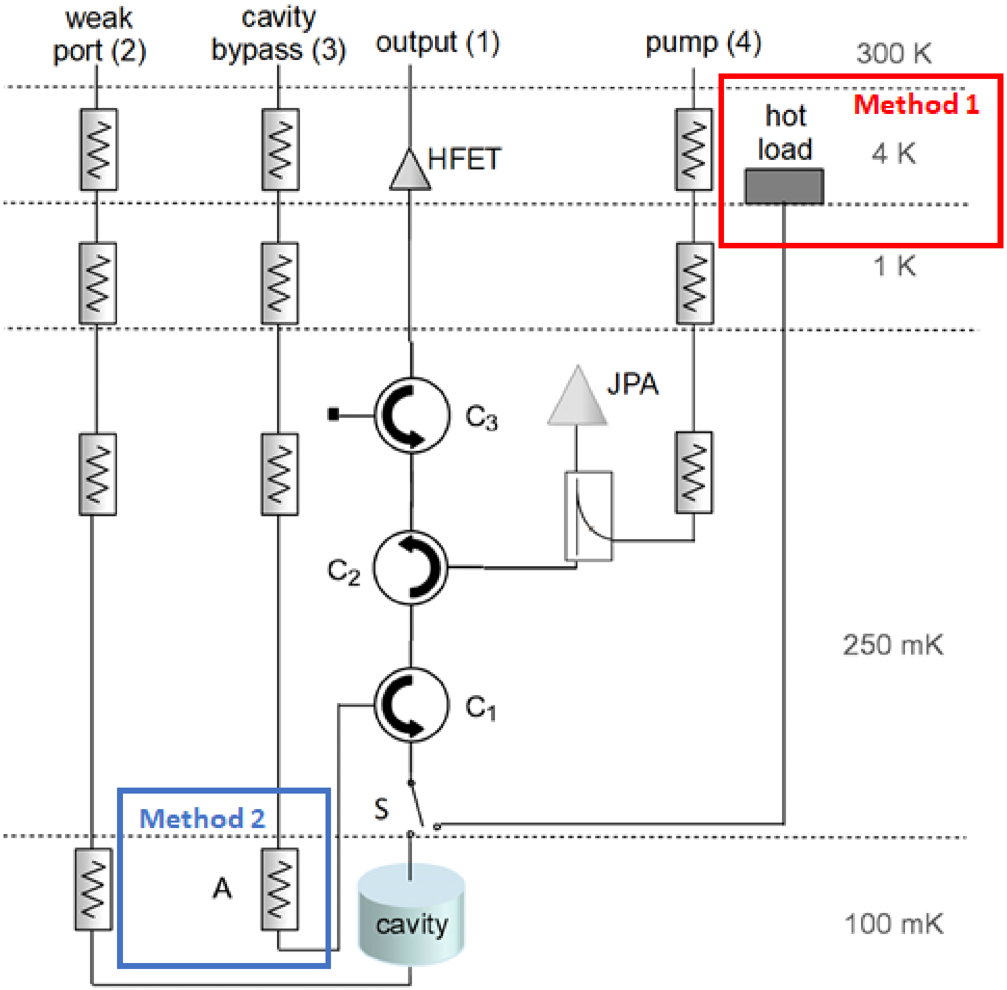

Figure 4.9: A schematic of the receiver of ADMX, from section 3.4. Hot load measurements are done with two methods. In method 1 (red), the receiver is connected to the hot load and the hot load is heated. In method 2 (blue), the switch is connected to the cavity and attenuator A (bottom left) is heated.

$$P_{out} = k_B B G_{HFET}(T_A \epsilon + T_{JPA}(1-\epsilon) + T_{HFET}) \tag{4.4}$$

where T_A is the temperature of attenuator A. Because the temperature of the JPA and attenuator A were approximately equal relative to the temperature of the HFET, T_A and T_{JPA} were nearly equal. In this case, the output power was

$$P_{out} = k_B b G_{HFET}(T_{JPA} + T_{HFET}). \tag{4.5}$$

the second method allows for a measurement of T_{HFET} independent of the amount of attenuation between the JPA and cavity.

This second method allows for a measurement of T_{HFET} that is independent of the attenuation between the JPA and cavity, and the first method can be used to determine the attenuation between the cavity and the JPA. Over the frequency range of interest, the noise temperature of the HFET amplifier plus downstream receiver components was determined to be 11.3 ± 0.1 K where the uncertainties listed here are the statistical errors in the fit. Both the measured gain and HFET noise temperature were incorporated into the analysis when establishing the sensitivity of the experiment.

4.7.2 Signal-to-Noise Improvement Measurement

A signal-to-noise improvement (SNRI) measurement is a commonly-used method to characterize the behavior of amplifiers. The signal-to-noise improvement ratio is defined as

$$SNRI = \frac{G_{on}}{G_{off}} \frac{P_{off}}{P_{on}} \tag{4.6}$$

where G_{on} and G_{off} are the power gain of the receiver with the JPA on and off and P_{on} and P_{off} are the noise power at the output of the receiver with the JPA on and off. As mentioned previously, when the JPA was turned off, that is, when it was no longer supplied with a pump tone, it behaved as a nearly perfect reflector for signals at the input.

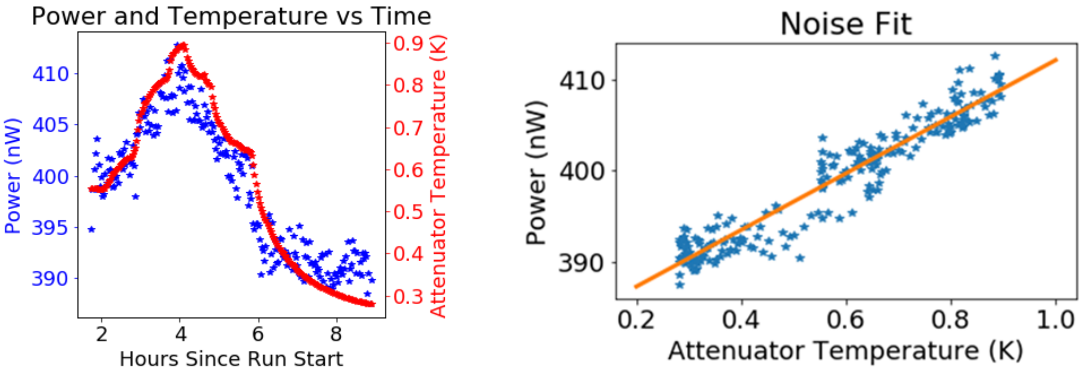

Figure 4.10: A typical hot-load measurement heating the Squidadel. Left: A plot of the power as recorded by the digitizer and attenuator temperature as a function of time during the hot load measurement. Right: A typical y-factor measurement showing the measured power as a function of the temperature of the Squidadel. A linear fit established the noise temperature of the system.

Assuming for now that the noise from the receiver was predominantly Johnson noise, P_{on} and P_{off} can be rewritten in terms of a noise temperature as

$$P_{on} = kBT_{sys} \tag{4.7}$$

$$P_{off} = kBT_{HFET} \tag{4.8}$$

where T_{sys} is the noise temperature of the system with the JPA on and T_{HFET} is the noise temperature of the HFET amplifier and warm receiver electronics (JPA off), as established from the hot-load measurement. Combined with equation 4.6, the system noise temperature is then

$$T_{sys} = \frac{T_{HFET}}{SNRI}. \tag{4.9}$$

SNRI measurements were made frequently throughout the run between tuning steps of the cavity. The increase in the receiver gain G_{on}/G_{off} with the JPA on was measured by comparing the fraction of power reflected off-resonance in reflection measurements. The change in noise power, P_{off}/P_{on} was measured by sampling power from the receiver with the JPA both on and off.

The SNRI measurement technique was especially useful in that it provided a method for determining the system noise temperature of the experiment without actively heating any elements in the experiment. This allowed SNRI measurements to be repeated often without having to wait between measurements for the experiment to thermally re-equilibrate. In fact, ADMX took advantage of the ability to perform rapid back-to-back SNRI measurements to optimize the system noise temperature of the experiment.

4.7.3 Optimizing the Noise Temperature

As the resonant frequency of the cavity was tuned across the frequency range, the JPA was repeatedly re-biased to keep the system noise temperature at a minimum. This re-biasing consisted of varying the JPA pump tone's power and frequency and the bias current to the JPA.

To ensure that the noise temperature of the receiver with the JPA on is minimized, the JPA SNRI was first coarsely scanned across several combinations of pump tone powers and bias currents. Figure 4.11 shows one such scan of the JPA SNRI at a given frequency, with the optimal settings corresponding to the highest JPA SNRI. This process was repeated every 5-7 tuning steps, corresponding to about once every 10 minutes. Between JPA re-biasing operations, it was observed that the SNRI did not vary by more than 1 dB, so the noise temperature did not vary significantly between single tuning steps.

4.8 Candidate Rescan Procedure

At a high-level overview, the run 1B frequency range of the run is divided into several segments, called "nibbles", typically about 10 MHz wide. The division of the run into nibbles minimized the number of times the cavity had to be tuned through a mode crossing and minimized any changes in operating conditions for axion-search data taken at a given frequency.

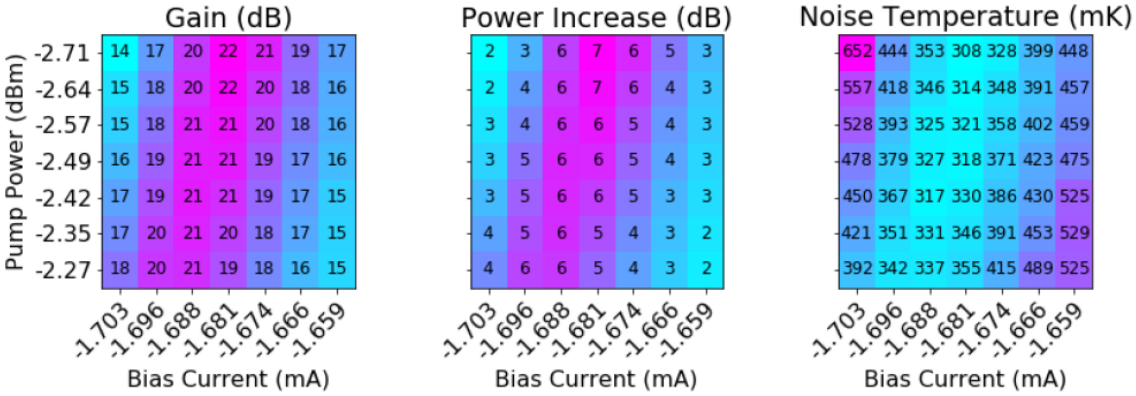

Gain (dB)

	-1.703	-1.696	-1.688	-1.681	-1.674	-1.666	-1.659
-2.71	14	17	20	22	21	19	17
-2.64	15	18	20	22	20	18	16
-2.57	15	18	21	21	20	18	16
-2.49	16	19	21	21	19	17	16
-2.42	17	19	21	21	19	17	15
-2.35	17	20	21	20	18	17	15
-2.27	18	20	21	19	18	16	15

Power Increase (dB)

	-1.703	-1.696	-1.688	-1.681	-1.674	-1.666	-1.659
	2	3	6	7	6	5	3
	2	4	6	7	6	4	3
	3	4	6	6	5	4	3
	3	5	6	6	5	4	3
	3	5	6	6	5	3	3
	4	5	6	5	4	3	2
	4	6	6	5	4	3	2

Noise Temperature (mK)

	-1.703	-1.696	-1.688	-1.681	-1.674	-1.666	-1.659
	652	444	353	308	328	399	448
	557	418	346	314	348	391	457
	528	393	325	321	358	402	459
	478	379	327	318	371	423	475
	450	367	317	330	386	430	525
	421	351	331	346	391	453	529
	392	342	337	355	415	489	525

Figure 4.11: An example of an system noise optimizing procedure. From left to right are measurements of the JPA gain and power increase, and receiver noise temperature at several different combinations of JPA bias currents and pump tone powers. Left: The change in the gain of the receiver when the JPA is turned on and off. Middle: The change in noise power from the receiver when the JPA is turned on and off. Right: The calculated system noise temperature of the receiver with the JPA. In this example, the system noise temperature is optimal at 380 mK when the JPA bias current is -2.49 mA and the JPA pump tone power is -1.70 dBm.

After an initial scan through the frequency range of each nibble, potential axion signals are identified as potential “candidate” axions. The method for identifying a “candidate” axion will be discussed in the “Analysis” chapter. A similar data-taking procedure was applied for rescanning candidates, a process where candidates were studied in more detail. However, during the rescan procedure, the scan rate was increased significantly at non-candidate frequencies, and candidate axions were rescanned with a significantly longer integration time to improve the signal-to-noise ratio of a putative axion signal. Axion candidates that persisted after two rescans were then subject to additional studies, which will be discussed in the “Analysis” chapter.

4.8.1 Blinded-Synthetic Axion Injections

Throughout the run, a number of synthetic axions at varying powers were injected into the system using the synthetic axion generator system discussed in section 3.5 and the frequencies of the injections were blinded to the analysis group searching for axion candidates. After they were identified as candidates, synthetic axions would be unblinded either following the first rescan (“class 1”) or before a procedure in which the magnetic field would be ramped down and the power of the candidate signal was re-measured (“class 2”). Using this method for blinded-synthetic axion injections, after all the synthetic axions were unblinded in a given nibble, the synthetic axion generator was turned off and the frequencies of synthetic axions were rescanned in the admittedly small likelihood the synthetic axion signal masked a true axion signal. The blinded-synthetic axion injections enabled exercising of the candidate rescan procedure and ensured that the analysis would always havae some initial axion candidates.

4.9 Run Summary

The target frequency range of run 1B of ADMX was explored between January and October 2018. Across the frequency range the signal-to-noise ratio for a DFSZ axion was more than sufficient to enable us to exclude DFSZ axions in the null case. Over the run, in total about

190,000 individual power spectra were collected. The method by which these spectra were combined and used to search for a potential axion signal is discussed in the next chapter.

Chapter 5

ANALYSIS

The goal of the analysis was to search for an axion signal within data collected from run 1B of ADMX, which scanned the frequency range 680-800 MHz. This chapter will focus on the analysis of the run 1B data. I will begin with an introduction to the analysis. Then, I will describe in more detail the methodology of the analysis. I will conclude by discussing results thereby obtained from run 1B.

5.1 Analysis Introduction

The goal of the analysis was to identify, with high confidence, axion-like signals that may be in one or more of the 190,000 individual spectra collected during run 1B. The analysis methodology was built on that developed by Edward Daw, a former ADMX student [79]. Each individual spectrum represented the microwave power from the cavity amplified by the receiver across a 50 kHz-wide bandwidth and centered on the cavity resonant frequency. Typically, the signal-to-noise ratio (SNR) for an axion signal in an individual spectrum at the resonant frequency of the cavity after 100 seconds of integration was 11.7 (1.7) for KSVZ (DFSZ) axions. In the case of the DFSZ axion, the main target of this search, the SNR of an axion signal was too small to be easily detectable by eye in an individual spectrum. To increase the sensitivity to such axions, the power from individual spectra were "co-added" together to form what was termed a "grand spectrum", with consequently higher SNR. In this chapter, I will review how a grand spectrum is constructed from the individual spectra and how the grand spectrum is used to identify candidate axion signals.

5.1.1 Analysis Overview

The analysis consisted of several steps, shown in figure 5.1. First, the database was queried for power spectra from the frequency range being analyzed. Afterwards, each spectrum was processed in the single-spectrum analysis. This step accounted for variations in experimental conditions between different spectra. Then, the processed spectra were co-added to form a "grand spectrum". The analysis used the grand spectrum to search for candidate axion signals. Any candidates thus found were flagged as a basis for more detailed analysis.

5.1.2 Increasing the SNR by constructing a Grand Spectrum

By co-adding individual spectra to form a grand spectra, the SNR of an axion, which could be small in an individual spectrum, was increased. This is somewhat obvious, but to take a simple example, suppose a single spectrum consists of white noise, σ_{noise}, with a small signal P_{sig} in one frequency bin. The SNR for this single spectrum would be $SNR_{single} = P_{sig}/\sigma_{noise}$. Obviously, when N such spectra are combined by adding together the power from each contributing bin, the total power of the signal is increased to $P_{sig,grand} = NP_{sig}$ while the noise is increased by $\sigma_{noise,grand} = \sqrt{N}\sigma_{noise}$. Thus, the SNR in the grand spectrum would be $SNR_{grand} = P_{sig}/\sigma_{noise} \times \sqrt{N} = SNR_{single} \times \sqrt{N}$. Figure 5.2 shows an example of assembling a grand spectrum from individual spectra containing synthetic KSVZ and DFSZ axion signals. The DFSZ axion signal, which is not easily observable in a single spectrum, is observable in the grand spectrum.

In the ADMX analysis, this process of co-adding spectra was more complicated. Firstly, the frequency bin number in which a putative signal was located in a spectrum varied as the cavity resonant frequency was tuned and the frequency range covered by the digitizer changed. The putative signal power also varied depending on parameters of the experiment, such as the quality factor of the cavity. In addition, each spectrum contained large-scale structure associated with the frequency-dependent gain of the ADMX receiver that distorted the shape of the noise spectrum of the receiver. The single-spectrum analysis, which will be

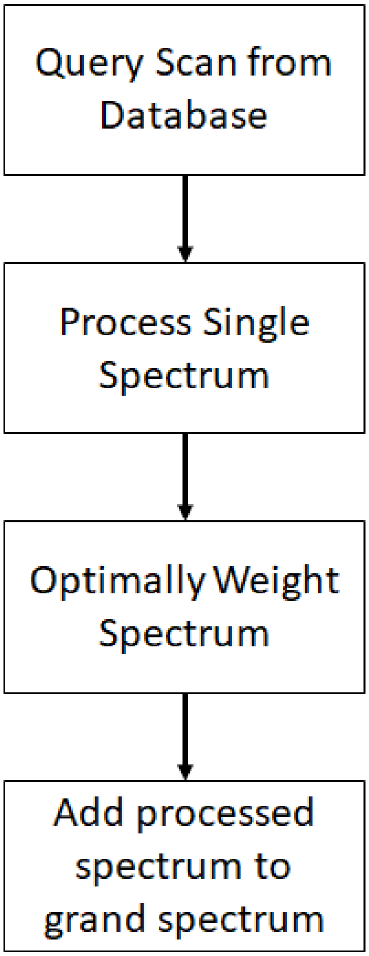

Figure 5.1: A diagram of the distinct steps of the analysis. First, individual spectra are queried from the SQL database. Second, the spectra are processed. The processed spectra are "weighted" and then co-added together to form a grand spectrum.

discussed in the section 5.2, processed the individual spectra to account for these variations.

5.2 Single Spectrum Analysis

Over the course of run 1B, a total of approximately 190,000 raw power spectra from the cavity were collected. Each spectrum was a 50 kHz wide, centered on the resonant frequency of the cavity, and no windowing was applied to the spectrum. Each spectrum consisted of 511 frequency bins with a bin width of 95.7 Hz. While the SNR for a DFSZ axion signal was small in any individual spectrum, about 1.7, by co-adding the spectra together, the SNR could be increased such that an axion signal would have been observable. Before spectra could be co-added together, each raw spectrum had to be "processed". Broadly speaking the steps taken in to process a raw spectrum were

1. Remove the large-scale structure associated from the raw spectrum
2. Re-scale the power measured in each bin to account for variations in the SNR of an axion
3. Filter each spectrum for axion-like signals

These steps were collectively called the "single-spectrum analysis" and will be discussed in this section.

5.2.1 Removing the RF Background

Recall from section 2.6, the power at the output of the cavity should largely resemble Gaussian-like Johnson noise overlaid with a possible axion signal. However, because the cavity power was amplified by the microwave receiver, the power measured at the digitizer contained additional structure associated with the frequency-dependent gain of the receiver (i.e. amplifiers, filters, etc). Examples of how this structure, which I refer to as the "RF background", distorts the flat noise power from the cavity are shown in figure 5.3.

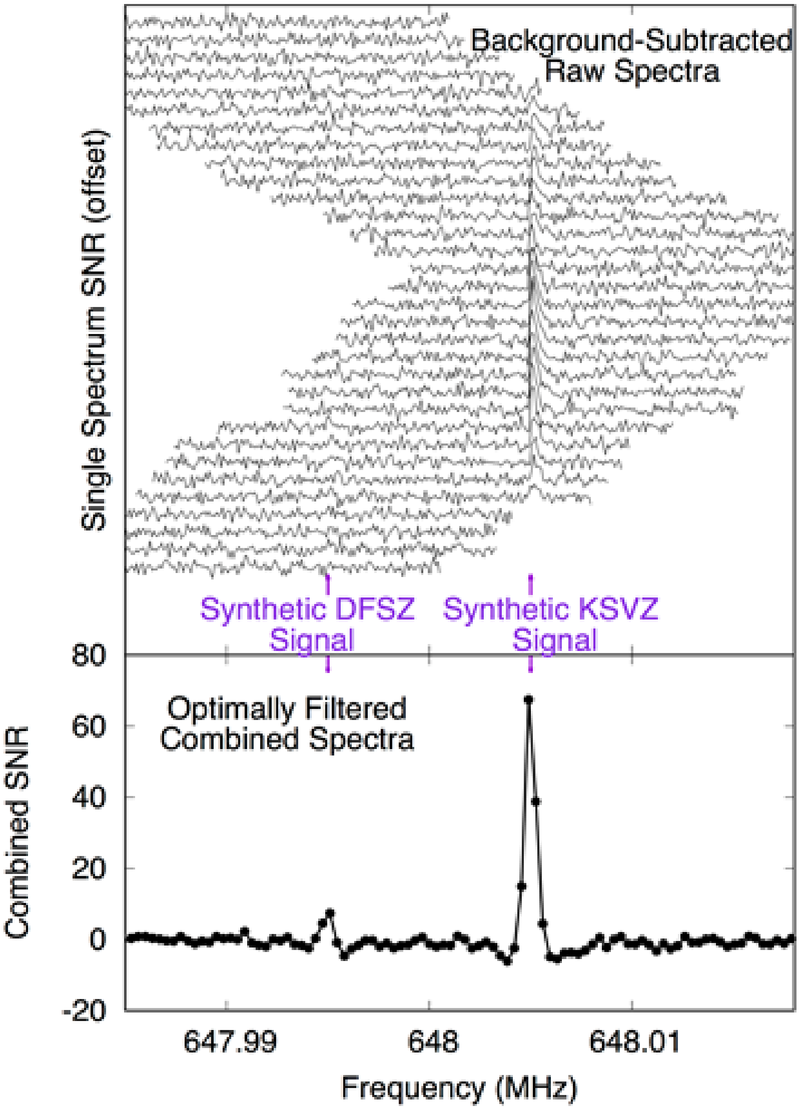

Figure 5.2: An example of constructing a grand spectrum from individual spectra containing both a synthetic KSVZ and DFSZ axion. The horizontal axis is frequency and the vertical axis is the power offset to show several power spectra. Upper: A series of background-subtracted spectra containing software-generated synthetic KSVZ and DFSZ axion signals. Note that a KSVZ signal is visible within a single spectrum, but a DFSZ signal is not. In addition, as the cavity is tuned, represented by the frequency shift of each spectrum, the power of the axion signal is enhanced when the resonant frequency of the cavity is tuned to the frequency of the axion. Lower: The grand spectrum constructed from the individual spectra. Note that both the KSVZ and DFSZ axion signal appear with high SNR.

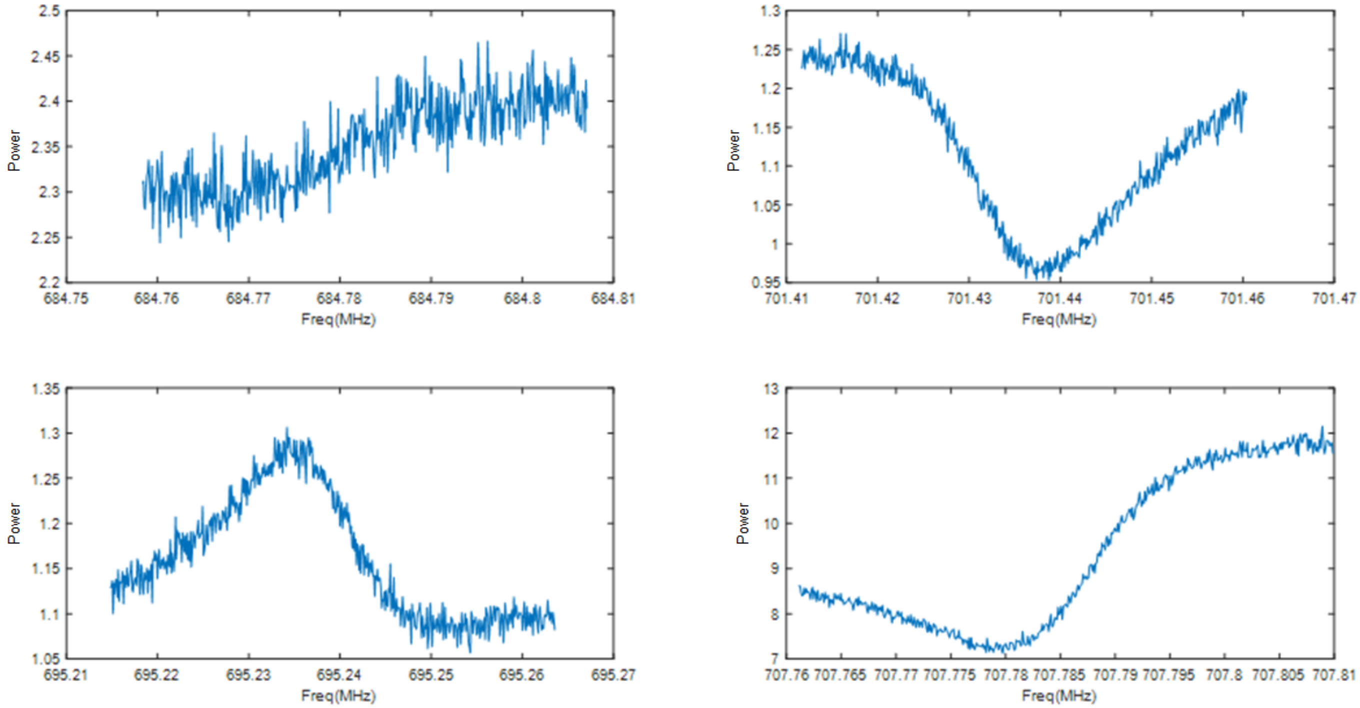

Figure 5.3: Examples of individual spectra. The horizontal axis is the frequency and the vertical axis is the power from the receiver divided by the warm receiver RF background. The variations in shape from spectrum to spectrum arise from the frequency-dependent power gain of the cryogenic receiver.

The removal of this structure was done in two steps. One step was to remove the RF background associated with the warm receiver and another step was to remove the RF background associated with the cryogenic receiver. Broadly speaking, the methodology for removing the RF background in both steps was to determine the contribution of the receiver to the RF background, then, divide the power spectrum by that contribution.

5.2.2 Warm Receiver RF Background

As discussed is section 3.4.5, the warm receiver mixed-down the signal from the cavity to an intermediate frequency of 10.7 MHz for voltage sampling by the digitizer. Because the intermediate frequency was fixed, the RF background of the warm receiver did not vary much from spectrum to spectrum. Thus, the same model for the warm-receiver's RF background was used for all spectra.

To measure the warm-receiver RF background, a broadband Johnson noise source was connected to the input of the warm receiver. Then, several power spectra were taken of the power output from the warm receiver. These spectra were averaged together, and the average of the spectra was fit with a Savitsky-Golay filter (length 121 and polynomial order 4), a digital filter to smooth data by fitting a subset of the data to a polynomial [80]. The Savitsky-Golay filter was selected because it was well-documented for this type of application and computationally simple.

Figure 5.4 shows the the warm-receiver RF background along with the associated fit from the Savitsky-Golay filter. The rise in power towards the ends of the warm-receiver RF background was primarily due to a two-pole bandpass filter in the warm receiver. The two-pole bandpass filter was a physical filter within the warm receiver used to filter signals outside of a 150 kHz bandwidth about the 10.7 MHz intermediate frequency. The bandpass filter was necessary to remove the local-oscillator tones in the mixing stages as well as any additional wideband noise. Due to the shape of this filter, more power was measured at frequencies closer to the edges of the pass band of the filter, resulting in the observed rise in power towards either end of the spectrum.

5.2.3 Cryogenic Receiver RF Background

Following removal of the warm-receiver RF background, there remained residual structure within the individual spectra due to the cryogenic-receiver RF background. To estimate the cryogenic-receiver RF background, each spectrum was fit to a generic 6-parameter polynomial of Padé form,

$$P(x) = \frac{A + Bx + Cx^2 + Dx^3}{1 + Ex + Fx^2}; \; x = \frac{2Q(f - f_0)}{f_0} \text{ [81].} \tag{5.1}$$

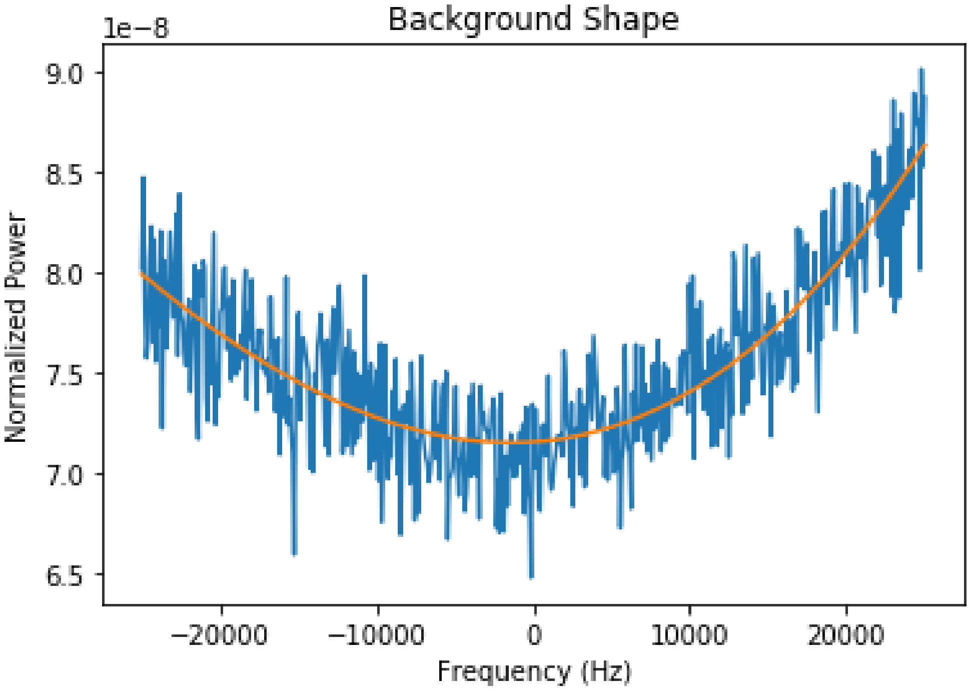

Figure 5.4: A spectrum of the RF background of the warm receiver. The orange line is a fit to the data using a Savitsky-Golay filter. The resulting fit is used in later analysis as the model for the warm-receiver's RF background.

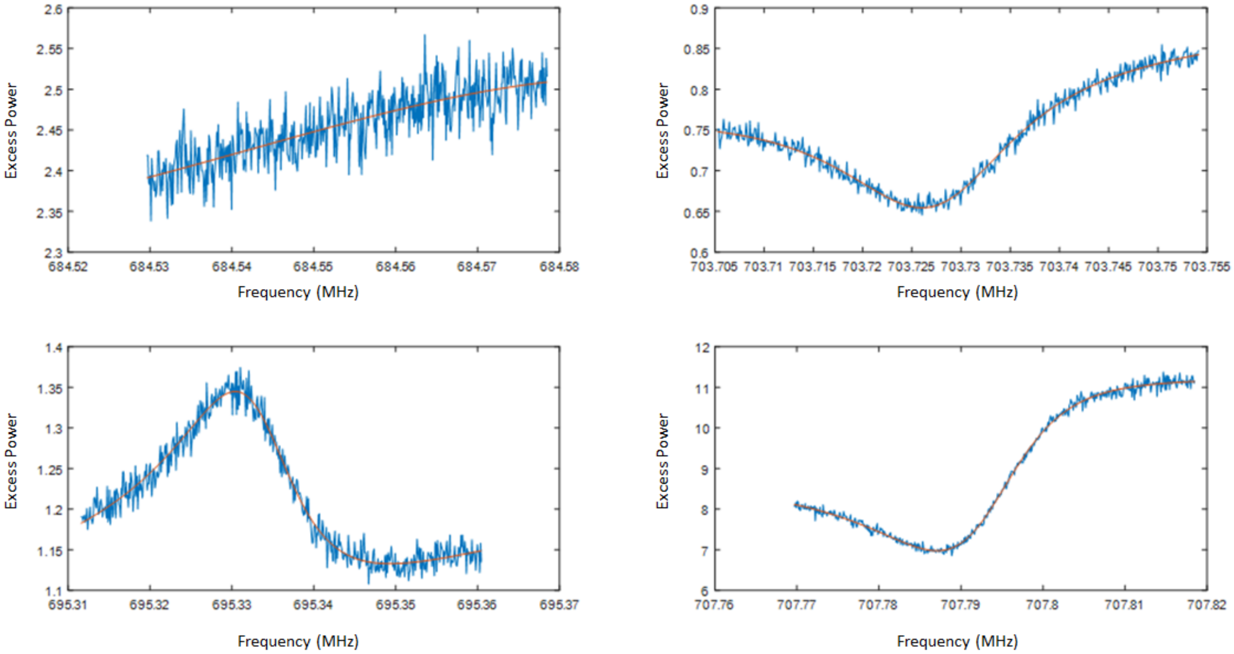

Figure 5.5: Examples of the Padé background fits applied to the spectra shown from figure 5.3.

where A, B, C, D, E,and F are fit parameters, Q is the quality factor of the cavity, and f_0 is the cavity resonant frequency. Figure 5.5 shows the results of the fit applied to the spectra from figure 5.3. It is evident the fit was largely successful at describing the wideband RF background associated with the cryogenic receiver. Because of the narrow width of an axion signal (700 Hz) compared with the bandwidth of a power spectrum (50 kHz), the Padé fit would not remove an axion signal. However, at frequencies near the axion signal, the background fit was skewed by the axion signal. As a result, the measured power of an axion signal was diminished by the fit to the cryogenic-receiver background. The effect this had when setting limits on the axion-to-photon coupling is discussed in section 5.5.2. At this point, I can say this effect occurs for very large axion signals, which are very unlikely to be undetected in this analysis.

We call the power spectrum with the RF background of the receiver removed the “filtered

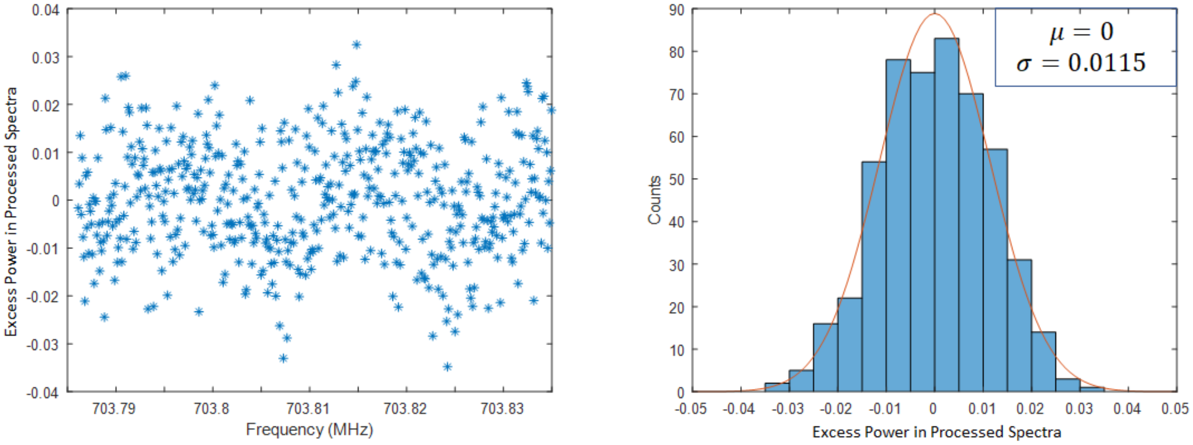

Figure 5.6: Left: A power spectrum in which the RF background has been removed. Right: A histogram of the power from the spectrum on the left. With the RF background removed, the remaining Johnson noise follows a near-Gaussian distribution with a standard deviation of about 0.01.

spectrum". One such filtered spectrum is shown in figure 5.6 (Left). In the absence of any axion signals, we expected filtered spectra to consist of noise which followed a Gaussian-like distribution. Figure 5.6 (Right) shows a histogram of the power in the filtered spectrum and it appeared the noise largely followed an approximately Gaussian distribution. Recall that the expected standard deviation of the filtered spectra could be found from the Dicke-Radiometer equation, $\sigma = 1/\sqrt{tB}$ [52]. In our case, the integration time, t, was 100 seconds and the bin width, B, was 95.7 Hz, so the expected standard deviation was about 0.01 which was approximately what was observed.

Following removal of the warm and cryogenic receiver RF backgrounds, the mean power of a filtered spectrum was identically 1. By subtracting 1 from the power in each bin, the mean power in each bin, referred to as δ_i, was shifted to $\mu = 0$. The measured power in each bin gains a more intuitive meaning, reflecting the excess power about the mean power from the cavity. In the analysis, an axion signal would be observed at some frequency with a positive mean excess power.

5.2.4 Re-scaling Spectra

Following removal of the warm and cryogenic RF backgrounds, we have a number of filtered spectra. However, because experimental conditions varied from spectrum to spectrum, we could not make direct comparisons of the measured power between different spectra. By re-scaling the measured power in each bin of a filtered spectrum, we accounted for these variations in the analysis. The re-scaled power in a given bin is calculated using the equation

$$\delta_i^s = s_i \times \delta_i \tag{5.2}$$

where δ_i^s is the re-scaled power, s_i is the scaling factor, and δ_i is the measured power in the i^{th} bin of the filtered spectrum. The scaling factor, applied to each bin in the filtered spectrum, accounted for variations in the expected SNR of an axion between different spectra. Obviously, the two parameters that affected the SNR of an axion were the system noise temperature and the power of an axion signal. To account for these parameters, the scaling factor used was

$$s_i = \frac{P_{noise}}{P_i} = \frac{k_B B T_{sys}}{P_i} \tag{5.3}$$

where k_B is Boltzmann's constant, T_{sys} is the system noise temperature, P_i is the expected DFSZ axion power in frequency bin i of the filtered spectrum, and B is the width of each bin of a power spectrum. In this section, I will review the motivation for the selected scaling factor, s_i.

The factor kBT_{sys}, accounts for variations in the system noise temperature of the experiment. By multiplying the power in each of a filtered spectrum by kBT_{sys}, the standard deviation of the resulting spectrum became $\sigma_N = \sigma \times kBT_{sys}$, where σ was the the noise in the filtered spectrum. For a given signal power P_{sig}, $SNR = P_{sig}/(\sigma kBT_{sys})$, as expected from the Dicke-Radiometer equation.

The factor P_i, accounted for operating conditions that affected the expected axion power. For example, in individual spectra where the cavity quality factor or form factor were higher, the expected power from an axion signal is larger. The method by which the expected axion power was calculated in discussed in the following section 5.2.5. As a result of re-scaling each bin by $1/P_i$, the expected mean value for a bin with a DFSZ axion signal was $\mu = 1$ and the expected mean value for a bin without an axion signal was $\mu = 0$. In addition, the standard deviation across a power spectrum was no longer uniform. Instead, the standard deviation for a bin was

$$\sigma_i = \frac{k_B B T_{sys} \sigma}{P_i} \tag{5.4}$$

where k_B is Boltzmann's constant, T_{sys} is the system noise temperature, P_i is the expected DFSZ axion power in frequency bin i, B is the bandwidth of each bin of the power spectra, and σ is the standard deviation of the filtered spectrum, typically about 0.01.

We referred to the power spectra following the re-scaling step of the single spectrum analysis as "re-scaled spectra". Figure 5.7 shows an example of one such re-scaled spectrum. The utility of re-scaling the spectrum allowed an "apples-to-apples" comparison of the digitized power between different spectra. Bins from different spectra corresponding to the same frequency could be thought of as Gaussian random variables with the same mean (1 if there is a DFSZ axion and 0 otherwise) and different standard deviations.

5.2.5 Calculating Axion Power

The power of an axion signal in the i^{th} bin of a spectrum is given by the equation,

$$\begin{gathered} P_i = 2.2 \times 10^{-23}\, W \left(\frac{V}{136\ L}\right) \left(\frac{B}{7.6\ T}\right)^2 \left(\frac{C_{010}}{0.4}\right) \left(\frac{g_\gamma}{0.36}\right)^2 \left(\frac{\rho_a}{0.45\ GeV cm^{-3}}\right) \\ \left(\frac{f_i}{740\ MHz}\right) \left(\frac{Q_L}{30,000}\right) \times \left(\frac{1}{1 + 4Q^2((f_i - f_0)/f_0)^2}\right) \times \left(\frac{1 - 2S_{11}}{1 - S_{11}}\right), \end{gathered} \tag{5.5}$$

where g_γ is the model dependent axion coupling, ρ_a is the local dark matter density, f_i is the frequency of the axion ($f_0 = E/h$), B is the magnetic field, V is the cavity volume, Q_L is the loaded quality factor, C_{010} is the form factor of the TM_{010} mode, f_0 is the frequency

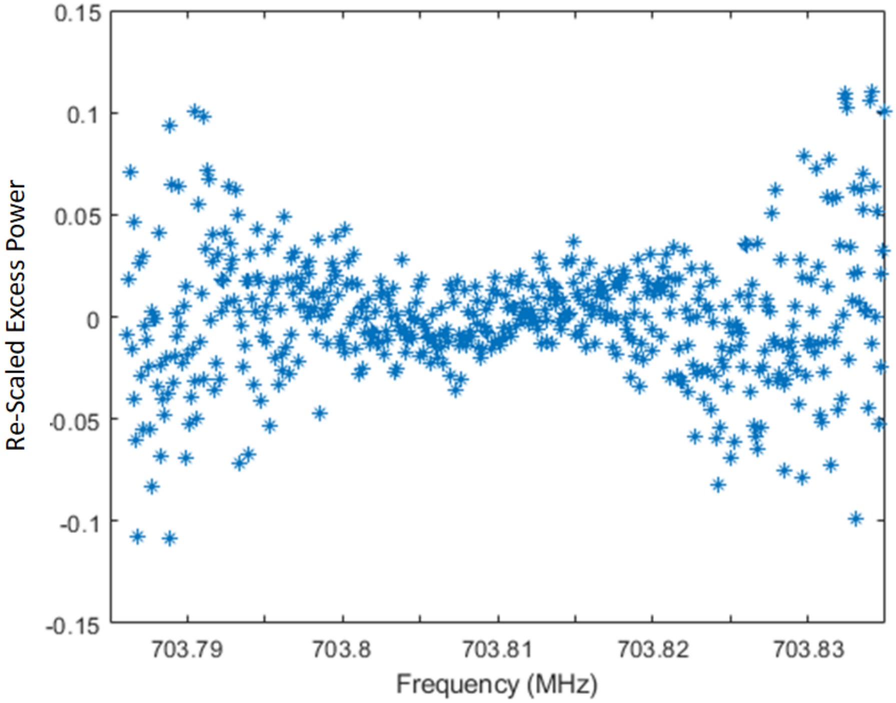

Figure 5.7: An example of a re-scaled spectrum. The increase in standard deviation towards each end of the spectrum was primarily from the decrease in the SNR of an axion from the Lorentzian lineshape of the cavity.

of the cavity, and S_{11} is the coupling parameter. Recall that g_γ, ρ_a, and f_i are parameters fixed by theory predictions and assumptions. Here I will explain how the remaining terms are determined.

$\boldsymbol{C_{010}}$: Recall from section 3.2 that the form factor quantified the overlap between the electric field of the cavity mode, in this case the TM$_{010}$ mode, and the external magnetic field, and is given by

$$C_{010} = \frac{(\int dV E_{010} \cdot B_{ext})^2}{V B_{ext}^2 \int dV E_{010}^2}, \tag{5.6}$$

where E_{010} is the electric field of the TM$_{010}$ mode and B_{ext} is the external magnetic field. The variation over the cavity volume of both the electric field of the cavity mode and the external magnetic field were determined through simulations of the cavity using Computer Simulation Technology (CST) software [82]. The form factor was thereby estimated.

The form factor was calculated in equation 5.6 separately for rod-motion configurations where the rods were both moved clockwise (symmetric) and where one rod was moved clockwise and the other was moved counter-clockwise (anti-symmetric). The resulting form factors were listed in the table shown in table 5.1. For the symmetric configuration, the form factor varied by $< 1\%$ for every 3 MHz and so it was satisfactory, within target errors, to calculate the form factor every 3 MHz. Recall that the anti-symmetric configuration was only used to search for axions across mode crossings which spanned < 1 MHz, and thus it was sufficient to calculate only one form factor for each mode crossing. For any given spectrum, the form factor applied at that frequency was determined through linear interpolation between the values in the table. Overall, the form factor in the symmetric configuration ranged from 0.424-0.441, while in the anti-symmetric configuration it ranged from 0.35-0.37.

$\boldsymbol{B}$: The power of an axion signal developed within the cavity scales as B^2. The value of the magnetic field used in equation 5.5 was the peak magnetic field at the center of the magnet. Of course, the magnetic field varied over the magnet bore. The variations in the magnetic field were simulated in CST and incorporated into the calculation of the form factor [82]. The current through the solenoid magnet was accurately measured by the main-magnet

Cavity TM_{010} Resonant Frequency (MHz)	Form Factor (C_{010})
Symmetric Configuration	
680.6	0.424
683.0	0.428
685.5	0.43
688.1	0.432
690.7	0.433
693.4	0.436
696.2	0.437
699.0	0.438
702.0	0.439
704.5	0.441
Anti-Symmetric Configuration	
740	0.37
750	0.37
780	0.35
781	0.35

Table 5.1: Table of the form factors for run 1B. Form factors were estimated using Computer Simulation Technology (CST) software of the ADMX cavity modes and the modeled external magnetic field [82]. "Symmetric" and "anti-symmetric" refer to the rod configurations used during standard data-taking (symmetric) and over mode crossings (anti-symmetric), as discussed in section 4.3.3.

power supply. The magnetic field was then inferred from the manufacturer's coil constant 8.5 T/ 248.96 A. This ratio was given by the magnet designer and agreed with Biot-Savart calculations and measurements. During run 1B, the main magnet was ramped to 225 A, corresponding to a central magnetic field of 7.68 T. The current was recorded throughout the run, and did not vary by more than 0.01 A.

$\boldsymbol{Q_L}$**,** $\boldsymbol{f_0}$: As discussed previously in section 4.3.1, transmission measurements determined the cavity swept response by applying swept RF power through the cavity over a range of frequencies. The swept response of the cavity was then used to determine the cavity loaded quality factor and resonant frequency.

$\boldsymbol{S_{11}}$: The S_{11} parameter measured how well coupled the antenna was to the mode of the cavity. As discussed in section 4.4, reflection measurements measured the fraction of power reflected off of the strongly-coupled antenna on the cavity. S_{11} was measured as the fraction of power reflected off the strongly-coupled antenna, which was found from the relative size of the trough in the reflection response.

5.2.6 Searching for an Axion Signal

At this stage in the single spectrum analysis, the RF backgrounds had been removed from the raw spectrum and the power in each bin of the resulting filtered spectrum had been re-scaled to account for variations in the SNR of an axion signal. The final step in the single spectrum analysis was to enhance the SNR of axion-like signals by searching the re-scaled spectrum for signals matching the expected axion lineshape. This search was done by convolving the re-scaled spectrum with the expected lineshape of an axion signal

$$\delta^{con,s}(f) = \int \delta^{s}(f') \times g(f', f)\, df', \tag{5.7}$$

where $\delta^{con,s}(f)$ is the processed spectrum following the convolution, δ^{s} is the power in the re-scaled spectrum, and $g(f', f)$ is the axion lineshape of an axion signal as a function of frequency f' with an axion rest mass frequency f. Recall from section 2.6.1 that the lineshape of an axion signal was due to the velocity distribution of axion dark matter in the vicinity of the laboratory. In the analysis, two models were used for the axion lineshape resulting in two separate grand spectra.

The first model used the isothermal sphere halo model for dark matter [53]. In this simple case, the dark matter halo was an isothermal sphere and the lineshape therefore followed a Maxwell-Boltzmann distribution

$$g(f, f_a) = \frac{2}{\sqrt{\pi}} \sqrt{f - f_a} (\frac{3}{f_a \frac{c^2}{<v>}})^{3/2} exp(\frac{-3(f - f_a)c^2}{f_a < v >}), \tag{5.8}$$

where f is the frequency, f_a is the frequency of axion's rest mass, and $< v >$ is the root mean square velocity of dark matter. For the local Milky Way halo, observations suggested the root mean square velocity of $< v^2 >= (270\ km/s)^2$ [53].

N-body simulations, which include more physics and are therefore more realistic, have suggested a narrower velocity distribution. The empirical lineshape predicted from these models is

$$g(f, f_a) = (\frac{f - f_a}{m_a \kappa})^{\alpha} exp(-(\frac{f - f_a}{m_a \kappa})^{\beta}). \tag{5.9}$$

In this model, α, β, and κ are free parameters. For a Milky Way-like halo, the parameters were found to be $\alpha = 0.36 \pm 0.13$, $\beta = 1.39 \pm 0.28$, and $\kappa = (4.7 \pm 1.9) \times 10^{-7}$ [54]. As discussed in section 2.6.1, the narrower lineshape associated with the N-body simulation improves the SNR of ADMX relative to the isothermal-sphere model, as the signal is distributed over a narrower frequency width while the noise is relatively flat. This is our current best estimate of the axion lineshape.

Through the single spectrum analysis any variations between raw spectra due to variations in experimental conditions was accounted for and each raw spectrum was filtered for axion-like signals. The power measured in each bin of the resulting processed spectrum were independent Gaussian random variables with the same mean ($\mu = 1$ if there is a DFSZ axion and $\mu = 0$ if there is no axion signal) and different standard deviation. Then, by co-adding the processed spectra together, we could boost the SNR of an axion signal such that it would be easily observable.

5.3 Constructing a Grand Spectrum

As shown in figure 5.2, a grand spectrum was constructed by co-adding together individual processed spectra; doing so increased the SNR of an axion signal so that it could be readily detected above the noise. In this section, I will discuss the details of constructing a grand spectrum from the processed spectra.

5.3.1 Weighting

Recall that each of the processed spectra are Gaussian random variables of the measured power from the cavity with the same mean ($\mu = 1$ if there is a DFSZ axion and $\mu = 0$ if there is no axion signal) and different standard deviations. By co-adding together the measured power in all bins corresponding to the same frequency, we increased the SNR of an axion signal. To optimize the SNR of an axion signal in the grand spectrum, the run 1B analysis utilized an inverse-weighting method for co-adding together spectra [83]. Using this method, power measurements with a smaller standard deviation (i.e. Higher quality data) was weighted more strongly compared to measurements with a larger standard deviation. This method was first used by Edward Daw [79] and was proven to minimize the variance of the excess power for a given bin in the grand spectrum. Using this weighting method, the excess power for a bin w in the grand spectrum was calculated as

$$P_w = \frac{\sum_i \frac{p_i}{\sigma_i^2}}{\sum_i \frac{1}{\sigma_i^2}} \tag{5.10}$$

where p_i is excess power in i^{th} bin of the processed spectrum and σ_i is the variance in the bin. The summation was over all bins corresponding to a given frequency bin in the grand spectrum. Similarly, the standard deviation for a bin w in the grand spectrum was calculated as

$$\sigma_w = \sqrt{\frac{1}{\sum_i \frac{1}{\sigma_i^2}}}. \tag{5.11}$$

The grand spectrum was defined by these two quantities, the measured excess power P_w and the standard deviation σ_w. The procedure for using the grand spectrum to search for potential axion signals is discussed in section 5.4.1.

5.3.2 Applying Cuts on Spectra

As was expected, there were cases where some of the data collected during the run was not used because it contained unphysical values or because the cavity mode had been lost. Cuts were therefore applied in the analysis to remove these spectra before they were added into the grand spectrum. The values of the cuts are shown in table 5.2 and discussed below.

Cuts on the quality factor removed individual spectra where the resonant frequency of the cavity was “lost”. These were flagged as instances where the transmission measurements through the cavity was flat noise. The fit to the resulting transmission measurement was poor and gave a nonsense quality factor. The range in the cuts shown in table 5.2 represented acceptable quality factors predicted by simulation, thus anything outside this range was likely the result of losing the mode. (In the case an axion signal was present in the transmission measurement, the expected power of the axion signal is small relative to the swept RF power. Even if an axion signal were present during a transmission measurement, it would not significantly effect the measured quality factor.)

The cuts on system noise were used to remove spectra where the noise temperature was mismeasured. The lower bound, $T_{sys} < 0.1$ K, represented an unphysical noise temperature where the system noise temperature was lower than the physical temperature of the cavity. On the other hand, measurements in which $T_{sys} > 2.0$ K corresponded to a noise temperature significantly higher than what would be expected from a JPA operating at a physical temperature of 230 mK. Both cases were the result of errors in the JPA SNRI measurement, often due to a change in the state of the receiver. For example, unexpected heating of the

JPA would have caused the JPA gain to drop by over 20 dB, resulting in a higher than expected system noise temperature. (Again, in the case an axion signal was present during an SNRI measurement, the power from an axion signal was small enough that it would not effect the measured power from the cavity. As a result the effect of an axion signal on noise temperature measurements was minimal, so spectra containing an axion signal would not be affected by the cuts.)

Cut were also applied on spectra in which the RF background was not successfully removed. During the RF background removal process, if the χ^2 per degree of freedom of the 6^{th} order Padé fit to the cryogenic RF background was greater than 2, the spectrum was cut because the fit to the cryogenic RF background was poor. In such cases, the processed spectra contained residual structure in addition to the expected noise and possible axion signal. (Again, in the case an axion signal was present in a spectrum, the low power and narrower relative width of an axion signal would not have been enough to result in a χ^2 per degree of freedom of greater than 2.)

A number of other cuts were applied on spectra within a given range of time and/or frequency. These "timestamp cuts" were primarily applied to remove spectra containing blindly injected synthetic axion signals after they had been revealed. In addition, such cuts were used in cases where it had been verified through widescan measurements that the power spectra had been centered on the wrong resonant mode of the cavity.

In total, the cuts applied on the collected spectra removed about 12,000 out of approximately 190,000 spectra from the analysis.

5.4 ADMX Results

Following the construction of the grand spectrum, we were finally able to identify axion candidates. In this section, I will review the criteria for identifying potential axion candidates. Then, I will discuss the procedures to verify whether candidates are consistent with a real axion signal. Finally, I will discuss limits placed on the axion-to-photon coupling across the explored axion mass range.

Parameter	Constraint	Spectra Removed
Quality Factor	10,000< Q <120,000	316
System Noise	0.1 K< T_{sys} <2.0 K	4,514
Error in Filter Shape	N/A	249
“Timestamp Cuts”	N/A	7,189

Table 5.2: List of cuts applied to the run 1B spectra. In total, 12,265 spectra were cut from the grand spectrum.

5.4.1 Axion Candidates

As discussed in section 4.3.1, the scanned frequency range was divided into several 10-MHz wide “nibbles”. In each nibble, after the frequency range had been scanned such that the SNR for a DFSZ axion was at least 3.0, a grand spectrum was constructed for the nibble. Recall that in the grand spectrum, each frequency bin (w) contains a measured power (P_w) and standard deviation (σ_w). From the grand spectrum, potential axion candidates were identified as bins in the grand spectrum satisfying either of the following criteria:

1. The 90% upper limit on the excess power at the frequency bin (w) was not less than the power of a DFSZ axion. In other words, we would not have been able to exclude a DFSZ axion signal at that frequency ($P_{DFSZ} < P_w + 1.281\sigma_w$).

   - or -

2. The power measured at that frequency bin (w) exceeded $3\sigma_w$. ($P_w > 3\sigma_w$). This criterion was selected to identify instances in the grand spectrum of a statistically significant excess of power.

The goal of the first criterion was to ensure that we could exclude a DFSZ axion across the whole frequency range explored by run 1B. Frequency bins violating the first criterion were identified as bins in the grand spectrum where a 90% confidence upper limit on the power in the bin was greater than the power predicted by a DFSZ axion signal. In the analysis, these were cases where $P_{DFSZ} < P_w + 1.926\sigma_w$.

While the first criterion identified axions signals with DFSZ coupling or greater, it would not as confidently identify axion signals that were weaker than a DFSZ axion. The power of an axion signal could have been less than DFSZ if the local axion dark matter density was less than expected or if the axion-to-photon coupling was weaker than DFSZ. While the scan rate during data taking did not in general provide sensitivity to such weak signals, there were however frequency ranges where enough data were taken that such a weak signal could have been observable. To identify signals more weakly coupled than DFSZ, the second criterion was introduced which identified candidates for which the excess power was statistically significant. The analysis identified candidates fulfilling the second criterion as frequency bins where $P_w > 3\sigma_w$.

The candidate-rescan procedure and the procedure for synthetic axion unblinding were discussed in sections 4.8 and 4.8.1, respectively. Frequencies identified as potential axion candidates were rescanned usually at least for twice as long thereby significantly increasing the SNR for a potential axion signal. The data from the initial scan and rescan were then combined, and axion candidates that remained candidates in the combined dataset were identified as persistent axion candidates. Recall that synthetically-injected axions were unblinded either before a second rescan of persistent axion candidates (class 1) or before a magnet-ramp procedure (class 2). At this stage, class 1 synthetic-axion injections were unblinded, and the frequency regions at the injections were rescanned to allow a search for possible axion signals at synthetic-axion frequencies. The data for the second rescan was analyzed independently from the previous data, and if the axion candidate continued to persist it was subjected to further detailed analysis.

Over the course of run 1B, 3 persistent candidates were identified. Table 5.3 lists these persistent candidates requiring further analysis. For these candidates, further analysis were applied to determine if they remained axion candidates or were likely due to external sources such as radio frequency interference (RFI).

Candidate Frequency (MHz)	Power (DFSZ Axion Power)
686.310	2.36
730.195	1.51
780.255	1.49

Table 5.3: A table of persistent axion candidates detected within the experiment and the measured power at the candidate frequency, relative to a DFSZ axion.

5.4.2 Candidate-Veto Procedure

Over the course of run 1B, ADMX searched for axions from 680–790 MHz. Within this range, three persistent candidates were observed, at 686.310, 730.195, and 780.255 MHz. Each of the three persistent candidates was analyzed individually to determine whether the signals were from an axion or another source.

First, persistent candidates were analyzed to study how the power of the candidate changed as the cavity was tuned. A true axion signal would develop within the resonant cavity such that the signal power would increase as the cavity resonance was tuned to the signal frequency. On the other hand, external interference could be picked up by components elsewhere in the receiver chain, so that the signal power could be largely independent of the cavity resonant frequency. By measuring how the power of a candidate changed as the resonant frequency of the cavity changed, we could examine whether the signal developed consistent with an axion. We found candidate signals at 686.310 and 780.255 MHz did not maximize on-resonance, indicating they were likely due to external radio interference and therefore could be excluded as axions.

Another method for vetoing persistent candidates was to study how the power of the candidate changed as the magnetic field was ramped. Recall from equation 5.5, the expected power of an axion signal scaled as $P \ \alpha \ B^2$. Therefore, a reduction in the strength of the magnetic field would result in a reduction in the power of a true axion signal. On the other hand, the power of signals from other external sources, such as RFI interference, would likely not be greatly affected by the strength of the magnetic field. By ramping down the magnetic field, e.g. to half the operating field, and measuring the power of the candidates, we could determine whether a candidate behaved as expected for a true axion.

The signal at 730.195 MHz, shown in figure 5.8, maximized on resonance and was consistent in power and linewidth to the signal expected from a DFSZ axion. This result triggered a decision by the candidate detection committee to ramp the magnetic field down to study whether the power of the signal would scale as B^2, in a manner consistent with an axion signal. However, before the procedure was initiated, on unblinding the candidate it was found to be a class 2 synthetic-axion signal. On finding this, the synthetic injection at this frequency was disabled and the frequency region near the candidate was rescanned. No signal then appeared at 730.195 MHz, and thus all candidate axion signals were excluded; no candidates survived. We concluded that either the axion was not within the explored range, that the axion dark-matter density is a small fraction of the halo density ($\rho_a < 0.45$ GeV/cc), or that the axion-photon coupling constant is significantly below the prediction for DFSZ ($g_\gamma < 0.36$).

5.5 Setting Limits on the Axion Coupling

In the absence of persistent axion-like signals, the data from run 1B was used to set limits on the axion-to-photon coupling between the axion mass range $2.81 - 3.31\ \mu eV$. The general strategy for setting limits on the axion-to-photon coupling was to first place a limit on power of a signal developed within the cavity, P_{exc}, for each frequency bin of the grand spectrum. The limit on the power from the cavity at this frequency could then be translated to a limit on the axion-to-photon coupling using the relation

$$\frac{g^2_{a\gamma\gamma}(exc)}{g^2_{a\gamma\gamma}(DFSZ)} = \frac{P_{exc}}{P_{DFSZ}} \tag{5.12}$$

where $g^2_{a\gamma\gamma}(DFSZ)$ is the axion-to-photon coupling constant for a DFSZ axion, P_{DFSZ} is the expected power for a DFSZ axion at that frequency in the ADMX experiment, and P_{exc}

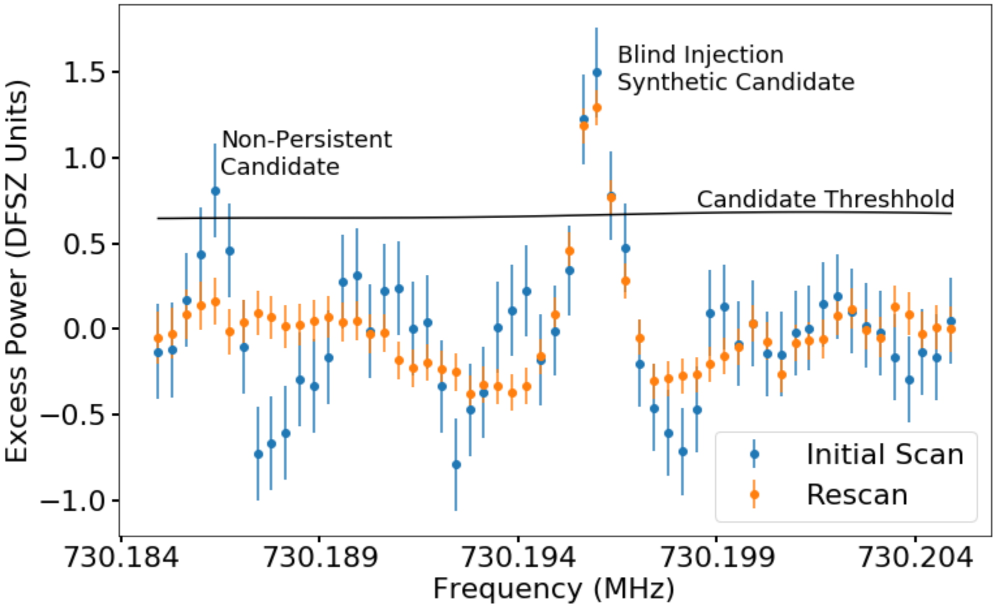

Figure 5.8: A subset of the grand spectrum showing the synthetically-injected axion candidate at 730.195 MHz. The vertical axis is the excess power from the cavity normalized with respect to the power of a DFSZ axion. *Blue* The power measured during the initial scan. *Orange* The power measured during a rescan with about 4 times more integration time. The prominent peak centered at 730.195 MHz on unblinding was revealed to be to a synthetic axion identified in the analysis that persisted after a rescan; the small peak to the left at 730.186 MHz was a candidate that did not persist in the rescan. As an aside, notice that because of a mismatch in the fit to the RF background in the presence of an axion signal, the power at the frequencies surrounding the candidate are suppressed. This can be seen at frequencies surrounding the 730.195 MHz candidate.

is the limit placed on the power of the signal from the cavity. P_{DFSZ} is calculated using equation 2.13, assuming a dark matter halo density of 0.45 GeV/cc for the standard dark matter halo model (or a dark matter halo density of 0.65 GeV/cc for the N-body model for axion dark matter structure formation). These limits were established assuming that axions saturate the local dark matter. For models where axions comprise a smaller percentage of the local dark matter, the limits would be increased by a factor ρ_{DM}/ρ_{axion}, where ρ_{DM} is the total dark matter density and ρ_{axion} is the density of axion dark matter.

5.5.1 Calculating the Upper Limit of Power from the Cavity

Recall that a frequency bin (w) of the grand spectrum contains information about the measured excess power, P_w, and the standard deviation in the power from the cavity, σ_w. For each bin, the measured power and standard deviation were used to establish, with 90% confidence, a lower limit on the power in the bin. As previously discussed, the noise within the grand spectrum was mainly Johnson noise which has a largely Gaussian-like distribution. Thus in a given bin, the confidence level for a signal exceeding P_{exc}, for a bin with power P_w and standard deviation σ_w, was generically given by

$$c.l.(P_{exc}) = \frac{1}{\sqrt{2\pi}} \int_{-\infty}^{(P_{exc}-P_w)/\sigma_w} e^{-x^2/2} dx = \frac{1}{2}(1 + erf(\frac{P_{exc}/\sigma_w - P_w/\sigma_w}{\sqrt{2}})). \tag{5.13}$$

Note that this was consistent with calculating the confidence level for a normal distribution with a sample mean of $\mu = P_w$ and standard deviation σ_w.

Because an axion signal was only observable as an excess of power above the noise, we did not need to be concerned with cases where $P_w < 0$. For cases where the measured power was negative, a mean power of $\mu = P_w = 0$ was used. In addition, a re-normalized normal distribution was used in which the probability of a negative power excess was 0. The approach of neglecting cases where $P_w < 0$ when setting limits was conservative because it neglected cases where there could have been a small axion signal in addition to a larger negative deviation in the noise power. Therefore, the limits set from this approach were

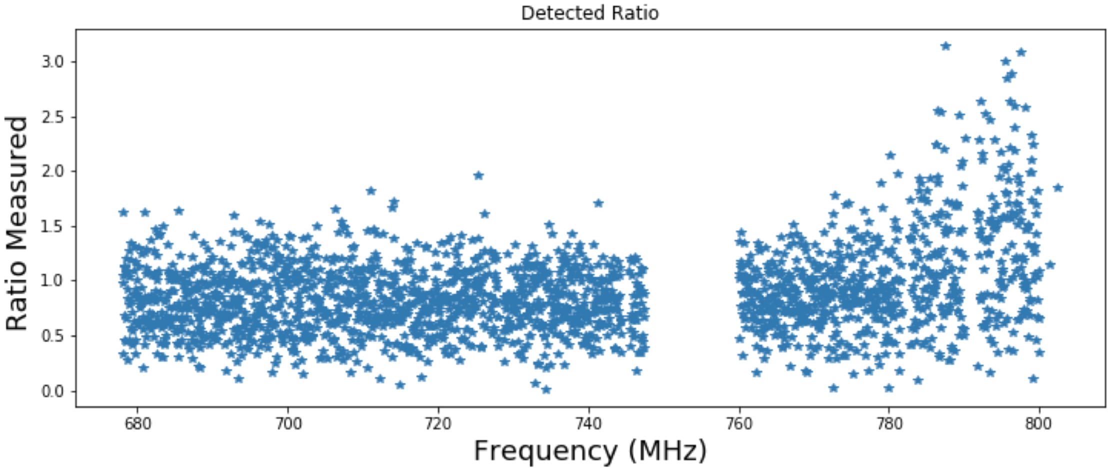

Figure 5.9: In total, 20,000 axion signals were injected into spectra through computer software. The ratio of the injected to measured power across the frequency range is shown. On the vertical axis is the ratio of the measured power in the grand spectrum to the power of the injected axion. On average, it was observed that the power of the injected axion was diminished by a factor of 0.82 due to the fit to the RF background of the cryogenic receiver.

conservative.

5.5.2 Determining the Suppression of Axion Signals

Recall from section 5.2.1 that a 6-order Padé approximate is used to remove the cryogenic-receiver RF background. As a result of the fit, the power of an axion signal was suppressed. To determine the amount of suppression in the axion signal, 20,000 software-injected signals with known powers between those expected for DFSZ and KSVZ axions were injected across the frequency range of the run. Figure 5.9 plots the ratio of power detected by the analysis to the power of the injected signal. On average, it was found that the signal power of an axion from the cavity was diminished by a factor of 0.82 due to fit to the RF background of the cryogenic receiver. This effect was accounted for below in the reported limits.

5.5.3 Run 1B Limits

Given the absence of axion-like signals, a 90% upper confidence limit was set on the axion-photon coupling over the scanned mass range, shown in figure 5.10 (Green). The frequency gaps in the limits were frequency ranges where mode crossings reduced the form factor to the extent that the experiment was no longer sufficiently sensitive to DFSZ axion dark matter. The lighter and darker shades corresponded to the limits set for the Maxwell-Boltzmann and N-body models for the Milky Way axion dark matter halo. Shown in orange are previous ADMX limits published in 2018 [57] using a Microstrip SQUID amplifier (MSA), and shown in blue are yet earlier limits set by ADMX reported in 2010 [56]. Note that the limits set in 2010 required several years data-taking to establish. In comparison, the limits reported in this thesis were set after a search of less than a year. The significant increase in scan rate was due to the increased sensitivity of the experiment.

The results presented in this thesis excluded not only the KSVZ axion, but also the much more compelling DFSZ axion. In addition, the results represented a factor-of-four increase in mass coverage over the limits reported in [57]. Notably, ADMX continues to be the only axion haloscope to be sensitive to DFSZ axions over the plausible QCD dark-matter mass range. To reach this sensitivity has been a many-year long project that required the efforts of not only myself, but numerous collaborators. ADMX continues to search for axions at higher masses with similar sensitivity, and a discovery could happen at any moment.

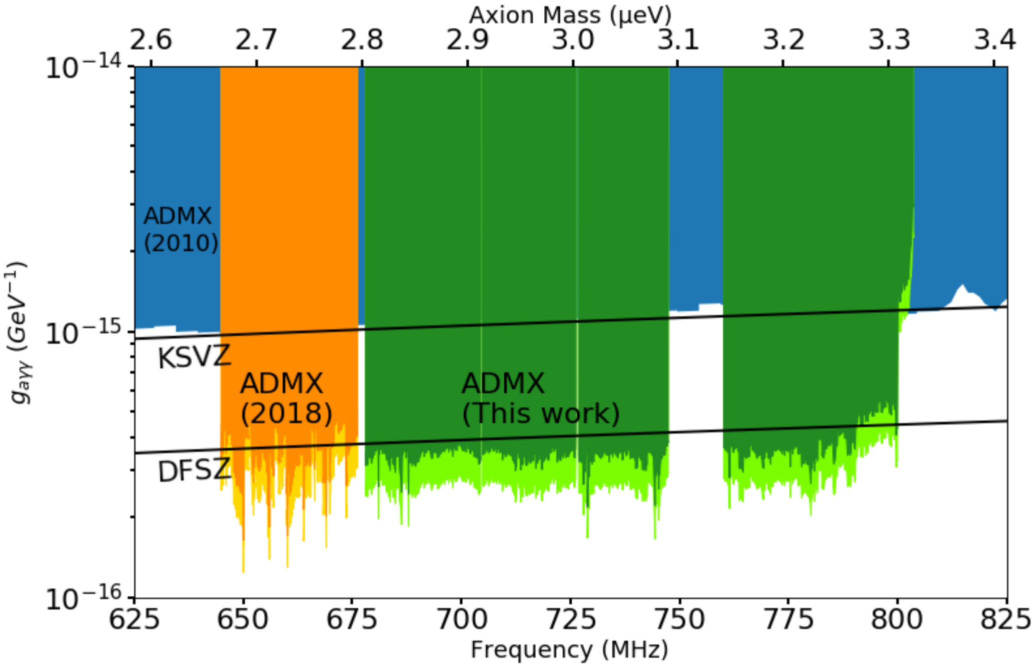

Figure 5.10: 90% confidence exclusion on axion-photon coupling as a function of axion mass (Upper Axis) or frequency (Lower Axis) for the Maxwell-Boltzmann (MB) dark-matter model and N-body model. *Blue* Previous limits reported in [84]. *Orange* Previous limits reported in [57]. *Green* Limits from this work. Darker shades indicate limits set for the MB model [53] and the lighter shade indicate limits set for the N-body model [54].

Chapter 6

DISCUSSION AND CONCLUSIONS

In chapter 2, I discussed how the axion is a hypothetical elementary particle that elegantly solves the Strong-CP problem [20, 21, 22] and accounts for dark matter in the Universe [15, 85, 86, 87, 88]. The possible parameter space for axion dark matter is fairly well constrained in mass and axion-to-photon couplings. In order to account for 100% of the dark matter in the Universe, the axion mass is constrained to 1-100 μeV [89, 90, 91, 92, 93, 94]. The range of plausible couplings for the axion are constrained by two benchmark models for the axion, the KSVZ [23, 24] and DFSZ [25, 26] axion. While the DFSZ axion model is almost an order of magnitude more weakly coupled to photons, it is especially compelling because it satisfies the constraints for grand unified theories [25] which is suggested by the Strong-CP problem. In addition, because of the sketchy theoretical motivation for axions that are more weakly coupled than DFSZ, an experiment that is sensitive to the DFSZ axion in a given mass range can likely detect or eliminate an axion in that range.

Axion haloscopes are the most sensitive class of experiment to search for axion dark matter. Indeed they are the only experiments sensitive to DFSZ axions. In the class of haloscope experiments, ADMX, the experiment that lies at the heart of my thesis, is the most sensitive axion haloscope. In chapter 4, I discussed how ADMX achieved this sensitivity by using ultra-low noise quantum amplifiers and cooling the experiment to temperatures on the order of 100 mK with a dilution refrigerator.

6.1 Operating ADMX

Previous limits set by ADMX excluded the DFSZ axion in the mass range from $2.66 - 2.81\ \mu eV$ [57]. Those limits marked ADMX as the first axion haloscope to achieve sensitivity to both the KSVZ and DFSZ axion. To achieve this sensitivity has been a many-year long project, on which I have been grateful to play a role. Following the 2017 run, ADMX underwent several upgrades including employing a Josephson parametric amplifier (JPA) and the integration of a system for synthetic axion injection. In 2018, ADMX successfully searched for axions with these upgrades.

The 2018 run was the first time ADMX had utilized a JPA, and the results were successful. The JPA provided over 20 dB of power gain with ultra-low noise over a 10-20 MHz bandwidth. By regularly re-biasing the JPA to tune the JPA resonance to match the cavity resonance, the explorable mass range was increased by a factor of 4 compared to the 2017 run. In future runs, ADMX will continue to use JPAs that operate at higher frequencies to search for higher mass axions, and the experience gained from operating with a JPA in this run will be critical.

The synthetic axion generator (SAG) enabled the injection of axion-like signals into the ADMX cavity. As discussed in this thesis, this was a powerful tool for testing the response of the ADMX receiver to axion-like signals and the ability of the ADMX analysis to identify axion-like signals. The use of the SAG for blinded axion injections into the experiment helped us to exercise our candidate detection and rescan methodologies. Future runs of ADMX will continue to use the SAG to ensure that the ADMX is always prepared to identify axion signals.

In the results reported in this thesis, the coverage of ADMX was expanded a factor of 4 to exclude axions in the mass range from $2.81 - 3.31\ \mu eV$ [58], effectively ruling out axion dark matter within the mass range. The limits set by ADMX by this thesis are shown alongside other experiments in figure 6.1. As shown in the figure, ADMX continues to be the only haloscope experiment sensitive to the DFSZ axion.

6.2 Future Work

ADMX will continue to search for axion dark matter at higher mass ranges to equal or better sensitivity. We sense that if the axion is not found in the currently-accessible mass

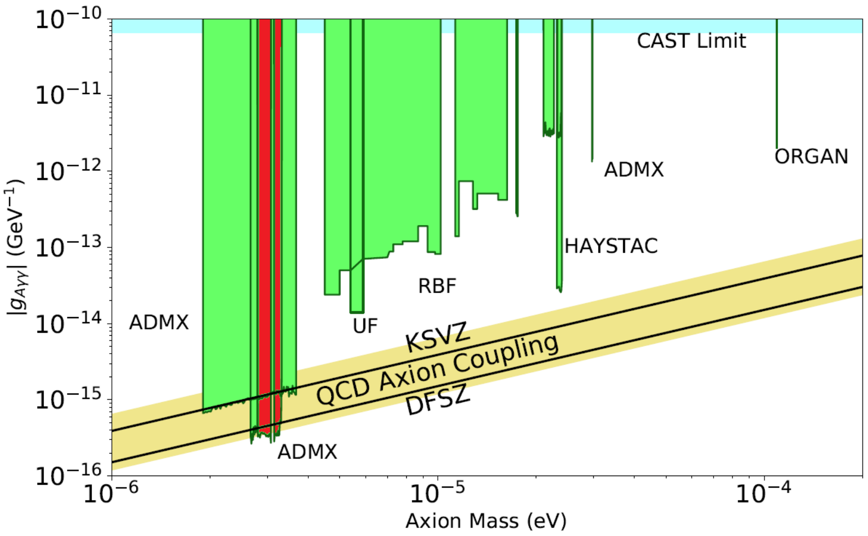

Figure 6.1: Limits on the axion to photon coupling as a function of the mass of the axion by this thesis (Red) and various other experiments (Green). In addition, the band of plausible couplings for the axion to solve the Strong-CP problem are shown in yellow, including the KSVZ and DFSZ axion. PC: Particle Data Group [39].

range, then higher masses are a more promising place to look. In the search for higher mass axions, we aim to either discover axion dark matter or rule it out within that mass range. However, the search for axion dark matter at higher masses is not without challenges. As the wavelength of the expected photon signal becomes smaller, the volume of the resonators also naturally becomes smaller, which in turn decreases the expected power of an axion signal.

A number of designs are currently being developed to boost the signal-to-noise ratio for an axions at higher masses, and while they are not relevant to this thesis, they are worthy of note. Several examples of designs for higher mass axion searches are shown in figure 6.2. In its current iteration (Top Left), ADMX uses the same cavity system with larger tuning rods to search for higher mass axions. In addition to that, a multi-cavity system (Top Right) is being developed that coherently combines the signal from four smaller diameter resonators to boost the signal-to-noise of an axion. For extremely high mass axions ($m_a > 25\ \mu eV$), an experiment named “Orpheus” (Bottom) is being developed at the University of Washington by fellow graduate student, Raphael Cervantes. This experiment will search for axion dark matter with higher order TM_{0n0} modes and makes use of dielectric materials to compress the electric field anti-parallel to the external magnetic field in order to minimize the reduction in form factor. Similar to the work presented in this thesis, these experiments will search for axion dark matter to high sensitivity, expanding the mass range covered by ADMX, and enabling ADMX to either detect the axion or exclude it within that mass range. An axion discovery could be made at any moment!

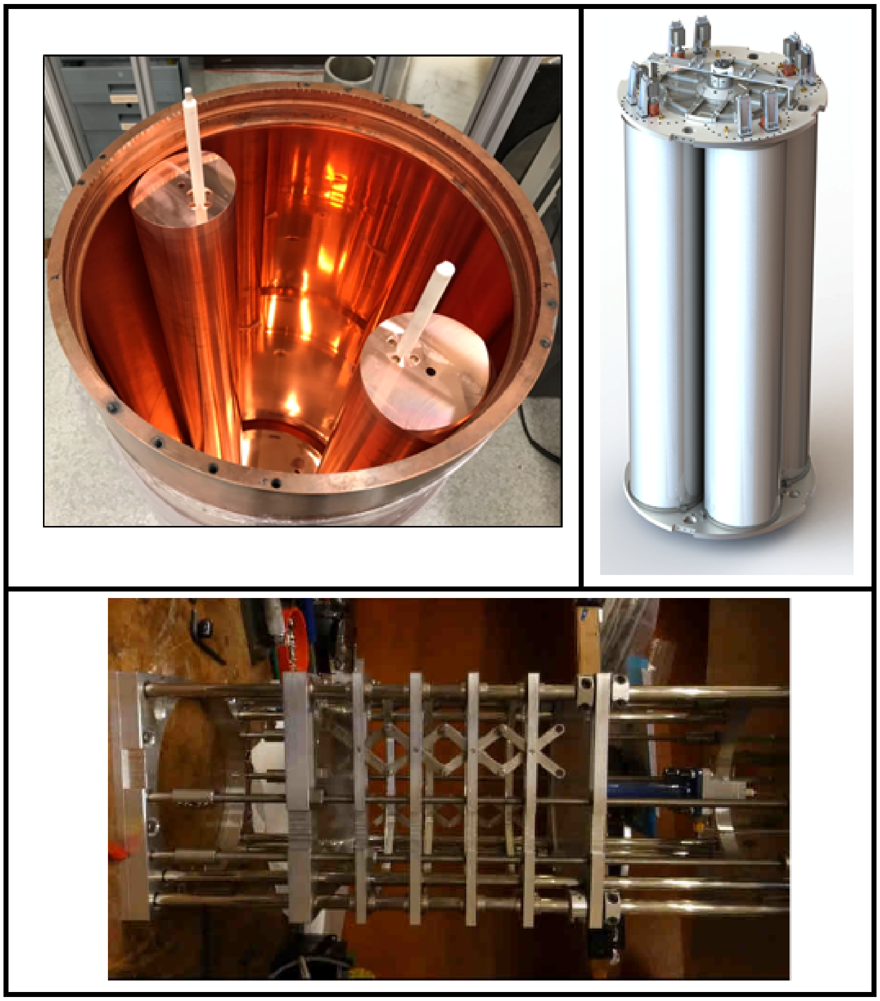

Figure 6.2: Experiments in development for higher mass axion searches. Top Left: Using the same cavity system but with larger tuning rods, ADMX is currently searching for axion dark matter up to 4.22 μeV. Top Right: Higher frequency searches will require smaller diameter cavities. To increase the SNR, multiple cavities tuned to the same resonant frequencies will be used with the signals from the cavities added coherently. Bottom: At even higher frequencies ($m_a > 25\ \mu eV$), traditional cavities are too small to be sensitive to axion signals. Orpheus, at the University of Washington, will search for axions using higher order modes. Using evenly spaced dielectrics, the reduction in form factor typically associated with higher order modes will be reduced.

BIBLIOGRAPHY

[1] Jonathan L. Ouellet, Chiara P. Salemi, Joshua W. Foster, Reyco Henning, Zachary Bogorad, Janet M. Conrad, Joseph A. Formaggio, Yonatan Kahn, Joe Minervini, Alexey Radovinsky, Nicholas L. Rodd, Benjamin R. Safdi, Jesse Thaler, Daniel Winklehner, and Lindley Winslow. First Results from ABRACADABRA-10 cm: A Search for Sub-μeV Axion Dark Matter. *Phys. Rev. Lett.*, 122:121802, Mar 2019.

[2] L. Zhong, S. Al Kenany, K. M. Backes, B. M. Brubaker, S. B. Cahn, G. Carosi, Y. V. Gurevich, W. F. Kindel, S. K. Lamoreaux, K. W. Lehnert, S. M. Lewis, M. Malnou, R. H. Maruyama, D. A. Palken, N. M. Rapidis, J. R. Root, M. Simanovskaia, T. M. Shokair, D. H. Speller, I. Urdinaran, and K. A. van Bibber. Results from phase 1 of the HAYSTAC microwave cavity axion experiment. *Phys. Rev. D*, 97:092001, May 2018.

[3] Edward W Kolb and Michael S Turner. The Early Universe. *Nature (London)*, 294(5841):521–526, 1981.

[4] Alan H. Guth. Inflationary universe: A possible solution to the horizon and flatness problems. *Phys. Rev. D*, 23:347–356, Jan 1981.

[5] Alain Coc and Elisabeth Vangioni. Primordial nucleosynthesis. *International Journal of Modern Physics E*, 26(08):1741002, Aug 2017.

[6] Matthias Steinmetz and Julio F. Navarro. The hierarchical origin of galaxy morphologies. *New Astronomy*, 7(4):155–160, Jun 2002.

[7] Gianfranco Bertone and Dan Hooper. History of dark matter. *Rev. Mod. Phys.*, 90:045002, Oct 2018.

[8] J. H. Oort. The force exerted by the stellar system in the direction perpendicular to the galactic plane and some related problems. *Bulletin of the Astronomical Institutes of the Netherlands*, 6:249, August 1932.

[9] V. C. Rubin, Jr. Ford, W. K., and N. Thonnard. Rotational properties of 21 SC galaxies with a large range of luminosities and radii, from NGC 4605 (R=4kpc) to UGC 2885 (R=122kpc). *The Astrophysical Journal*, 238:471–487, June 1980.

[10] K. G. Begeman, A. H. Broeils, and R. H. Sanders. Extended rotation curves of spiral galaxies: dark haloes and modified dynamics. *Monthly Notices of the Royal Astronomical Society*, 249:523, April 1991.

[11] A. N. Taylor, S. Dye, T. J. Broadhurst, N. Benitez, and E. van Kampen. Gravitational Lens Magnification and the Mass of Abell 1689. *The Astrophysical Journal*, 501(2):539–553, Jul 1998.

[12] Steven W. Allen, August E. Evrard, and Adam B. Mantz. Cosmological Parameters from Observations of Galaxy Clusters. *Annual Review of Astronomy and Astrophysics*, 49(1):409–470, Sep 2011.

[13] A. A. Penzias and R. W. Wilson. A Measurement of Excess Antenna Temperature at 4080 Mc/s. *The Astrophysical Journal*, 142:419–421, July 1965.

[14] D. N. Spergel, L. Verde, H. V. Peiris, E. Komatsu, M. R. Nolta, C. L. Bennett, M. Halpern, G. Hinshaw, N. Jarosik, A. Kogut, M. Limon, S. S. Meyer, L. Page, G. S. Tucker, J. L. Weiland, E. Wollack, and E. L. Wright. First-Year Wilkinson Microwave Anisotropy Probe (WMAP) Observations: Determination of Cosmological Parameters. *The Astrophysical Journal Supplement Series*, 148(1):175–194, Sep 2003.

[15] N. Aghanim, Y. Akrami, M. Ashdown, J. Aumont, C. Baccigalupi, M. Ballardini, A. J. Banday, R. B. Barreiro, N. Bartolo, and et al. Planck 2018 results. *Astronomy & Astrophysics*, 641:A6, Sep 2020.

[16] Adam G. Riess, Alexei V. Filippenko, Peter Challis, Alejandro Clocchiatti, Alan Diercks, Peter M. Garnavich, Ron L. Gilliland, Craig J. Hogan, Saurabh Jha, Robert P. Kirshner, B. Leibundgut, M. M. Phillips, David Reiss, Brian P. Schmidt, Robert A. Schommer, R. Chris Smith, J. Spyromilio, Christopher Stubbs, Nicholas B. Suntzeff, and John Tonry. Observational Evidence from Supernovae for an Accelerating Universe and a Cosmological Constant. *Astrophys. J.*, 116(3):1009–1038, Sep 1998.

[17] G. E. Addison, D. J. Watts, C. L. Bennett, M. Halpern, G. Hinshaw, and J. L. Weiland. Elucidating ΛCDM: Impact of Baryon Acoustic Oscillation Measurements on the Hubble Constant Discrepancy. *Astrophys. J.*, 853(2):119, 2018.

[18] A.M. Polyakov. Quark confinement and topology of gauge theories. *Nuclear Physics B*, 120(3):429–458, 1977.

[19] C. Abel, S. Afach, N. J. Ayres, C. A. Baker, G. Ban, G. Bison, K. Bodek, V. Bondar, M. Burghoff, E. Chanel, Z. Chowdhuri, P.-J. Chiu, B. Clement, C. B. Crawford, M. Daum, S. Emmenegger, L. Ferraris-Bouchez, M. Fertl, P. Flaux, B. Franke,

A. Fratangelo, P. Geltenbort, K. Green, W. C. Griffith, M. van der Grinten, Z. D. Grujić, P. G. Harris, L. Hayen, W. Heil, R. Henneck, V. Hélaine, N. Hild, Z. Hodge, M. Horras, P. Iaydjiev, S. N. Ivanov, M. Kasprzak, Y. Kermaidic, K. Kirch, A. Knecht, P. Knowles, H.-C. Koch, P. A. Koss, S. Komposch, A. Kozela, A. Kraft, J. Krempel, M. Kuźniak, B. Lauss, T. Lefort, Y. Lemière, A. Leredde, P. Mohanmurthy, A. Mtchedlishvili, M. Musgrave, O. Naviliat-Cuncic, D. Pais, F. M. Piegsa, E. Pierre, G. Pignol, C. Plonka-Spehr, P. N. Prashanth, G. Quéméner, M. Rawlik, D. Rebreyend, I. Rienäcker, D. Ries, S. Roccia, G. Rogel, D. Rozpedzik, A. Schnabel, P. Schmidt-Wellenburg, N. Severijns, D. Shiers, R. Tavakoli Dinani, J. A. Thorne, R. Virot, J. Voigt, A. Weis, E. Wursten, G. Wyszynski, J. Zejma, J. Zenner, and G. Zsigmond. Measurement of the Permanent Electric Dipole Moment of the Neutron. *Phys. Rev. Lett.*, 124:081803, Feb 2020.

[20] R. D. Peccei and H. R. Quinn. CP Conservation in the Presence of Pseudoparticles. *Phys. Rev. Lett.*, 38:1440–1443, 1977.

[21] Steven Weinberg. A New Light Boson? *Phys. Rev. Lett.*, 40:223–226, 1978.

[22] Frank Wilczek. Problem of Strong P and T Invariance in the Presence of Instantons. *Phys. Rev. Lett.*, 40:279–282, 1978.

[23] Jihn E. Kim. Weak-Interaction Singlet and Strong CP Invariance. *Phys. Rev. Lett.*, 43:103, 1979.

[24] Mikhail A. Shifman, A.I. Vainshtein, and Valentin I. Zakharov. Can confinement ensure natural CP invariance of strong interactions? *Nucl.Phys.*, B166:493, 1980.

[25] Michael Dine, Willy Fischler, and Mark Srednicki. A simple solution to the strong CP problem with a harmless axion. *Phys. Lett.*, B104:199, 1981.

[26] A.R. Zhitnitsky. On Possible Suppression of the Axion Hadron Interactions. (In Russian). *Sov. J. Nucl. Phys.*, 31:260, 1980.

[27] Sz. Borsanyi, Z. Fodor, K. H. Kampert, S. D. Katz, T. Kawanai, T. G. Kovacs, S. W. Mages, A. Pasztor, F. Pittler, J. Redondo, A. Ringwald, and K. K. Szabo. Lattice QCD for Cosmology, 2016.

[28] Kyu Jung Bae, Ji-Haeng Huh, and Jihn E Kim. Updating the axion cold dark matter energy density. *Journal of Cosmology and Astroparticle Physics*, 2008(09):005, Sep 2008.

[29] Guillermo Ballesteros, Javier Redondo, Andreas Ringwald, and Carlos Tamarit. Standard Model—Axion—Seesaw—Higgs Portal Inflation. Five problems of particle physics and cosmology solved in one stroke. *JCAP*, 08:001, 2017.

[30] Sanghyeon Chang and Kiwoon Choi. Hadronic axion window and the big-bang nucleosynthesis. *Physics Letters B*, 316(1):51–56, 1993.

[31] Steen Hannestad, Alessandro Mirizzi, Georg G Raffelt, and Yvonne Y.Y Wong. Neutrino and axion hot dark matter bounds after WMAP-7. *Journal of Cosmology and Astroparticle Physics*, 2010(08):001–001, Aug 2010.

[32] Maria Archidiacono, Steen Hannestad, Alessandro Mirizzi, Georg Raffelt, and Yvonne Y. Y. Wong. Axion hot dark matter bounds after Planck. *JCAP*, 10:020, 2013.

[33] Eleonora Di Valentino, Elena Giusarma, Massimiliano Lattanzi, Olga Mena, Alessandro Melchiorri, and Joseph Silk. Cosmological axion and neutrino mass constraints from Planck 2015 temperature and polarization data. *Physics Letters B*, 752:182–185, 2016.

[34] S. Chang, C. Hagmann, and P. Sikivie. Studies of the motion and decay of axion walls bounded by strings. *Physical Review D*, 59(2), Dec 1998.

[35] C. Hagmann, S. Chang, and P. Sikivie. Axion radiation from strings. *Physical Review D*, 63(12), May 2001.

[36] Takashi Hiramatsu, Masahiro Kawasaki, Toyokazu Sekiguchi, Masahide Yamaguchi, and Jun'ichi Yokoyama. Improved estimation of radiated axions from cosmological axionic strings. *Physical Review D*, 83(12), Jun. 2011.

[37] Masahiro Kawasaki, Ken'ichi Saikawa, and Toyokazu Sekiguchi. Axion dark matter from topological defects. *Physical Review D*, 91(6), Mar 2015.

[38] Takashi Hiramatsu, Masahiro Kawasaki, Ken'ichi Saikawa, and Toyokazu Sekiguchi. Production of dark matter axions from collapse of string-wall systems. *Phys. Rev. D*, 85:105020, May 2012.

[39] P.A. Zyla et al. Review of Particle Physics. *PTEP*, 2020(8):083C01, 2020.

[40] Paolo Gondolo and Georg G. Raffelt. Solar neutrino limit on axions and keV-mass bosons. *Phys. Rev. D*, 79:107301, May 2009.

[41] N. Viaux, M. Catelan, P. B. Stetson, G. G. Raffelt, J. Redondo, A. A. R. Valcarce, and A. Weiss. Neutrino and Axion Bounds from the Globular Cluster M5 (NGC 5904). *Phys. Rev. Lett.*, 111:231301, Dec 2013.

[42] Adam Burrows, M. Ted Ressell, and Michael S. Turner. Axions and SN 1987A: Axion trapping. *Phys. Rev. D*, 42:3297–3309, Nov 1990.

[43] Michael S. Turner. Axions from SN1987A. *Phys. Rev. Lett.*, 60:1797–1800, May 1988.

[44] Peter S. Shternin, Dmitry G. Yakovlev, Craig O. Heinke, Wynn C. G. Ho, and Daniel J. Patnaude. Cooling neutron star in the Cassiopeia A supernova remnant: evidence for superfluidity in the core. *Monthly Notices of the Royal Astronomical Society: Letters*, 412(1):L108–L112, 03 2011.

[45] Dany Page, Madappa Prakash, James M. Lattimer, and Andrew W. Steiner. Rapid Cooling of the Neutron Star in Cassiopeia A Triggered by Neutron Superfluidity in Dense Matter. *Phys. Rev. Lett.*, 106:081101, Feb 2011.

[46] Mikhail V. Beznogov, Ermal Rrapaj, Dany Page, and Sanjay Reddy. Constraints on axion-like particles and nucleon pairing in dense matter from the hot neutron star in HESS J1731-347. *Phys. Rev. C*, 98:035802, Sep 2018.

[47] Asimina Arvanitaki, Masha Baryakhtar, and Xinlu Huang. Discovering the QCD axion with black holes and gravitational waves. *Phys. Rev. D*, 91:084011, Apr 2015.

[48] R. Ballou, G. Deferne, M. Finger, M. Finger, L. Flekova, J. Hosek, S. Kunc, K. Macuchova, K. A. Meissner, P. Pugnat, M. Schott, A. Siemko, M. Slunecka, M. Sulc, C. Weinsheimer, and J. Zicha. New exclusion limits on scalar and pseudoscalar axionlike particles from light shining through a wall. *Phys. Rev. D*, 92:092002, Nov 2015.

[49] V. Anastassopoulos, S. Aune, K. Barth, A. Belov, H. Bräuninger, G. Cantatore, J. M. Carmona, J. F. Castel, S. A. Cetin, F. Christensen, J. I. Collar, T. Dafni, M. Davenport, T. A. Decker, A. Dermenev, K. Desch, C. Eleftheriadis, G. Fanourakis, E. Ferrer-Ribas, H. Fischer, J. A. García, A. Gardikiotis, J. G. Garza, E. N. Gazis, T. Geralis, I. Giomataris, S. Gninenko, C. J. Hailey, M. D. Hasinoff, D. H. H. Hoffmann, F. J. Iguaz, I. G. Irastorza, A. Jakobsen, J. Jacoby, K. Jakovčić, J. Kaminski, M. Karuza, N. Kralj, M. Krčmar, S. Kostoglou, Ch. Krieger, B. Lakić, J. M. Laurent, A. Liolios, A. Ljubičić, G. Luzón, M. Maroudas, L. Miceli, S. Neff, I. Ortega, T. Papaevangelou, K. Paraschou, M. J. Pivovaroff, G. Raffelt, M. Rosu, J. Ruz, E. Ruiz Chóliz, I. Savvidis, S. Schmidt, Y. K. Semertzidis, S. K. Solanki, L. Stewart, T. Vafeiadis, J. K. Vogel, S. C. Yildiz, K. Zioutas, and C. A. S. T. Collaboration. New CAST limit on the axion–photon interaction. *Nature Physics*, 13(6):584–590, Jun 2017.

[50] J. K. Vogel et al. The Next Generation of Axion Helioscopes: The International Axion Observatory (IAXO). *Phys. Procedia*, 61:193–200, 2015.

[51] P. Sikivie. Experimental "Tests" of the Invisible Axion. *Phys. Rev. Lett.*, 51:1415–1417, 1983.

[52] R. H. Dicke. The Measurement of Thermal Radiation at Microwave Frequencies. *Rev. Sci. Inst.*, 17(7):268–275, 1946.

[53] Michael S. Turner. Periodic signatures for the detection of cosmic axions. *Phys. Rev. D*, 42:3572–3575, Nov 1990.

[54] Erik W. Lentz, Thomas R. Quinn, Leslie J Rosenberg, and Michael J. Tremmel. A New Signal Model for Axion Cavity Searches from N-body Simulations. *The Astrophysical Journal*, 845(2):121, aug 2017.

[55] L. D. Duffy and P. Sikivie. Caustic ring model of the Milky Way halo. *Physical Review D*, 78(6), Sep 2008.

[56] S. J. Asztalos, G. Carosi, C. Hagmann, D. Kinion, K. van Bibber, M. Hotz, L. J Rosenberg, G. Rybka, J. Hoskins, J. Hwang, P. Sikivie, D. B. Tanner, R. Bradley, and J. Clarke. SQUID-Based Microwave Cavity Search for Dark-Matter Axions. *Phys. Rev. Lett.*, 104:041301, Jan 2010.

[57] N. Du, N. Force, R. Khatiwada, E. Lentz, R. Ottens, L. J Rosenberg, G. Rybka, G. Carosi, N. Woollett, D. Bowring, A. S. Chou, A. Sonnenschein, W. Wester, C. Boutan, N. S. Oblath, R. Bradley, E. J. Daw, A. V. Dixit, J. Clarke, S. R. O'Kelley, N. Crisosto, J. R. Gleason, S. Jois, P. Sikivie, I. Stern, N. S. Sullivan, D B Tanner, and G. C. Hilton. Search for Invisible Axion Dark Matter with the Axion Dark Matter Experiment. *Phys. Rev. Lett.*, 120:151301, Apr 2018.

[58] T. Braine, R. Cervantes, N. Crisosto, N. Du, S. Kimes, L. J. Rosenberg, G. Rybka, J. Yang, D. Bowring, A. S. Chou, R. Khatiwada, A. Sonnenschein, W. Wester, G. Carosi, N. Woollett, L. D. Duffy, R. Bradley, C. Boutan, M. Jones, B. H. LaRoque, N. S. Oblath, M. S. Taubman, J. Clarke, A. Dove, A. Eddins, S. R. O'Kelley, S. Nawaz, I. Siddiqi, N. Stevenson, A. Agrawal, A. V. Dixit, J. R. Gleason, S. Jois, P. Sikivie, J. A. Solomon, N. S. Sullivan, D. B. Tanner, E. Lentz, E. J. Daw, J. H. Buckley, P. M. Harrington, E. A. Henriksen, and K. W. Murch. Extended Search for the Invisible Axion with the Axion Dark Matter Experiment. *Phys. Rev. Lett.*, 124:101303, Mar 2020.

[59] Dongok Kim, Junu Jeong, SungWoo Youn, Younggeun Kim, and Yannis K. Semertzidis. Revisiting the detection rate for axion haloscopes. *Journal of Cosmology and Astroparticle Physics*, 2020(03):066–066, Mar 2020.

[60] John David Jackson. Classical Electrodynamics 2nd ed., 1975.

[61] MμShield Magnetic Shielding. Mμshield magnetic shielding hydroforming, mumetal itar & iso certified manufacturing, 2021. https://www.mushield.com/.

[62] S.J. Asztalos, G. Carosi, C. Hagmann, D. Kinion, K. van Bibber, M. Hotz, L. J Rosenberg, G. Rybka, A. Wagner, J. Hoskins, C. Martin, N. S. Sullivan, D. B. Tanner, R. Bradley, and John Clarke. Design and performance of the ADMX SQUID-based microwave receiver. *Nucl. Instrum. Methods Phys. Res. A*, 656(1):39 – 44, 2011.

[63] Low Noise Factory. State-of-the-art room temperature and cryogenic low noise amplifiers, 2021. https://www.lownoisefactory.com/.

[64] Quinnstar Technology. Millimeter-wave innovation, 2021. https://quinstar.com/.

[65] I. Siddiqi, R. Vijay, F. Pierre, C. M. Wilson, M. Metcalfe, C. Rigetti, L. Frunzio, and M. H. Devoret. RF-Driven Josephson Bifurcation Amplifier for Quantum Measurement. *Physical Review Letters*, 93(20), Nov 2004.

[66] M. H Devoret, A Wallraff, and J. M Martinis. Superconducting Qubits: A Short Review. 2004.

[67] Keysight Technologies. Keysight: Electronic design, test automation & measurement equipment, 2021. https://www.keysight.com/.

[68] AlazarTech. Alazartech PCI digitizers, 2021. https://www.alazartech.com/.

[69] C.J. Yeager and S.S. Courts. A review of cryogenic thermometry and common temperature sensors. *IEEE Sensors Journal*, 1(4):352–360, 2001.

[70] Lakeshore Cryotronics. Lakeshore cryotronics-advancing science, 2021. https://www.lakeshore.com/.

[71] Agilent Scientific Instruments. Agilent: Chemical analysis, life sciences, and diagnostics, 2021. https://www.agilent.com/.

[72] A.J. Kozubal, D.M. Kerstiens, J.O. Hill, and L.R. Dalesio. Run-time environment and application tools for the ground test accelerator control system. *Nuclear Instruments and Methods in Physics Research Section A: Accelerators, Spectrometers, Detectors and Associated Equipment*, 293(1):288 – 291, 1990.

[73] John C. (John Clayton) Worsley. Practical Postgresql, 2002.

[74] C. Boutan, M. Jones, B. H. LaRoque, N. S. Oblath, R. Cervantes, N. Du, N. Force, S. Kimes, R. Ottens, L. J. Rosenberg, G. Rybka, J. Yang, G. Carosi, N. Woollett, D. Bowring, A. S. Chou, R. Khatiwada, A. Sonnenschein, W. Wester, R. Bradley, E. J. Daw, A. Agrawal, A. V. Dixit, J. Clarke, S. R. O'Kelley, N. Crisosto, J. R. Gleason,

S. Jois, P. Sikivie, I. Stern, N. S. Sullivan, D. B. Tanner, P. M. Harrington, and E. Lentz. Piezoelectrically Tuned Multimode Cavity Search for Axion Dark Matter. *Phys. Rev. Lett.*, 121:261302, Dec 2018.

[75] Gianpalo Carosi, Raphael Cervantes, Seth Kimes, Parashar Mohapatra, Rich Ottens, and Gray Rybka. Orpheus: Extending the ADMX QCD Dark-Matter Axion Search to Higher Masses. In Gianpaolo Carosi and Gray Rybka, editors, *Microwave Cavities and Detectors for Axion Research*, pages 169–175, Cham, 2020. Springer International Publishing.

[76] Xiaoyue Li. MADMAX: A Dielectric Haloscope Experiment. *J. Phys. Conf. Ser.*, 1468(1):012062, 2020.

[77] Kurt Jung. *Beginning Lua programming.* Wrox beginning guides. Wiley/Wrox, Indianapolis, IN, 2007.

[78] T. L. Wilson. Techniques of Radio Astronomy, 2011.

[79] Edward John Daw. *A Search for Halo Axions.* PhD thesis, Massachusetts Institute of Technology, 1998.

[80] Abraham. Savitzky and M. J. E. Golay. Smoothing and Differentiation of Data by Simplified Least Squares Procedures. *Analytical Chemistry*, 36(8):1627–1639, 1964.

[81] George A. (George Allen) Baker. Padé approximants, 1996.

[82] CST studio suite. https://www.3ds.com/products-services/simulia/products/cst-studio-suite/. Accessed: 2019-12-06.

[83] Joachim Hartung. Statistical Meta-Analysis with Applications, 2008.

[84] S. Asztalos, E. Daw, H. Peng, L. J Rosenberg, C. Hagmann, D. Kinion, W. Stoeffl, K. van Bibber, P. Sikivie, N. S. Sullivan, D. B. Tanner, F. Nezrick, M. S. Turner, D. M. Moltz, J. Powell, M.-O. André, J. Clarke, M. Mück, and Richard F. Bradley. Large-scale microwave cavity search for dark-matter axions. *Phys. Rev. D*, 64:092003, Oct 2001.

[85] L.F. Abbott and P. Sikivie. A cosmological bound on the invisible axion. *Phys. Lett.*, B120:133–136, 1983.

[86] Michael Dine and Willy Fischler. The not-so-harmless axion. *Phys. Lett. B*, 120(1):137 – 141, 1983.

[87] John Preskill, Mark B. Wise, and Frank Wilczek. Cosmology of the invisible axion. *Phys. Lett.*, B120:127–132, 1983.

[88] J. Ipser and P. Sikivie. Can Galactic Halos Be Made of Axions? *Phys. Rev. Lett.*, 50:925–927, Mar 1983.

[89] Claudio Bonati, Massimo D'Elia, Marco Mariti, Guido Martinelli, Michele Mesiti, Francesco Negro, Francesco Sanfilippo, and Giovanni Villadoro. Axion phenomenology and θ-dependence from $N_f = 2 + 1$ lattice QCD. *Journal of High Energy Physics*, 2016(3):155, 2016.

[90] Evan Berkowitz, Michael I. Buchoff, and Enrico Rinaldi. Lattice QCD input for axion cosmology. *Phys. Rev. D*, 92:034507, Aug 2015.

[91] S Borsanyi, Z Fodor, J Guenther, K.-H. Kampert, S D Katz, T Kawanai, T G Kovacs, S W Mages, A Pasztor, F Pittler, J Redondo, A Ringwald, and K K Szabo. Calculation of the axion mass based on high-temperature lattice quantum chromodynamics. *Nature*, 539(7627):69–71, Nov 2016.

[92] Guillermo Ballesteros, Javier Redondo, Andreas Ringwald, and Carlos Tamarit. Unifying Inflation with the Axion, Dark Matter, Baryogenesis, and the Seesaw Mechanism. *Phys. Rev. Lett.*, 118:071802, Feb 2017.

[93] Michael Dine, Patrick Draper, Laurel Stephenson-Haskins, and Di Xu. Axions, instantons, and the lattice. *Phys. Rev. D*, 96:095001, Nov 2017.

[94] Peter Petreczky, Hans-Peter Schadler, and Sayantan Sharma. The topological susceptibility in finite temperature QCD and axion cosmology. *Physics Letters B*, 762:498 – 505, 2016.

Appendix A

SYSTEM NOISE TEMPERATURE CALIBRATION FROM RECEIVER MEASUREMENTS

An improved understanding of the cryogenic RF background could also provide an additional means of calibrating the system noise temperature of the experiment. Recall the receiver diagram shown in figure 3.7. The power off-resonance from the cavity is dominated by the noise emitted from attenuator A at 100 mK, and reflected off the cavity and the power on-resonance is dominated by noise emitted from the cavity at 130 mK. In principle, because the power is measured both on- and off-resonance and the temperatures of the noise sources are known, the system noise temperature can be calibrated, similar in concept to the Y-factor measurements discussed in section 4.7. However, this requires a well-understood model of the RF background noise of the receiver.

For run 1B, the model developed for the RF background assumed that the Johnson noise from attenuator A and the cavity were amplified by the JPA and HFET. The noise from the cavity followed a Lorentzian lineshape centered on the resonant frequency of the cavity. The noise from attenuator A was reflected off the cavity. In addition, a small component of noise from attenuator A was transmitted through the circulator against the directionality of the circulator. This process was described by a RF background of the form,

$$P_{output} = (a_1 + a_2 \times \frac{1}{1+x^2} + a_3 \times \frac{x}{1+x^2}) * (1 + a_4 \times x);\ x = \frac{2Q(f-f_0)}{f_0} \tag{A.1}$$

where a_1, a_2, a_3, and a_4 were free parameters of the fit.

Terms in the first set of parenthesis arose from modeling the system as previously described with off-resonance noise from attenuator A and on-resonance noise from the cavity. The term in the second set of parenthesis arises from approximations of the frequency-dependent response of the JPA gain. The gain response of the JPA resembles a Lorentzian where the gain is maximized at the JPA pump-tone frequency. Because the pump-tone frequency is fixed at 375 kHz above the cavity frequency, an increase in the gain across the range of each individual spectra is expected, and this gain is approximated as linear. Note this fit is similar in form to a 4-parameter Padé fit.

The fit parameters can be expressed in terms of physical parameters within the experiment as

$$a_1 = G_{rec}(T_A \times (1 + \epsilon_{circ} + 2\sqrt{\epsilon_{circ}}cos(\Delta)) + T_{rec}) \tag{A.2}$$

$$a_2 = G_{rec}(T_{cav} - T_A \times (1 + 2\sqrt{\epsilon_{circ}}cos(\Delta)) \tag{A.3}$$

$$a_3 = G_{rec}(T_A\sqrt{\epsilon_{circ}}sin(\Delta) \tag{A.4}$$

where G_{rec} is the power gain of the receiver, T_{rec} is the noise temperature contribution of the receiver, T_A is the temperature of attenuator A, T_{cav} is the temperature of the cavity, ϵ_{circ} is the isolation loss of the circulators, and Δ is a phase offset between the signal incident on and reflected by the cavity.

Figure A.1 shows the fit parameters, a_1, a_2, and a_3, as a function of frequency. While in principle it would be possible to extract physical parameters from the fit, such as the system noise temperature, we didn't do so for run 1B as unphysical values arose from the model. For example, in our model, a_2 could be approximated as the difference between the temperature of the cavity and the attenuator A. Since the cavity was consistently hotter than attenuator A, a_2 is should always be positive, even when accounting for small perturbations from the term, $2\sqrt{\alpha_{circ}}cos(\Delta)$. However, figure A.1 shows instances where the fit parameter a_2 is negative. Such instances suggest that this RF model is yet incomplete.

However, we observed some of the predicted variations in the fit parameters. For example, a sinusoidal-like variation is observed in the fit parameters as a function of the cavity's resonant frequency. Such behavior is expected as the electrical length, and as a result the phase offset between the signal from the attenuator being reflected by the cavity and the signal from the attenuator traveling backward through the circulator, will increase with increasing frequency. For the purposes of the analysis, we concluded that the model developed for run 1B was an approximation used only to help establish the origins of the RF background in the receiver. In the future, a more comprehensive model generated using RF simulation software could provide an improved understanding of the RF background. Hence, during run 1B, the system noise was calibrated using the methods discussed in section 4.7, which were independent of the RF model.

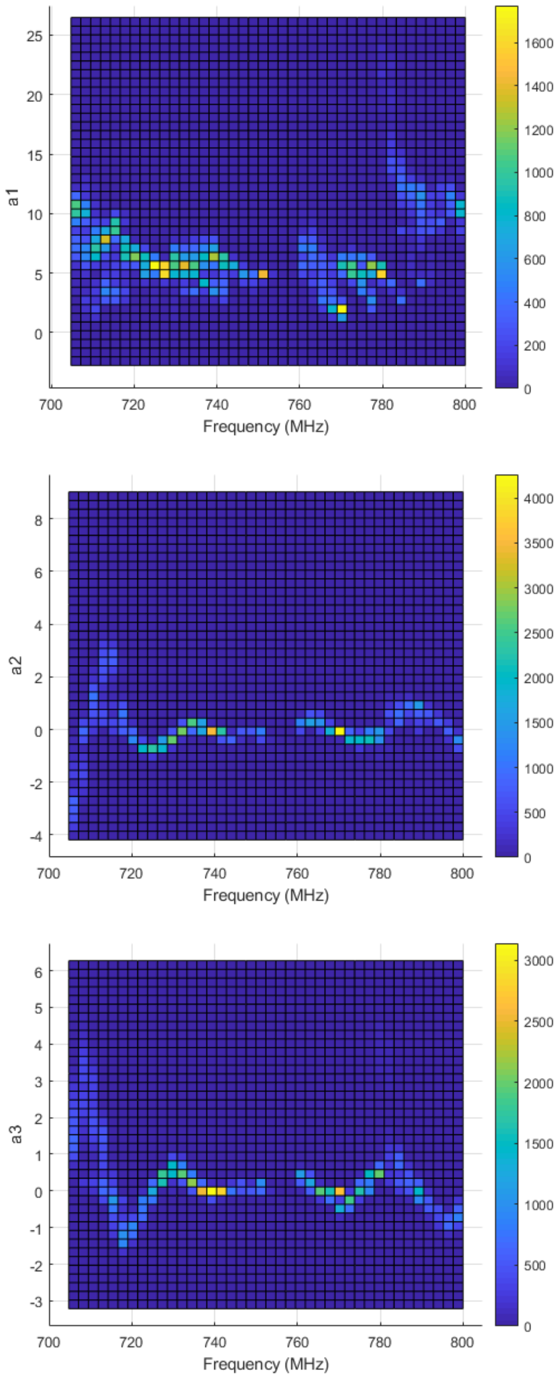

Figure A.1: Histograms of the fit parameters as a function of the resonant frequency of the cavity. The gap around 758 MHz is due to a mode crossing preventing data from being collected at that frequency.

Funding Acknowledgements

This work was supported by the U.S. Department of Energy through Grants No DE-SC0009800, No. DE-SC0009723, No. DE-SC0010296, No. DE-SC0010280, No. DE-SC0011665, No. DEFG02-97ER41029, No. DE-FG02-96ER40956, No. DEAC52-07NA27344, No. DE-C03-76SF00098 and No. DE-SC0017987. Fermilab is a U.S. Department of Energy, Office of Science, HEP User Facility. Fermilab is managed by Fermi Research Alliance, LLC (FRA), acting under Contract No. DE-AC02-07CH11359. Additional support was provided by the Heising-Simons Foundation and by the Lawrence Livermore National Laboratory and Pacific Northwest National Laboratory LDRD offices.